The Machining of Titanium Alloys with Polycrystalline Diamond Tools

By

Wencheng Pan

B. Eng. Automotive

A thesis submitted in fulfillment of the requirements for the degree of Doctor of Philosophy

March 2014

School of Aerospace, Mechanical and Manufacturing Engineering

RMIT University

Melbourne, Australia

Abstract

The excellent mechanical properties and unrivalled corrosion resistance of Titanium have led to the successful application of Titanium alloys in aerospace industry. However, the inherent properties of low thermal conductivity and high chemical reactivity of Titanium alloys cause poor machinability. They adversely affect tool life, cause premature tool failure, and eventually lead to extremely low machining efficiency.

Recently, Polycrystalline diamond (PCD) tools have been successfully used in the turning of Titanium alloys. The significant hardness and the excellent thermal conductivity of PCD make it the most advantageous tool material for the machining of Titanium alloys, in particular Ti6Al4V. This research investigated the application of PCD tools in the end milling of Ti6Al4V by using customized cutting tools. The discharge characteristics of PCD was analyzed; the mathematical relationship between cutting force and cutting parameters was developed; tool life, tool wear, and causes that lead to tool failure were discussed. A cutting temperature model was developed and validated to investigate the relationship between cutting temperature and machining parameters. To analyze tool wear and cutting temperatures, residual chemical components on the PCD tool were examined with X-ray diffraction method, while surface integrity of cutting tools was inspected based on the images taken by the scanning electrical microscope. Finite element analysis models were developed to simulate the initiation of cracks under different loading cycles.

The main contributions of the research are as follows:

1. The development of new instantaneous cutting force models. The predictive models are able to predict both the peak value of cutting force and the instantaneous cutting force.

2. The development of a new cutting temperature model which is able to describe the mathematical relationship between machining parameters (*cutting speed*: v_c, *feed*: f_d and *axial cutting depth*: a_p) and the dynamic cutting temperature.

3. New findings in tool wear mechanism and chip morphology in end milling Ti6Al4V with PCD tools. Three failure types of PCD tool have been identified. The mechanisms of these failure types are shearing effect on the boundary of tool-chip interface, stress concentration at notch locations on the cutting edge and the uneven distribution of cutting stress on the contact area between tool and chip. The feed was confirmed to be the most important factor affecting the final surface quality. Two different serration

frequencies were found on a single chip. The boundary between two areas with different serration frequencies was found to be at a position of 25 % of the chip length.

Declaration

I certify that except where due acknowledgement has been made, the work is that of the author alone; the work has not been submitted previously, in whole or in part, to qualify for any other academic award; the content of the thesis is the result of work which has been carried out since the official commencement date of the approved research program; any editorial work, paid or unpaid, carried out by a third party is acknowledged; and, ethics procedures and guidelines have been followed.

Wencheng Pan

March 2014

Acknowledgements

I sincerely show my gratitude for the grateful support of my supervisors Dr. Songlin Ding and Prof. John Mo. Their expertise, input and advice have been ordinarily valuable for my whole research program. And I also thank Dr. Andrew Mackie and Mr. Prat Karan for their support in proofreading my thesis.

My particularly thanks go to my parents and wife Yingxi Chen.

Publications

The following publications are associated with this research:

1. **Wencheng Pan**, Adam Kamaruddin, Songlin Ding, John Mo "Experimental investigation of end milling of Titanium alloys with polycrystalline diamond (PCD) tools", *Proceedings of the Institution of Mechanical Engineers, Part B, Journal of Engineering Manufacture*, 2014, Accepted.

2. **Wencheng Pan**, Bramha Kondaiah, Songlin Ding, John Mo "Tool wear and surface integrity in end milling of Ti6Al4V with Polycrystalline Diamond tools", *Advanced Materials Research*, Vol. 820 (2013) pp 134-137.

3. **Wencheng Pan**, Songlin Ding, John Mo, "Statistical analysis of cutting forces in the milling of Titanium alloys with Polycrystalline Diamond (PCD) tools", *Applied Mechanics and Materials*, 2013, Vols. 271-272, p.338-342.

4. A. Kamaruddin, **W.C. Pan**, S.L. Ding, J. Mo, " Preliminary study on the effect of mass-induced damping on machining delicate workpiece geometry", *Advanced Material Research*, 2013, Vol.764, p 83-89.

5 S. Ye, **W. Pan**, S. Ding, J, Mo, M. Brandt, A. Mackie "Electrical Discharge Characteristics of Polycrystalline Diamonds", *Advanced Materials Research*, 2012 Vol. 426, p 44-47.nduced damping on machining delicate workpiece geometry", *Advanced Material Research*, 2013, Vol.764, p 83-89.

6 **Wencheng P**, Songlin D, John M. "Thermal characteristics in milling Ti6Al4V with polycrystalline diamond tools" *International Journal of Advanced Manufacturing Technology, 2014, accepted.*

7 **Wencheng P**, Songlin D, John M. "The prediction of cutting force in end milling Titanium alloy (Ti6Al4V) with PCD tools" – Submitted to *Proceedings of the Institution of Mechanical Engineers, Part B, Journal of Engineering Manufacture*.

TABLE OF CONTENTS

LIST OF FIGURES

LIST OF TABLES

NOMENCLATURE

Term	Description
A	The parameter of Johnson-Cook constitutive equation
a_p	Axial cutting depth
B	The parameter of Johnson-Cook constitutive equation
BCBN	Binderless Cubich Boron Nitride
C	The parameter of Johnson-Cook constitutive equation
CBN	Cubic Boron Nitride
CVD	Chemical Vapor Deposition diamond
c	Thermal conductivity of workpiece
db	length of differential cutting edge perpendicular to cutting speed
ECEA	End Cutting Edge Angle
EDG	Electrical Discharge Grinding
EDM	Electrical Discharge Machining
erf	$erf(x) = \frac{2}{\sqrt{\pi}} \int_0^x e^{-t^2} dt$
F	Resultant force
F_{dy}	The instantaneous cutting force
FEM	Finite Element Method
F_{max}	The peak values of the tangential, radial and axial force components in each milling cycle
F_T, F_R, F_Z	The tangential, radial and axial force components of local coordinate system
F_X, F_Y	The force components in Cartesian coordinate system of workpiece
f	Feed
HSS	High Speed Steel
$h(\varphi)$	Instantaneous uncut chip thickness at the rotation angle φ
K_i	The constants of cutting temperature
K_T,K_R,K_Z	Shearing specific coefficients
K_{tc},K_{rc},K_{ac}	Edge specific coefficients
k_t, k_r, $k_{z,}$	The cutting force constants of the tangential, radial and axial force components
$l_{R,}$ l_Z	The cutting force constants of the radial and axial force components
m	Runout parameters
m_1,m_2,m_3	Three empirical parameters to calculate cutting force components
m_T, m_R, m_Z	The cutting force constants of the tangential, radial and axial force

	components
n	The parameter of Johnson-Cook constitutive equation

Term	Description
i_p	Peak current
PCBN	Polycrystalline Cubic Boron Nitride
PCD	Polycrystalline Diamond
Q	Heat generation of machining process
q_i	The heat source of shear plane and flank
q_M	Heat flux
R_1,R_2,	The coefficients of cutting temperature model
R_c	The value of workpiece resistance
$R(\varphi)$	the radius of each circumference
R_0	Tool radius
S	The length of cutting edge
T	Temperature of material
T_{AVE}	Average cutting temperature on tool
T_r	Room temperature
T_m	Melting temperature
T_t	Tool wear value as illustrated at *Figure 6.6*
t	Milling time
U_e	The discharging voltage of gap
U_g	The discharging voltage which crosses the channel
U_r	The discharging voltage which crosses the workpiece
x_i,y_i,z_i	The dimension of measuring point in the coordinate system of shear plane Heat source or flank heat source
WBN	Wurtzite phase of Boron Nitride
WC	Tungsten carbide
v	Cutting speed
z	The normal distance of measuring point from tool-chip interface
α	Diffusivity of workpiece
φ	Rotation angle
τ	Time
κ	positioning angle
ρ	Density
θ_i	The cutting temperature which is determined by shear plane heat source or flank heat source

1 Introduction

1.1 Introduction

Owing to the high strength-to-weight ratio and high resistance to corrosion, Titanium and its alloys, in particular Ti6Al4V, are used widely in aerospace industry. Many conventional tool materials such as tungsten carbide (WC) and High Speed Steel (HSS) have been used in the end milling process since Ti6Al4V was invented. However, short tool life is one of the most significant issues associated with the problem of improving machinability of Ti6Al4V. Ti6Al4V has very high mechanical yield strength, fracture energy and chemical affinity. It also has extremely low thermal conductivity which contributes to the dramatic shortening of tool life in some high speed machining processes. In order to improve the machinability of Ti6Al4V, Polycrystalline diamond (PCD) has been applied in aerospace industry as a new cutting tool material [1]. The Low G ratios, high cutting force, and high wheel cost pose a significant challenge to the machinability of Ti6Al4V. Moreover, the PCD mills with small size were used in few experiments, this limit the application of Ti6Al4V in the industries. Therefore, to investigate the small size PCD mill is also one of the objective to this project.

The Electrical-discharge Grinding (EDG) is a non-contact thermal erosion process in which the metal is removed by a series of recurring electrical discharges between the rotating electrode and the electrically conductive workpiece, in the presence of a dielectric fluid. The electric conductivity of PCD caused by the conductive binding material (Cobalt) makes it possible to grind PCD tools with EDG technology. However, since PCD is a relatively low bulk conductivity material, the discharge characteristics of PCD are different from conventional tool material such as Carbide or Carbone Tungsten. In practice there is a pressing need to find its special discharge characteristics to facilitate the design of proper EDG processes. The investigation of PCD electrical discharge characteristics include: study of dynamic voltage and current waveforms, study of PCD dynamic electric resistance and study of short circuit exception. The optimization of the grinding process can be done by monitoring parameters such as the ignition time of pulses and using them for the manipulation of open circuit voltage, current limit and pulse on and off times.

Cutting force is a critical factor that affects tool life and surface integrity of the workpieces. The availability of an accurate cutting force model is very important in predicting cutting forces, which in turn are used in selecting suitable machining parameters. Normally, the calculations of instantaneous chip thickness and cutting coefficients of cutting force components are the two main methods for determining the value of cutting force. The theoretical chip thickness is affected by run out effect, tool geometry and cooling conditions. However, with different tool

materials and workpieces, the cutting force curves of machining Ti6Al4V always show fluctuations which so far have been investigated in very few the literatures. More accurate expressions of cutting forces are needed when new tool materials like PCD are applied in the machining process.

High strength, low density and good corrosion resistance make Titanium alloy Ti6Al4V a popular material in aerospace, biomechanical, marine and chemical industries. However, due to its low thermal conductivity, Ti6Al4V is difficult to machine. To improve the machinability, many researches have been conducted in the past decades to study the thermal effects in milling Ti6Al4V with focusing on the analysis of cutting temperature and chemical components. Rosemar et al. [1] found segmented chips in the experiment with high pressure cooling and continuous chip in the test with a conventional cooling system. Mohd Hadzley et al. [2] successfully developed a Finite Element Method (FEM) model for the process of machining Ti6Al4V under the high pressure cooling which correctly simulated the cutting temperature and chip formation. The high cutting temperature is mainly caused by the heat generated during the machining process. The endmilling process is relatively unstable, because the tool and workpiece contact intermittently. The cutting heat generation rate and dissipation rate vary a great deal. According to Lin et al. [3], there are two components to the heat generation process in the milling system: the heat is generated from the shearing effect and from the friction of tool and chip. Changes in machining parameters can result in more, or less, heat generation which causes a cutting temperature change. Ti6Al4V has high chemical affinity with most tool materials when the working temperature rises above 500^{o}C. The main chemical components of PCD tools are diamond, cobalt and WC, the last of which is generally used for the PCD backing. Graphitization of the diamond is likely to begin to occur when the cutting temperature is in the region of to 800^{o}C. The modelling of cutting temperature is therefore important to the application of using PCD tools for endmilling Ti6Al4V.

Tool wear analysis is one of the most important aspects associated with developing new tools for the metalworking. Poor surface quality usually results from by excessive tool wear and always after catastrophic tool failure. Different tool wear forms will result in different surface quality. Generally, tool wear form and evolution are two major research areas. In term of endmilling Ti6Al4V process, the conventional tool wear forms appear as chipping, built-up-edge, chemical reaction and material diffusion, although previous research has demonstrated that in the case of synthetic diamond tools (PCD and CVD), the high yield strength and thermal conductivity of the diamond results in significant tool performance improvements in turning Ti6Al4V [4]. Many studies [1, 4] of the machining Ti6Al4V process have not done the chemical examination in

detail due to various reasons; there is an opportunity to identify tool wear form and mechanism by investigating residual chemical components on the PCD tools.

The analysis of surface quality resultant from different machining conditions allows for optimizing the machining processes. It is known vibration or chatter exists when machining Titanium under a wide range of machining parameters [5]. Erratic vibration and unpredictable chatter always causes bad surface quality. To some extent, the adiabatic shearing frequency which is also known as serration frequency indicates the stability of the instantaneous cutting force. The study of chip morphology will provide important information which is essential for understanding the process of end milling Ti6Al4V with PCD tools.

1.2 Research objectives

The research overall objectives is to develop PCD endmilling tool in the application of machining Ti6Al4V. And the research objectives are outlined below.

1. *To investigate electrical discharge characteristics of PCD*

Due to commercial confidentiality requirements, little analysis of PCD discharge waveforms has been published in the public domain. The resistance of PCD is a critical value for determining the input voltage and current in the EDG process. Determination of this value requires design and analysis of an idealized circuit. To investigate the electrical discharge characteristics of PCD material, several aspects require analysis: the influence of current on discharge waveform, the relationship between gap voltages, peak current and electrical resistance of various PCD materials.

The detailed process is listed as follows:

- Record and analyze discharge waveforms in the test of three materials (*CMX850*, *CTM302* and *WC*) and to identify the influence of changing current and voltage in the process.
- Investigate the relationship between gap voltage, peak current and electrical resistance of various PCD materials.

2. *To develop instantaneous cutting force models*

Currently most instantaneous cutting force models were developed by considering the instantaneous chip thickness as the only variable which changes over time. However, there are many fluctuations caused by the adiabatic shearing effect or cooling conditions which exist and

affect the instantaneous cutting force. Moreover, the changes in machining parameter will directly lead to changes in material shearing speed, friction speed and tool - chip contact area.

The analysis of instantaneous cutting force with different machining parameters allows new opportunities for developing a novel cutting force model which fully incorporates the influence of machining parameters. The model will reveal the time dependency of the cutting force.

The detailed tasks include:

- To develop and validate the new cutting force model to describe the mathematical relationship between instantaneous cutting force peak values and machining parameters.
- To deduce a new time-dependent function for instantaneous cutting force.

3. *To analyze thermal characteristics in the end milling of Ti6Al4V*

In the process of end milling Ti6Al4V with PCD tools, the study of the relationship between dynamic cutting temperature and machining parameters was incomplete in the literature. In addition, the chemical reactions taking place during machining have not been investigated in detail by any researcher. The chemical analysis of used PCD tools will yield useful results which are critical for understanding the process of endmilling Ti6Al4V with PCD tools.

The detailed tasks are as follows:

- To develop and validate the new dynamic cutting temperature model to describe the mathematical relationship between the controllable machine parameters and dynamic cutting temperature.
- To complete the chemical analysis of PCD tools which have been used under different machining conditions.

4. *To investigate wear mechanism of PCD tools in end milling Ti6Al4V*

Tool wear analysis of PCD has been done by many researchers for the machining of different materials. However, tool wear and evolution in end milling Ti6Al4V with PCD tools have not been investigated in the literature and there are a lot of unknowns about the tool failure mechanism in end milling Ti6Al4V.

5. *To investigate surface quality and chip morphology*

A constant adiabatic shearing frequency indicates a relatively stable machining process. However, due to the high thermal conductivity of PCD material, the chip morphology is expected to be different from the process using other tool materials. The surface quality resulting from endmilling Ti6Al4V with different tool materials has not been analyzed by any researcher with consideration of the influence of machining parameters,

In summary, this research focuses on improving the machinability of Ti6Al4V with the application of PCD end milling tools. The main objectives are to study the electric discharge characteristics of PCD materials, to develop a instantaneous cutting force model, to develop a dynamic cutting temperature model, to investigate the tool wear mechanism and surface quality. The project outcome is knowledge necessary for the successful application of PCD tool material in the process of endmilling Ti6Al4V.

This thesis will answer the follow research questions:

1. How do the electric discharging characteristics of PCD behave in the Electrical Discharge Machining (EDM) process?

2. How can the cutting force model describe the mathematical relationship between instantaneous cutting force and machining parameters?

3. How can the cutting temperature model describe the mathematical relationship between dynamic cutting temperature and machining parameters?

4. What are the possible chemical reactions occurring in the region of the cutting zone which is at an evaluated temperature?

5. What is the main tool wear form of PCD? How does PCD tool wear evolve?

6. How can the change of machining parameters influence the surface quality? How is the frequency of chip serration related to this?

1.3 Innovation and Contributions

The main innovation and contributions of this thesis are summarized as follows:

1. PCD electric discharging characteristics

The relationship between gap voltage, peak current and electrical resistance of various PCD samples was identified. This study was performed with two types of PCD and one WC tool

material. The summarized results indicate a significant difference between the values of the discharging voltages and currents for the different materials.

2. Modelling instantaneous cutting force

The proposed instantaneous cutting force models are able to predict the peak value of cutting force, and predict the instantaneous cutting force. The model describes the mathematical relationship between instantaneous cutting force and machining parameters (*cutting speed*: v_c, *feed*: f_d and *axial cutting depth*: a_p).

By analyzing the influence of machining parameters on cutting force coefficients, the exponential relationships between machining parameters and cutting coefficients are revealed. The fluctuations in the instantaneous cutting force curve can be predicted by a time-dependent function.

3. Thermal characteristics in the endmilling of Ti6Al4V

A new model was developed to describe the mathematical relationship between machining parameters (*cutting speed*: v_c, *feed*: f_d and *axial cutting depth*: a_p) and the dynamic cutting temperature. This is the first time the influence of machining parameters on average cutting temperature has been revealed for the process of end milling Ti6Al4V with a PCD tool.

4. Tool wear mechanism in the ending milling of Ti6Al4V

Three failure types of PCD tool have been identified. The mechanisms of these failure types are shearing effect on the boundary of tool-chip interface, stress concentration at notch locations on the cutting edge and the uneven distribution of cutting stress on the area of contact between tool and chip.

5. Surface quality and chip morphology

The feed has been confirmed to be the most important factor affecting the final surface quality. The analysis of the cutting force indicated that larger cutting force results in worse surface quality. The study of chip morphology focused on the serration frequency of chip samples. The boundary between two different serration frequency areas on one chip was found to be at a position of 25 % of the chip length.

1.4 Thesis outline

This thesis is organized into 8 chapters. Chapter 1, this chapter, has introduced the background,

motivations, objectives and major outcomes. Chapter 2 presents the literature review and the limitation of current knowledge, and an introduction to the application of PCD material in the metalworking area.

Chapter 3 concerns the investigation into the electrical discharge characteristics of PCD material in EDM processes. The main experiment performed is aimed at solving two issues: 1/ identification of the influence of changing current value in the process, and 2/ to study the relationship between gap voltages, peak current and electric resistance of various PCD materials.

Chapter 4 describes a new cutting force model which considers the influence of machining parameters. The new expressions for cutting coefficients are proposed based on the analysis of instantaneous cutting force characteristics. The instantaneous cutting force equation is also presented.

Chapter 5 presents the thermal analysis which comprises two parts: 1/ modelling the dynamic cutting temperature and 2/ analyzing the chemical components on used PCD tools. The new model of dynamic cutting temperature proposed in this chapter describes the mathematical relationship between dynamic cutting temperature and machining parameters. Possible chemical reactions occurring at the cutting face have been identified with strict consideration of working conditions.

Chapter 6 presents the results of the investigation into tool wear form and evolutions of PCD mills applied with different machining parameters in the endmilling of Ti6Al4V process. The complete analysis of tool wear form and evolution is based on a series of tests which applied different machining parameters (*cutting speed*: v_c, *feed*: f_d, *axial cutting depth*: a_p and *cutting length*).

Chapter 7 reports the research on surface quality analysis and chip morphology analysis. The surface quality analysis focuses on the influence of machining parameters and peak value of instantaneous cutting force. The chip morphology analysis discusses the serration frequency and its associated mechanism.

The Chapter 8 summarizes the significant outcomes and contributions of this thesis. Possible future work based on this research has been presented at the end of this chapter.

2 Literature Review

This chapter presents a review of the current technology and issues associated with machining Ti6Al4V and also the applications of PCD materials in the metalworking area. The review is relevant to the research outcomes and the novel research contributions of this thesis.

The scope of this literature review focuses on the instantaneous cutting force analysis of machining Ti6Al4V with turning and milling processes, the dynamic cutting temperature and chemical analysis of conventional tool materials and PCD after use in machining Ti6Al4V. The review concentrates on the published literature concerning aspects of tool performance including analysis of the tool wear mechanism analysis tool wear evolution. Studies of surface quality and chip morphology are another important area relevant to this thesis work so these are also been reviewed in the follow sections.

The limitations of current knowledge have been identified through this literature review. A number of associated issues are also discussed in this Chapter. Figure 2.1 outlines the literature review topics covered in this chapter.

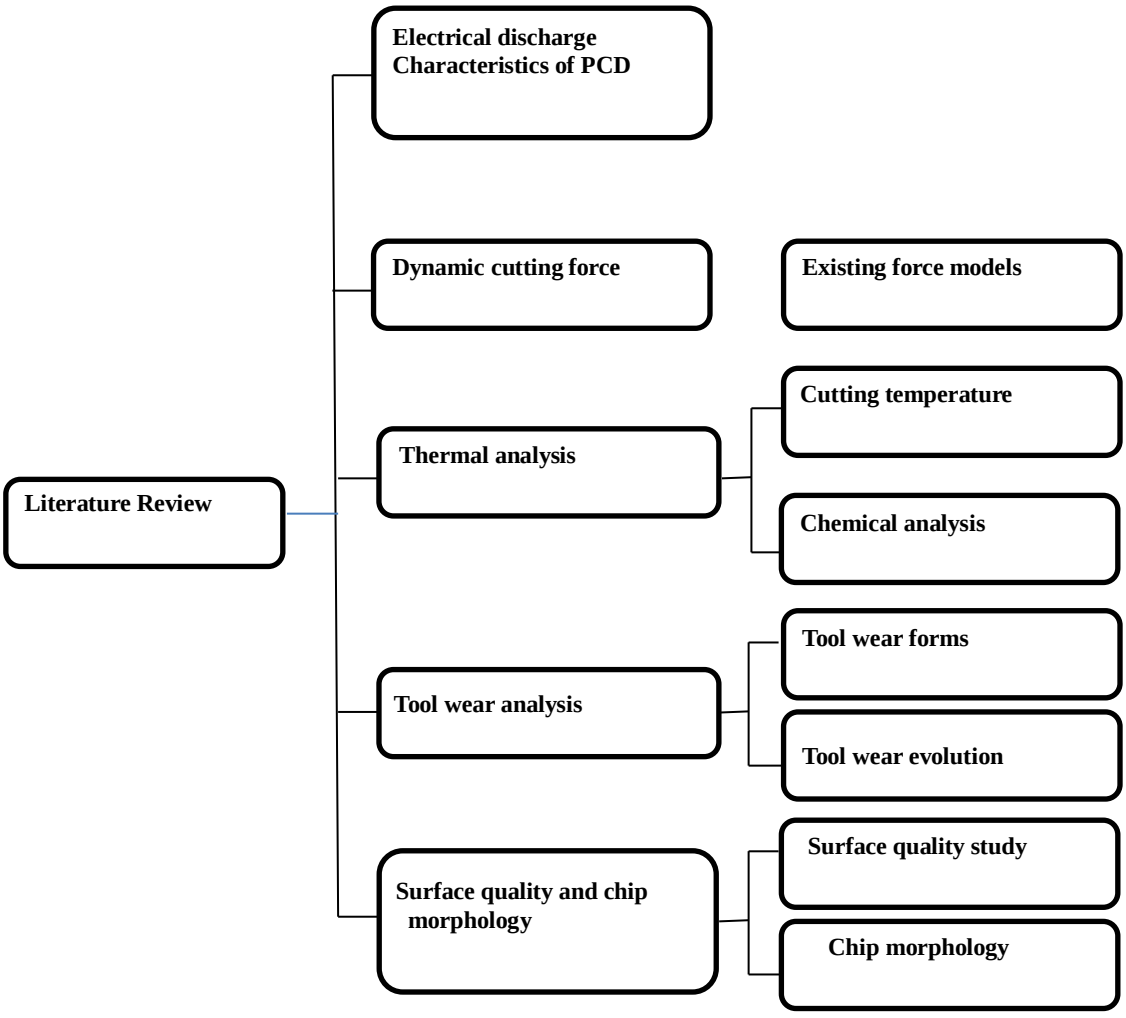

Figure 2.1- Literature review topic outline.

2.1 Machining Ti6Al4V and applications of PCD

2.1.1 Machining Ti6Al4V

The high strength-to-weight ratio and its great corrosion resistance make Titanium alloy Ti6Al4V a popular material for use in the aerospace, biomechanical, marine and chemical industries. However, due to its low thermal conductivity [6], Ti6Al4V is difficult to machine. For the past decades, many tool materials have been tested for machining this kind of alloys. These tool materials include High Speed Steel (HSS), normal tool steel, tungsten carbide (WC), (Polycrystalline Cubic Boron Nitride) PCBN, (Polycrystalline Diamond) PCD, CVD diamond (Chemical Vapor Deposition diamond), TiAlN, etc.

Sun and Gao applied TiAlN in the endmilling process of Ti6Al4V for studying the surface integrity [7]. The ranges of cutting speed, feed, radial cutting depth and axial cutting depth were 50 m/min - 110 m/min, 0.08 mm/tooth - 0.14 mm/tooth, 4 mm - 6 mm, 1.5mm, respectively. Water-soluble coolants were used. The surface roughness, residual stress and micro hardness were investigated. The results show that the largest residual normal stress was obtained when the cutting speed was set to 80 m/min and the micro hardness of finished surface was 70-90 % larger than the bulk materials. Bhaumik et al. [8] tried the material wBN-cBN in the turning process. This kind of material has a fracture toughness of 13-16 Mpa/m^2, hardness of 40-70 GPa and the elastic modulus of 760 GPa. The cutting speed, feed and axial cutting depth were 75 m/min, 0.1 mm/tooth and 0.5 mm. The cooling method was the same as Sun's experiment and excellent tool performance was found. Ezugwu et al. [9] applied the three different grains sizes of CBN tool material in the turning process of Ti6Al4V. The cutting speed that was applied was between 150 m/min - 250 m/min. The ranges of the other machining parameters were similar to Sun's experiment and the same high pressure cooling system was also applied in the process. The surface investigation showed that there was no adverse effect found on the finished surfaces.

However, some research works have also reported bad tool performance in the machining Ti6Al4V. Tungsten Carbide and Cubic Boron Nitride (CBN) tools have been used in milling Titanium alloys with reasonable results at low cutting speed of less than 90 m/min [10]. However, when they are applied at high cutting speed (larger than 100 m/min), the tool life becomes unacceptably short. According to our previous research [11], the longest tool life achieved was 0.32 hour when the material removal rate (MRR) was 1069.4 mm^3/min, and 7.57 hours when the MRR was 76.3 mm^3/min but in many cases the tool lasted for only a few

minutes. With the increased utilization of Titanium alloys in aerospace, medical and automotive industries, there is a pressing need for new cutting tools to improve productivity.

2.1.2 Applications of PCD

Diamond is one of the hardest materials in the world. Polycrystalline diamond (PCD) is made by sintering together diamond particles of 1 - 30 microns in the presence of a cobalt catalyst to produce an inter-grown mass of diamond grains by applying high temperature and pressure. The significant hardness and the excellent thermal conductivity [12] make PCD the most promising tool material for the machining of Titanium alloys.

Recently, PCD tools have been successfully used in the turning of Titanium alloys. Ezugwu et al. [13] studied the surface integrity after turning Ti6Al4V alloy with PCD tools using conventional and high pressure coolant supplies. Micrographs of the machined surfaces showed that the surface had been damaged by the formation of micro-pits and the presence of re-deposited work material. Rosemar et al. [1] investigated the behavior of PCD tools in turning Ti6Al4V alloy at high speed using high pressure coolant supplies. They found that an increase in coolant pressure tended to improve tool life and reduce the adhesion tendency. By studying tool wear of PCD inserts in turning Ti6Al4V, Schrock and Kwon et al. [14] found evidence of phase transformation and they concluded that a significant difference in wear existed between two different tool materials at low cutting speed. The wear was a result of the transition from alpha to beta phase in the titanium workpiece material. This conclusion is different from that made by Koenig and Neises [4]. They found that the binder phase and particle size of the PCD were the two factors which determined tool wear. Emmanuel investigated the surface integrity and tool performance of PCD by applying different cooling conditions in the turning processes [13]. The experimental results show the good performance of PCD tools with the high pressure cooling methods. Amin found that PCD tools had better wear resistance when compared to tools made of Carbon Tungsten [5].

In addition to turning operations, PCD has been applied in the milling of Titanium alloys but with tools of relatively large dimensions. In 1998 Kuljanic et al. [15] investigated the possibility of applying PCD in end milling with a tool of 32 mm in diameter. A tool life of 381 minutes was achieved when the cutting speed was 110 m/min and feedrate was 0.125mm. By using an end milling tool of 32 mm in diameter, Amin et al. [5] achieved the MMR of up to 59.87 mm^3/min while the tool life was almost twice as long as that WC-Co milling cutters. In order to analyse the wear mechanisms of PCD tools, Li et al. [16] conducted a series of cutting tests using an end PCD mill of 125 mm in diameter, and found that PCD tools exhibited relatively

little edge chipping and low flank wear at cutting speed of 250 m/min. This is the speed they found to be the best for PCD tools when machining Ti6Al4V titanium alloy. Similar research has also been conducted by Ota et al. [17]. PCD tools were found to have excellent flank wear resistance compared with conventional cemented carbide tools, and unprecedently high cutting speeds became possible by use of PCD tools with the application of high pressure coolant. Anhai et al. [18] performed an analysis of tool failure mechanisms in an experiment involving face milling Ti6Al4V with a PCD tool. The adhesive and abrasive fractographs were reported as was the profound effect of cutting speed on the PCD tool wears. Also, a research to optimizing machining parameters for high-speed milling Ti6Al4V with PCD tool was carried out by Gert et al. [12].

2.2 Electrical discharge characteristics of PCD materials

2.2.1 The discharge waveforms

For the several past decades, EDM methods have been used for machining many different materials. Generally, the analysis of discharge waveforms, which includes the investigation of the influence of changing machining parameters, is very important in optimizing the parameters to improve the surface quality and material removal rate. Normally, there are four gap states for EDM processes: Normal sparking, Open circuit, Arc and Short circuit. Figure 2.2 shows the discharge waveforms which are discussed by Lin et al. [19]. The applied workpiece material was SKD 61 steel. The electrode was copper and the dielectrical fluid was kerosene. Arcing and normal sparking are compared.

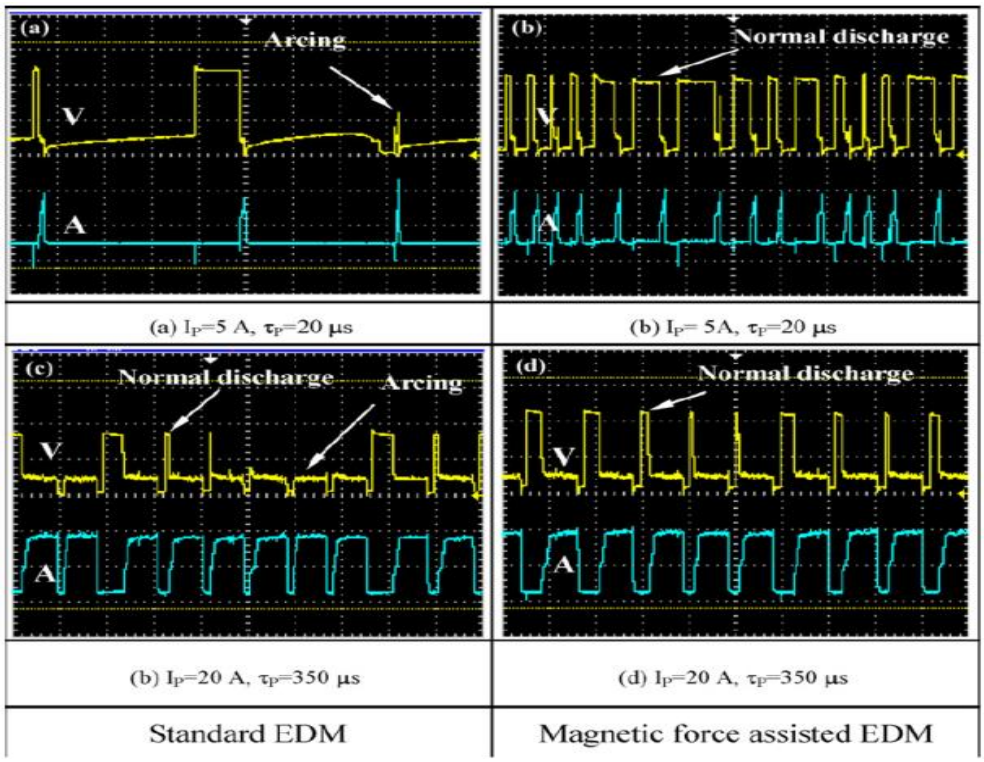

Figure 2.2 - The discharging waveforms of SKD 61steel [19].

Except for "Normal sparking" and "Open circuit", the other gap states can damage the surface finish and shorten the tool life. Several methods for predicting the gap states using the discharge waveforms have been proposed in many research works. Yan and Chien presented the method of defining the gap states by monitoring the gap voltage waveform [20]. By analyzing the characteristics of discharge waveforms, the influences of pulse interval, feed and workpiece thickness on the proportion of these four gap states were identified. Long pulse intervals and high feeds were concluded as the important reasons for a high ratio of short circuit pulses to normal pulses. The characteristics of the discharge waveforms can also reflect the performance of the power supply in the EDM process. For example, by analyzing the discharge waveform, the discharge energy which affects the gap distance can be evaluated. Yeo proposed a method to improve the tool wear compensation of a micro-EDM process. In this work the author developed a new electro-thermal model which used an associated online monitoring process [21]. In the study of optimizing machining parameters for a magnetic force assisted EDM process, Lin et al. [19] investigated the discharge waveforms. The discharge waveforms of voltages found in this experiment were higher than that of standard EDM process. In Garn's study of vibration's effect on a micro-EDM process [22], the mechanism of the discharging action was be derived based on analysis of the discharge waveforms.

The influence of the peak current on the discharge voltage is one of the important aspects of an EDM process. In Gurgui's analysis [23], the setting of peak current has a significant effect on

the discharging voltage and the surface quality. This study was about the machining of Micro-cavities with an EDM method. The electrode was copper, the dielectrical fluid and ONA oil and the workpiece was stainless steel. Excellent geometric accuracy was achieved when the peak current was 1 A.

2.2.2 The process of machining PCD by EDM

Because PCD contains conductive phases, the EDM process is suitable for machining PCD materials. In term of the cost compared to conventional process, EDM would be the better solution for machining this kind of material, due to the extremely high hardness. In the past few decades the development of EDM for machining PCD materials has been discussed in many research works. For example, by investigating the machining characteristics of PCD materials in the EDM process, Hsu et al. [24] found that the grain size and open circuit voltage significantly affect the result of Material Removal Rate (MRR) and working area. He also reported a MRR increase with increasing peak current and open circuit voltage. In his summaries of machining PCD with grinding and EDM methods, Tso and Liu [25] pointed out that a better surface finish could be achieved by using grinding processes rather than EDM methods. To improve the machinability of PCD materials, a new PCD material which contains electrically conductive diamond particles has alos been developed and tested by Iwai et al. [26]. Gao presented the process of WEDM machining of PCD materials which was aimed at optimizing the roughing operation and finishing operation [27]. According to the analysis of his experimental results, the peak current and open circuit voltage pulse were found to have a significant influence on roughing and finishing operations. The cutting edge radius achieved was 6.7 μm.

2.2.3 The limitations of current research in electrical discharge characteristics of PCD

Electrical Discharge Grinding (EDG) is the grinding process which applies the EDM method. In EDG the workpiece is machined with a rotating electrode which means that the sparking spot is different for each discharge pulse. Currently, there is few research works focus on the process of machining PCD with EDG method. To apply EDG in machining PCD materials, the short circuit can be prevented in the process when the grinder keeps rotating. The study of discharge waveforms is important for machining PCD with an EDG process. By analyzing the discharge waveforms, the gap states and discharging voltage can be monitored. Furthermore, the influence of peak current on the discharge voltage is relevant to the evaluation of machining efficiency metrics such as MRR (m^3/min) which can be analyzed in the future.

2.3 Instantaneous cutting force

2.3.1 Existing cutting force model

In existing cutting force models, two popular methods have been used: The Finite Element Method (FEM) and the analytical method. By using FEM to simulate the cutting process, there are many advantages:

1. More convenient than the analytical method because of the existing constitutive equation of material.
2. Can simulate processes with a wide range machining parameters.
3. More suitable for simulation of the dry cutting process.
4. Can consider the softening effect and strain hardening effect as part of the simulation.
5. Easier to obtain accurate stress, strain and temperature distributions.

One of the FEM cutting models has been developed by Rao [28] with AdvantEdge^{TM} software. In this study, the Johnson - Cook constitutive equation was applied for describing the stress - strain relationship and the material failure criterion. This material equation is a purely empirical function which was summarized by Johnson and Cook in 1983 based on experimental analysis [29]. Their expression is as Equation (2-1).

$$\sigma = (A + B\varepsilon_p^n)(1 + C\ln(\frac{\dot{\varepsilon}}{\dot{\varepsilon}_o}))(1 - (\frac{T - T_r}{T_m - T_r})^m) \tag{2-1}$$

Where *A, B, C, n, m* are material constants, ε is strain and strain rate is

$$\dot{\varepsilon} = \varepsilon / t \text{ , } t : time \tag{2-2}$$

Also, T, T_r, T_m are working temperature, room temperature (=25^o) and melting temperature of Ti6Al4V respectively.

Four groups of material constants from different studies were applied for the cutting model. The comparisons of prediction and experimental results have reasonable agreement. The detailed stress and temperature distributions are shown in Figure 2.3. It can be seen that the highest stress and temperature appear at the cutting edge.

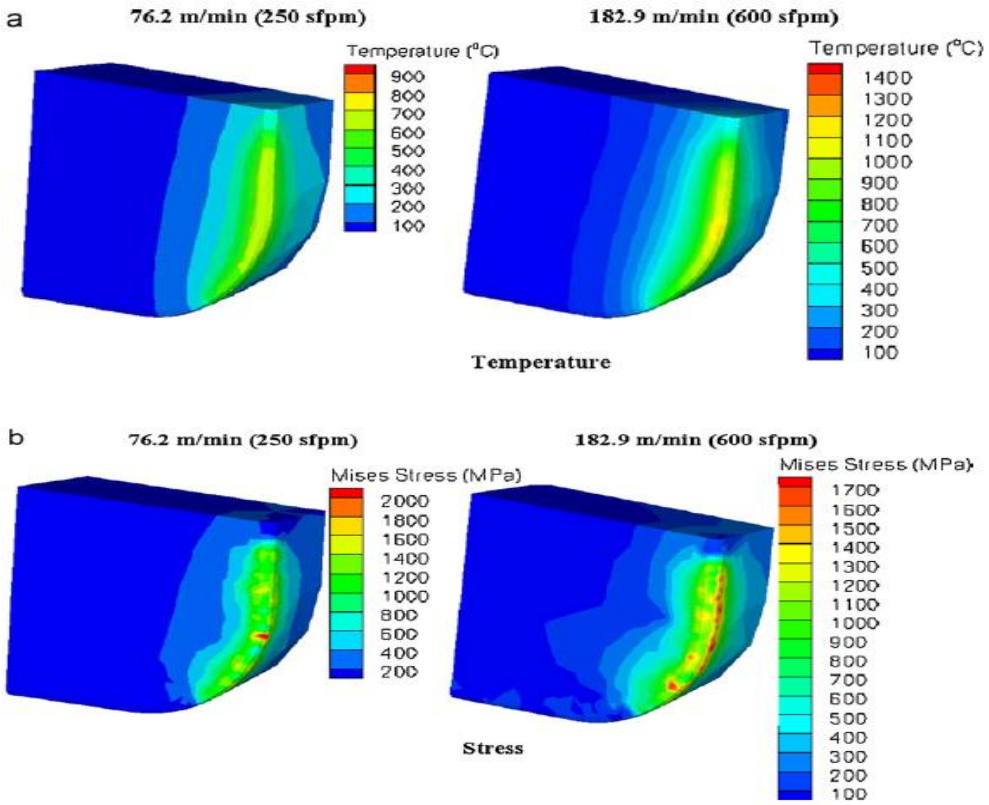

Figure 2.3 - The FEM simulation result of milling process: (a) the distribution of cutting temperature; (b) the distribution of stress [28].

However, the FEM simulation also has some obvious disadvantages:

- The limitation of simulating the process with long cutting length. The calculation task for long cutting length requires a high performance computer with a great deal of storage space in order to be accomplished in a reasonable time frame. Therefore, the long-term machining processes such as vibration or chatter cannot be studied easily.

- The limitation associated with considering the tool wear evolution in the process. Tool wear evolution simulation can only be performed using a long-term cutting simulation which, as mentioned above, is hard to be achieve.

- The limitation of material constitutive equations. There are limited constitutive equations available in commercial FEM software. And these involved equations cannot describe the dynamic behavior for all materials. In addition, they cannot describe materials operating under special working environments (e.g. evaluated temperature, high impact speed or chemical reaction). In summary, the constitutive equations are not applicable in many relevant situations.

In contrast, the analytical cutting force model based on the analyzing the geometrical parameters

and cutting forces, can achieve higher accuracy of predicting cutting force. The cutting force coefficients were introduced into the expressions of force components. Generally, there are three different directions of developing analytical cutting force model:

- The algorithm for calculating the cutting force coefficient.
- The algorithm which focus on geometrical parameters of machining process.
- The algorithm based on the analysis of the energy transfer.

Cutting force expressions and cutting force coefficients

Over the past decade, many researches have been carried out concerned with the prediction of instantaneous cutting force by calculating the cutting coefficients and deducing the algorithm of tool geometric parameters. Yun and Cho developed a cutting force model which could determine the constant cutting force coefficients and runout parameters of an endmilling processes [30]. For this study, the cutting force coefficients (K_n and K_f) and chip flow angle (θ_c) were assumed to be relevant to the geometrical parameters of cutter and properties of cutter and workpiece. If these two factors remain unchanged in an experiment, the cutting force coefficients and chip flows can be assumed as constants. According to Yun and Cho, the expressions of cutting force components in Cartesian coordinates is

$$\begin{cases} F_x = [C_1 K_n \cos(\phi - \alpha) + K_f K_n C_3 \cos\phi - K_f K_n C_4 \sin(\phi - \alpha_r)] t_c(\phi) B_1 \\ F_y = [C_1 K_n \sin(\phi - \alpha_r) + K_f K_n C_3 \sin\phi + K_f K_n C_4 \cos(\phi - \alpha_r)] t_c(\phi) B_1 \\ F_z = [-C_2 K_n + K_f K_n C_5] t_c(\phi) B_1 \end{cases} \quad (2\text{-}3)$$

Where C_1, C_2, C_3 and $B_1$are geometrical parameters.

The coefficient K_n equals to the value of K_T applied in Chapter 4. The t_c represents the uncut chip thickness which is related to the feed:

$$t_c = f \sin\phi \quad (2\text{-}4)$$

Where f is the feed and ϕ is the rotation angle of cutter. The expression (2-3) shows clearly that the instantaneous cutting force components are determined by the instantaneous chip thickness which means that, only the value of feed can affect the cutting forces.

Some studies assumed that the cutting force coefficients could be affected by changes in the machining parameters. Lee and Lin introduced a 3D cutting force model based on the study of

the end milling freeform surface [31]. The cutting force coefficients in this model were considered as functions of chip thickness:

$$\begin{cases} K_c = 569.14 t_c^{-0.283} \\ K_f = 0.1468 t_c^{-0.364} \end{cases} \tag{2-5}$$

Where K_c equals to the value of K_T applied in Chapter 4.

Similar expressions have been given based on the investigation of runout effect in an endmilling process by Kline and DeVor [32]. He also believed that the instantaneous uncut chip thickness was the key factor for the coefficients.

Based on the curve fitting experimental results, the different expressions of cutting force coefficients were given by Wan et al. [33] as Equation (2-6).

$$\begin{cases} K_t = W_{t1} + W_{t2} e^{W_{t3} t_c} \\ K_r = W_{r1} + W_{r2} e^{W_{r3} t_c} \\ K_z = W_{z1} + W_{z2} e^{W_{z3} t_c} \end{cases} \tag{2-6}$$

Where W_{t1}, W_{t2}, W_{t3}, W_{r1}, W_{r2}, W_{r3}, W_{z1}, W_{z2} and W_{z3} are calculating coefficients. It can be seen from the Equation (2-6) that the cutting force coefficients have an exponential relationship to the chip thickness which is determined by feed.

In Wu's study of a circular end milling process [34], the cutting coefficients of tangential, radial and axial force components are expressed with polynomial forms which were derived using curves fitting methods based on experimental results. But the mode includes only a single variable - radial depth of cut. The expressions of cutting force coefficients are as Equation (2-7).

$$\begin{cases} K_T = -2.92 d_e^3 + 51.82 d_e^2 - 309.3 d_e + 2727 \\ K_R = -1.618 d_e^3 + 39.85 d_e^2 - 318.7 d_e + 1947 \\ K_Z = -2.055 d_e^3 + 34.54 d_e^2 - 183.0 d_e + 603.5 \end{cases} \tag{2-7}$$

Where d_e is radial depth of cut.

The effect of cutting speed and feed

According to the conclusions reached by various researchers [35, 36], a change of machining parameters could lead to the strain hardening effect or heat softening effect which can affect the final values of cutting forces. As indicated in the discussion of the FEM model in this section,

the strain hardening and softening effect can be taken account of by using the constitutive equation of Johnson-Cook. Generally, an increase in the cutting speed and feed will cause a corresponding increase in strain and finally lead to strain hardening. Another consequence of increasing the speed and feed machining parameters is more heat generation in the process which will soften both the workpiece and the cutter. However, most cutting force models barely consider the influence of changing these machining parameters (cutting speed, feed and axial cutting depth). This is despite the fact that, the effects of varying cutting speed, feed and axial cutting depth can be seen from many published experimental results. According to Ali's analysis [37], when the values of feed changed from 80 mm/min to 160 mm/min, the main cutting force increased from 510 N to 620 N. Barry et al. [35] studied the cutting forces in the process of machining Ti6Al4V. From his result, it is easy to see the influence of cutting speed and feed in the machining process from the following pictures, see figure 2.4.

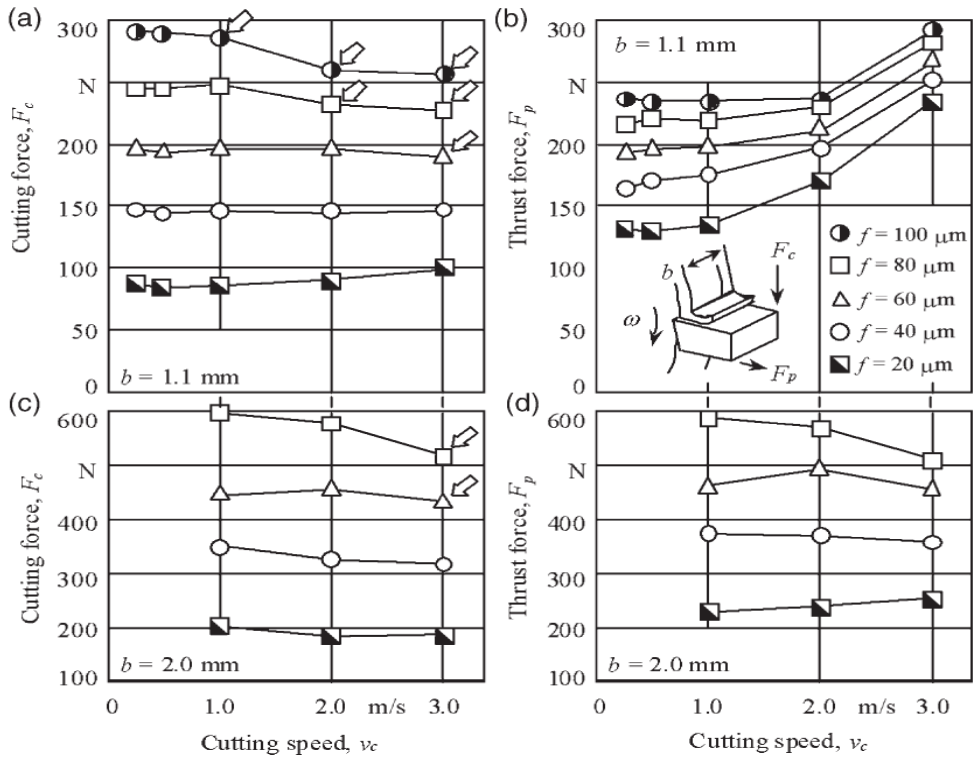

Figure 2.4 - The cutting forces in different working conditions [35].

Other factors for calculating cutting force

Wang developed an end-milling cutting force model by considering the instantaneous shear plane area, cutter geometry, vibration, and some other, less important factors [38]. The runout effect can directly affect instantaneous uncut chip thickness. Some researchers believed that this is important factor that needed to be taken account in the modeling. Yang et al. [39] proposed a new cutting force model by integrating the effect of runout for the milling of curved surfaces.

Similarly, Lamikiz et al. [40] developed a model for the milling of sculptured surfaces but focused on the analysis of the tool-chip contact area. Kline and DeVor [32] found that the presence of runout also increased the average chip thickness for those teeth actually engaged in the cut and increased the ratio of the maximum to average force.

2.3.2 The limitations of current research in cutting force model

The influences of cutting speed and feed have not been taken into account in most existing cutting force models. Therefore, these models can not completely reflect the characteristics of cutting force found in real life machining processes. For accurately predicting the cutting force, it is necessary to develop a new cutting force model which considers the influence of machining parameters. Moreover, obtaining time-dependent cutting force function is also important for predicting the fluctuation of the cutting force.

2.4 Thermal analysis

Seeking to improve machinability, many researches have been conducted studying the thermal effects in milling Ti6Al4V with focus on the analysis of cutting temperature, chemical components and chip morphology. Rosemar found segmented chips in experiments with high pressure cooling and continuous chips tests with a conventional cooling system [1]. Mohd Hadzley et al. successfully developed the Finite Element Method (FEM) model for the process of machining Ti6Al4V with high pressure cooling, this correctly predicted the cutting temperature and the form of the chip [2].

2.4.1 Cutting temperature

The cutting temperature is a factor which directly reflects the heat generated in the machining process. Ti6Al4V has extremely low thermal conductivity, the heat dissipation is worse than other commonly machined metals. The cutting temperature always remains at a very high level and this may cause chemical reaction or material diffusion.

Temperature measuring methods

Various methods have been used for the measurement of cutting temperatures. For example, Le Coz successfully applied a thermocouple system in the test of dry milling Ti6Al4V [41]. By setting the thermocouple sensor on the tool tip, the system was able to directly monitor and record the dynamic temperature of the tool. In the experiment conducted by Sato et al. [42], the

proposed system consisted of an infrared radiation pyrometer, optical fiber and a fiber coupler. In addition, Pittalà and Monno used an infrared thermal camera to directly measure the temperature of the cutting zone [43]. By comparing this method with other approaches, the infrared Camera (IRC) was found easy to use and was more practical in most milling systems.

Existing cutting temperature models

The prediction of cutting temperature is necessary for many aspects of metalworking such as evaluating the tool performance and workpiece surface integrity. Due to friction and shearing effects, the cutting heat causes an elevated temperature at the tool-chip interface. For Ti6Al4V, which has the thermal conductivity around 6.4 W/mK, the cutting temperature of the tool-chip interface often rises above 500o in conventional processes. This can cause problems because the chemical affinity of this alloy is very high in these high temperature working environments. Therefore, the development of a cutting temperature model is needed.

For recent years, various cutting temperature models have been proposed based on the analysis of experiments with different materials. There are two major types of models and these are referred to as FEM and analytical. One of the successful FEM cutting temperature models was proposed by Pittalà and Monno with the OXCUT software [43]. This 3D thermal model was developed for predicting the cutting temperature in the face milling operation of Ti6Al4V. In order to simulate the thermal gradient on the tool-chip interface, the heat coefficient was set to 10^4 N/s/mm/^{o}C. And the thermal properties of Ti6Al4V are list in Table 2.1. The Johnson-Cook constitutive equation was applied by Pittalà to describe the material mechanical behavior of Ti6Al4V. The final prediction highly agrees very well with the experimental result under different machining conditions.

Table 2.1 Thermal properties of Ti6Al4V [43]

Heat capacity ($\times 10^6$ J/m^{3}K)	Conductivity (W/(mK))
2.35(0^{o}C)	7(0^{o}C)
2.52(200^{o}C)	8.6(200^{o}C)
2.76(400^{o}C)	11.5(400^{o}C)
3.5(600^{o}C)	14.4(600^{o}C)
3.9(800^{o}C)	17.2(800^{o}C)

List et al. [44] developed another thermal model by using AbaqusTM software. This model focused on the high speed machining process (above 20 m/s) and it also considered the crater wear effect. The predictions of cutting forces, contact length and temperature with this model

also have a high correlation with experimentally obtained results.

Some research works focus on the development of analytical cutting temperature models based on the method of solving the heat diffusion equation. For example, in the study of a high-speed milling process, Chen et al. provided an analytical thermal model for predicting cutting temperature [45]. The cutting temperature and heat flux prediction were based on a method for solving the Equation below (2-8) with assumed boundary conditions.

$$\lambda\left(\frac{\partial^2 T}{\partial x^2}+\frac{\partial^2 T}{\partial y^2}+\frac{\partial^2 T}{\partial z^2}\right)-\rho c f\,\frac{\partial T}{\partial x}=\rho c\,\frac{\partial T}{\partial t} \tag{2-8}$$

Where λ, T, ρ, c, t are the thermal conductivity, temperature on workpiece, density, specific heat capacity and time respectively. And (x, y, z) are the locations of the measuring point. Also, the heat flux q_M was given as

$$q_M = q^*_{M-1}+\frac{\sum_i^r (Y_{i,M}-T_{i,M})X_{i,M}}{\sum_i^r X_{i,M}^2} \tag{2-9}$$

Where $T_{i,M}$ is the computed temperature from Equation (2-8); $X_{i,M}$ is the sensitivity coefficient; $Y_{i,M}$ is the surface temperature; q^*_{M-1} is the Taylor series expanded part of $T_{i,M}$.

For this model, the cutting speed was contained in the calculation of dimension. According to the prediction of this model which is shown in Figure 2.5, the cutting speed affected the cutting temperature significantly. Also, the heat flux dropped when critical cutting speed was exceeded.

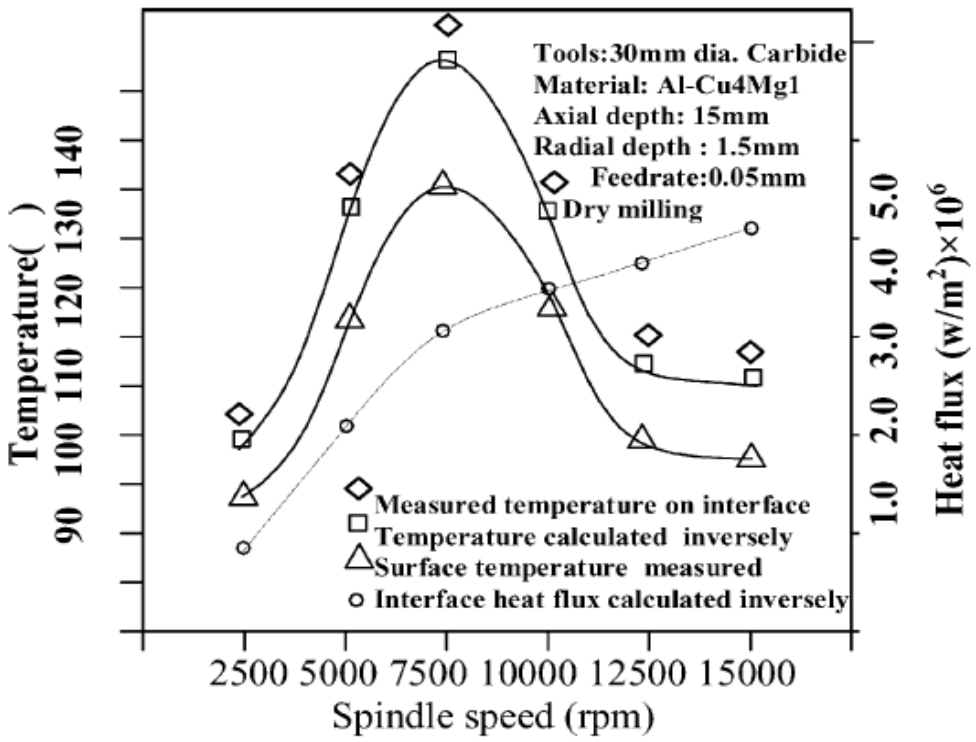

Figure 2.5 - The comparison of prediction and experimental results [45].

The specific cutting temperature functions of an arbitrary point on workpiece or cutter are given in some research works. For example, in Lin's study [3], the cutting temperature function of single point was expressed as Equation (2-10).

$$T = \frac{Q}{8c\rho\sqrt{\pi\alpha\tau}} J \tag{2-10}$$

Where the Q is the heat generated in the machining process and the expression for J is

$$J = (erf(\frac{x}{\sqrt{4\alpha\tau}}) - erf(\frac{x-W}{\sqrt{4\alpha\tau}})(erf(\frac{z}{\sqrt{4\alpha\tau}}) - erf(\frac{z-L}{\sqrt{4\alpha\tau}})) \tag{2-11}$$

Where (x,z) are the co-ordinates of the measuring point; W, L, α, τ are the width of the heat source, length of heat source, thermal diffusivity and time respectively.

Equation (2-10) was also derived from the heat diffusion equation, however, it can be clearly seen that the value of J is determined by the co-ordinates of the measuring point and material properties such as heat capacity (c) and density (ρ) were assumed to be constants.

In Lin's study, the final heat generation Q contains two different parts:

The heat generation from shearing effect:

$$Q_s(\tau,z)=\frac{V_s F_{s,j}(\tau,z)}{z\csc\phi_n h_j(\tau,z)\sec\beta} \tag{2-12}$$

Where V_s, $F_{s,j}(\tau,z)$, z, $h_j(\tau,z)$, ϕ_n, β are shearing speed, shearing force, axial cutting depth, uncut chip thickness, normal shearing angle and tool helix angle.

The heat generation from friction effect:

$$Q_f(\tau,z)=\frac{VF_{tf,j}(\tau,z)}{zVB\sec\beta} \tag{2-13}$$

Where V, $F_{tf,j}(\tau,z)$, VB are cutting speed, friction force and tool flank wear width.

From the Equation (2-12) and (2-13), the relationship between cutting speed and heat generation is clear.

However, generally, the changes of machining parameters will also cause the changes of shearing force and friction force.

An additional useful piece of information is that, according to Cui's study, the expression of heat generation was summarized into the purely empirical form [46]:

$$Q=5.295\cdot10^{14}\cdot h^2-4.414\cdot10^{14}\cdot h+2.066\cdot10^{8} \tag{2-14}$$

Where h equals to the uncut chip thickness.

By comparing the expressions of Equation (2-12) and (2-13) with Equation (2-14) it is clear the last equation is more convenient to apply in evaluating the heat generation. However, this expression is limited to certain working conditions.

Influence of machining parameters

The cutting temperature is sensitive to the machining parameters such as cutting speed (vc,m/min), feed (ft, mm/tooth) and axial cutting depth (ap, mm). Ugarte et al. [47] used an IRC in the milling of Ti6Al4V and he found the temperature rose with an increase of cutting speed. Similarly, in turning EN-31 steel alloy with carbide tools, Abhang and Hameedullah found that cutting temperature rose with an increase of v_c, f_t and a_p [48]. This conclusion also agrees with the analysis of micro-milling Aluminum alloy with TiAN tools by Zhou et al. [49].

2.4.2 Chemical analysis

As is well known, the process of machining Ti6Al4V always suffers the elevated cutting temperature. The chemical affinity between most tool materials and this alloy is very high when the cutting temperature is above 500^{o}. According to Machado and Wallbank, chemical reaction (e.g. oxidation or graphitization) and material diffusion are two forms of damage which frequently occurred in the process of machining Ti6Al4V [50]. By using the X-Ray Diffraction (XRD) method, the chemical components remaining on the tool can be identified and the cutting temperature can be deduced indirectly by checking against the temperature at which chemical reaction or material diffusion take place. Deng has applied the XRD method in the study of turning Ti6Al4V with WC tools [51]. The analysis shows that the W and Co had much higher rates of material diffusion when the working temperature was up to 600 ^{o}C when compared to the rates at encountered at 400oC. This material diffusion caused the hardness of cutter to be reduced. In the process of turning Ti6Al4V with PCD tools, Koenig and Neises [4] also found that the material diffusion occurred. These results also agree with the analysis by Amin in milling Ti6Al4V with both WC tools and PCD tools [5].

2.4.3 The limitations of current research in thermal analysis of endmilling Ti6Al4V with PCD tools

Most analytical cutting temperature models do not clearly reflect the influences of machining parameters such as cutting speed, feed and axial cutting depth. Also, there is no recent thermal study of endmilling Ti6Al4V with PCD tools. In particular, a cutting temperature model, the consideration of the influence of machining parameters, has not been developed. In addition, chemical analysis of used PCD tools also has not been performed. For the application of PCD in endmilling Ti6Al4V, the cutting temperature and chemical analysis are needed.

2.5 Tool wear study

2.5.1 Tool wear in conventional tool materials

The mechanical strength of Ti6Al4V is very high and the working temperature of this alloy is up to 500 ^{o}C. Therefore, for many tool materials, the tool life is extremely short when machining Ti6Al4V in comparison with that expected when machining steel. Jawaid et al. [52] studied the tool wear mechanism for the face milling process. The tool materials were PVD-TiN and CVD-TiCN+Al_2O_3. The tool rejection criteria in this study are: (a) average flank wear = 3.5 mm;

(b) maximum flank wear =0.7 mm; (c) excessive chipping/flaking or fracture of the cutting edge. For Jawaid's study, the influence of cutting speed on tool life has been summarized in Figure 2.6. From the aspect of material removal rate, better tool performance was found from CVD tool when compared with the performance of PVD tools. In this experiment, the major wear mechanisms were delamination, adhesion of work material, attrition, diffusion, plastic deformation and thermal cracks. These situations are shown in Figure 2.7 which is also taken from the Jawaid's experiment.

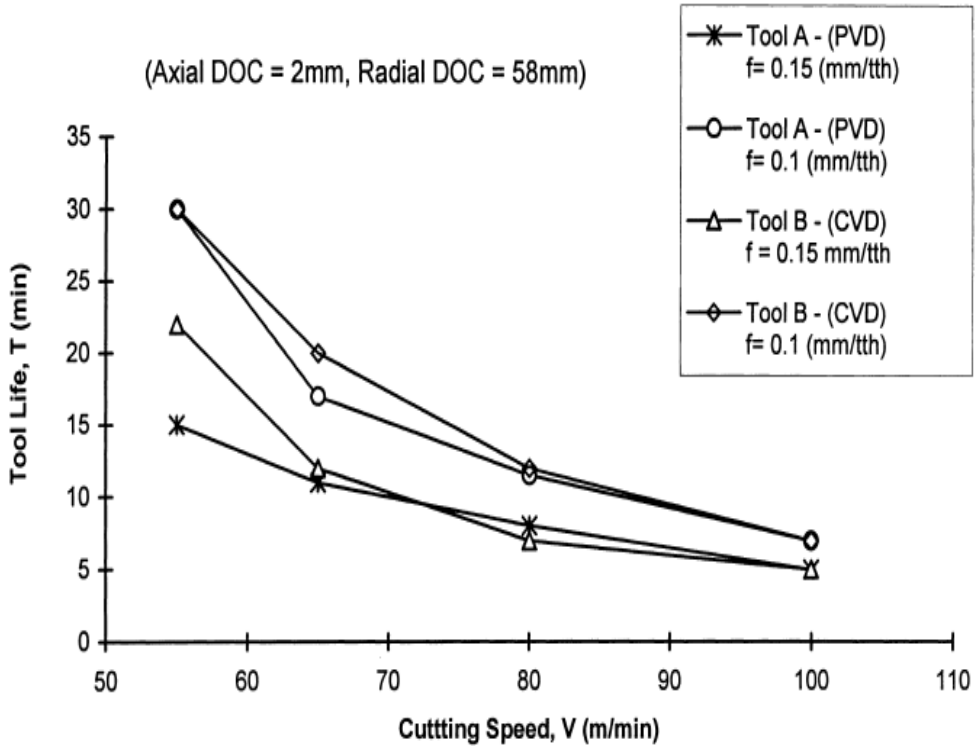

Figure 2.6 - The influence of cutting speed on tool lives [52].

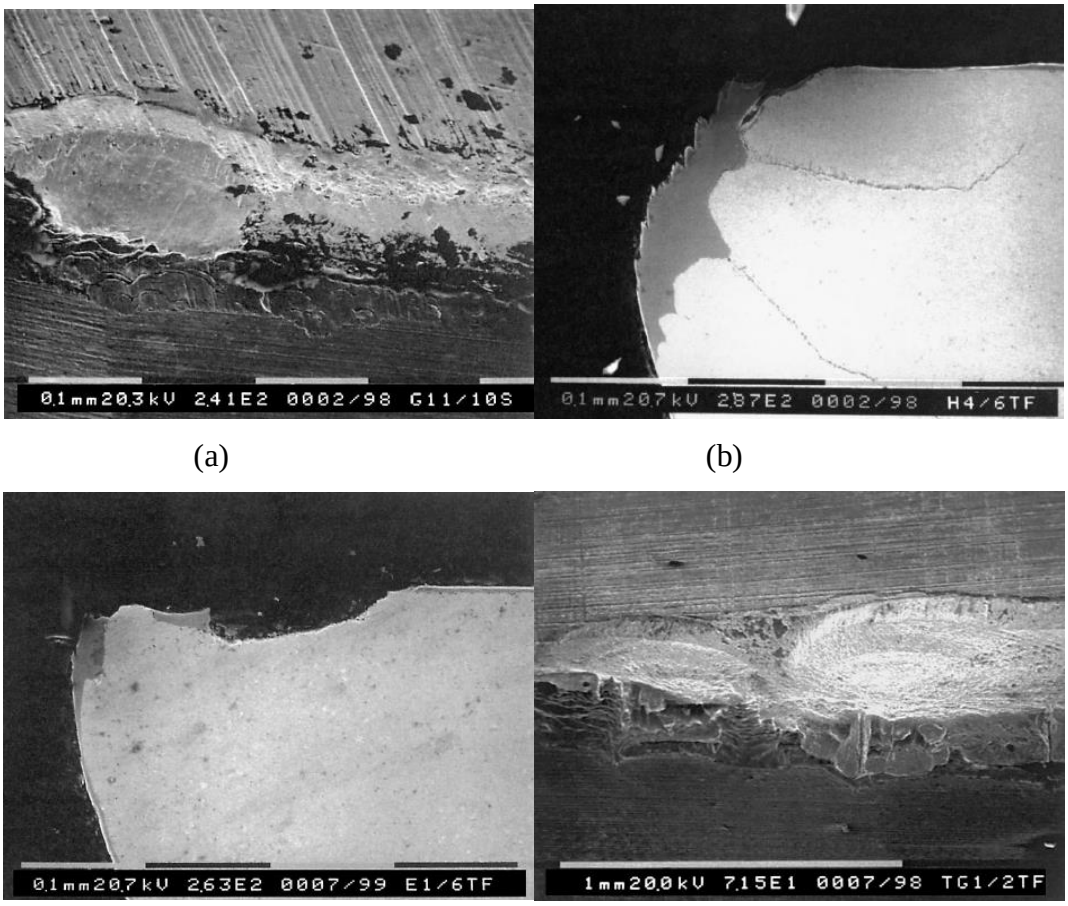

(a) (b)

(c) (d)

Figure 2.7 - The different tool wears: (a) delamination; (b) plastic deformation; (c) Adhesion of workpiece material; (d) cracks and severe flaking [52].

Oosthuizen et al. [12] investigated material diffusion in high speed machining of Titanium alloys. Evidence of diffusion between Carbide and Titanium was found and this was considered the major wear mechanism.

In the study of high-speed milling Ti6Al4V with Binderless Cubich Boron Nitride (BCBN) tools, Wang et al. [10] analyzed the tool wear evolution in different working conditions. As shown in Figure 2.8 shows which is quoted from Wang's study, the maximum cutting time is close to 9 mins before the flank wear reached 0.4 mm when the cutting speed was 300 m/min, feed was 0.125 mm/r and axial cutting depth was 0.075 mm. It can also be seen from Figure 2.8 [5] that the increase in machining parameters would affect the tool life. Wang also pointed out that adhesion to the workpiece and attrition were found as two major wear mechanisms.

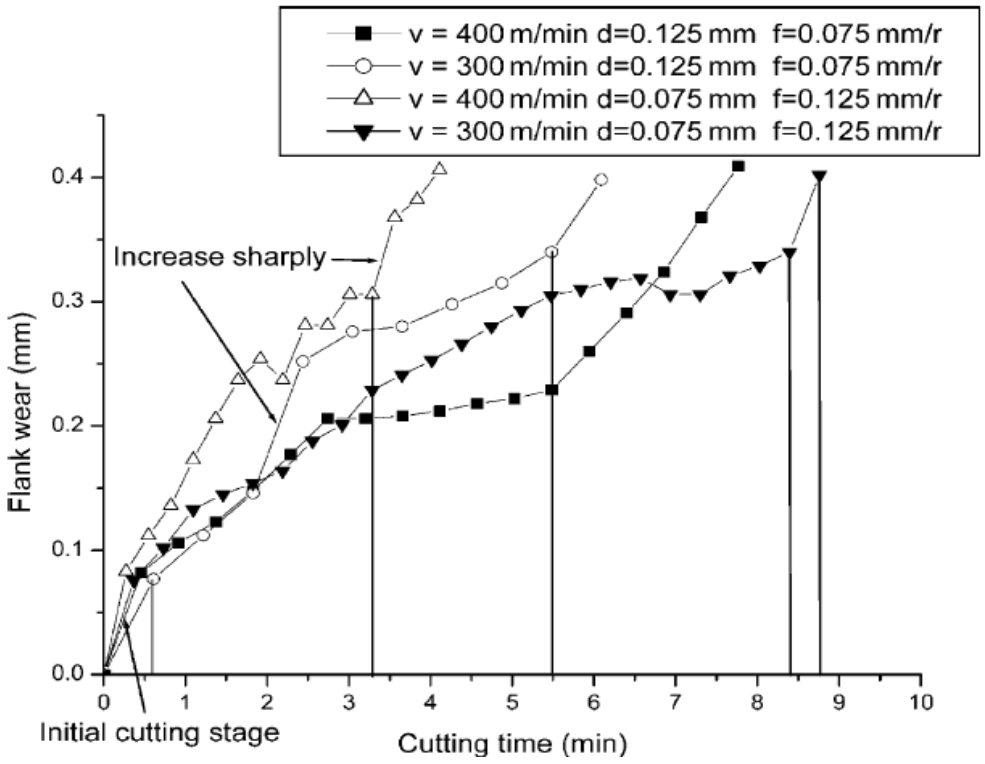

Figure 2.8 - The tool wear evolution in different working conditions [5].

For improved the tool life, conventional tool materials such as HSS and WC were also used in the processes but with different cooling methods. Bermingham tested the tool performance of WC in cryogenic machining Ti6Al4V. According to his analysis, the new cryogenic cooling method successfully extended the tool life of WC by up to 58 % when compared with that of dry machining process. In this study, the dominant tool wear mechanisms were found to be diffusion and adhesion [53]. In 2006 Su et al. investigated compressed cold nitrogen gas and oil mist cooling in high speed end milling of Ti6Al4V. They found an increase in tool life of 2.7 times when compared with an increase of 1.9 for a normal coolant system at 400m/min cutting speed.

There are dynamic stresses acting on the tool caused by formation of serrated teeth over the entire cutting speed range [54][55] and the high chemical reactivity of Ti6Al4V, especially at cutting temperatures in excess of 500 ^{o}C, causes high diffusion wear rate. At temperatures above 500 ^{o}C titanium has strong affinity to adhere, this property of titanium alloys leads to seizing of chips onto the cutting tool surface causing a built up edge which results in rapid tool failure [56]. The combined effect of high yield stress and low Young's modulus allows titanium alloys only small plastic deformations and encourages deflections, chatter and work piece movement away from tool [57]. All these factors lead to rapid cratering and plastic deformation of the cutting tool causing tool failure which is why Ti6Al4V is classified as a difficult to machine material [58].

2.5.2 PCD tool wear in different processes

Compared to other tool materials, PCD has a particularly high thermal conductivity of up to 560 W/mK and a very high hardness of above 50 GPa. Therefore, this material has been applied in machining Ti6Al4V with different processes for the past decade. Amin et al. [5] investigated the effectiveness of PCD inserts in the process of endmilling Ti6Al4V. He reported that the PCD inserts have better performance than WC inserts by considering the metal removal rate over the complete tool life. The major tool wear mechanisms in the case of PCD inserts were found to be diffusion, attrition and notching.

In another investigation of PCD tool performance [14], the maximum tool life of PCD reached 381 mins when the cutting speed was 110 m/min, feed was 0.135 mm/tooth, axial cutting depth was 0.2 mm and radial cutting depth was 5 mm. However, by using the PCD material within the cutting speed range of 175 m/min to 250 m/min, the maximum tool life reached 115.5 mins when high pressure coolant was applied in the process [59]. And the tool wear criterion refers to the ISO Standard 3685 [60].

2.5.3 Limitation of current research in PCD tool wear

Due to the excellent mechanical properties of PCD, it is reasonable to apply this material in the process of machining Ti6Al4V. According to recent research outcomes, there are few research works presenting the tool wear evolution of PCD in endmilling Ti6Al4V. Besides, the new cooling methods have not been applied widely in the industry neither have they been researched to any significant extent for this application. Therefore a study of PCD tool performance in the conventional endmilling Ti6Al4V process is necessary. Finally, the causes of PCD tool wear are barely mentioned in the existing research works.

2.6 Surface quality and chip morphology

2.6.1 Surface roughness

Surface roughness, which is measurement associated with the quality of the finished surface, is one of the most important parameters which can be used as a metric representing the machinability of Ti6Al4V. Different working conditions may cause the changes to the surface integrity which includes surface roughness. For example, Cai et al. [61] showed that Minimum Quantity Lubrication achieves the best lubrication effect and the longest tool life with reduced surface roughness.

As mentioned in section 2.1.1 above, PCD has superior characteristics which includes the very high hardness, toughness and wear resistance and thermal conductivity (which is five times that of copper). It has a relatively high melting point, [62] making it suitable for machining titanium alloys. By studying the process of milling Ti6Al4V with a PCD tool, Li et al. [63] found that the surface quality of the result was sensitive to variation in the cutting speed. This study also found a 5-20 % hardening of the finished surface. Based on the analysis of tool life, surface roughness, cutting forces and the wear mechanisms, Gert et al. [12] found that a decrease in feed and an increase in speed when using a PCD tool produced better surface finish and tool life and outperformed tungsten carbide tools at various cutting speeds. According to Ezugwu's analysis [13], the roughness of the finished surface was below 1.6 μm RA when the cutting speed was set between 175 m/min and 250 m/min, the feed was 0.15 mm/rev and axial cutting depth was 0.5 mm. Again hardening of the machined surface was found in the experiment. Although PCD tool material is highly reactive with titanium alloys, the chemical reaction forms a layer of Titanium carbide which protects the tool by forming barrier to further diffusion. Honghua et al. [64] found that roughness, micro hardness and the microstructure of the machined surface were better with PCD than the surfaces machined with other tool materials.

2.6.2 Chip morphology

The serrated chip is one of the important thermal characteristics in milling Ti6Al4V. The serration is known to be the result of adiabatic shearing (ABS). According to Puerta et al. [65], ABS always occurs in the zone which experiences a high strain rate. Sima and Ozel found that the ABS bands could be observed clearly when the cutting speed was higher than 60 m/min with the feed above 0.05 mm/rev [66]. When these machining parameters were large enough to cause obvious chip serration, the chip serration frequency was sensitive to the machining parameters, geometrical effect, the thermal properties of the cutting tool and of the workpiece and the cooling efficiency.

In the process of machining Ti6Al4V, Gert et al. [12] mentioned that at high cutting speeds the properties of titanium alloy Ti6Al4V causes complex wear mechanisms on the cutting tool because of the titanium alloy's low thermal conductivity of 7W/mK which is 86% lower than that of AISI 1045 steel. The heat affected zone in titanium machining is very small because of its high strength maintaining property at elevated temperatures and also its ability to form localised shear bands during the machining process. It forms very short chip-tool contact length of about one-third of the contact length for steel [67]. This concentrates the heat giving rise to a temperature of about 700 ^{o}C at the cutting edge [5].

The serration frequency of the chips is one of the important characteristics for localized shearing effect. This parameter normally indicates the shearing speed and local geometry of shearing bands. According to the analysis conducted by Molinari et al. [68], the chip serration frequency was proportional to the cutting speed. Migu ́ez studied the chip serration by using FEM models [69]. Their results show that the geometrical parameters and friction are important to the chip morphology. Furthermore, Baker has also found that a lower thermal conductivity could cause a higher serration frequency [70]. PCD has a higher thermal conductivity than conventional tool materials. In the process of milling Ti6Al4V, it is important to understand how this difference will affect the shape of the chips. Little research into the serration frequency in milling Titanium alloy with PCD tools has been conducted to date.

2.6.3 Limitation of current research in surface quality

For the alloy Ti6Al4V, the influence of machining parameters on surface roughness has been studied by many researchers in the machining of Ti6Al4V. However, the study of the machining parameters' influence on surface roughness is insufficient. For example, the influence of feed has been barely investigated. In addition, the serration frequency of the chips is relevant to the thermal mechanics of the process and this is not completely covered in the literature. The analysis of chip serration frequency would be a useful supplement to a tool performance study.

2.7 Summary

Although plenty of research has been performed in the area of machining Titanium with PCD tools, most of the research is focused on the turning process or the milling process with big cutting tools (more than 10 mm in diameter). So far little research has been conducted in the application of small milling tools. This thesis investigates the performance of PCD milling tools in milling of titanium alloys (Ti6Al4V) by using customized cutting tools of 6 mm in diameter. The objectives and experimental methods are presented as follow:

- To study the discharging characteristics of PCD. The PCD materials will be tested in the new developed Electrical Discharge Grinding (EDG) system. The voltage and current will be directly monitored through the designed circuit.

- To study the relationship between cutting parameters and cutting force. The experimental data will be collected through the Kistler dynamometer associated with National Instrument system in the cutting tests. A new cutting force model with the consideration of the influences of changing cutting speed, feed and axial cutting depth will be developed. The

new cutting force model will be validated through a series of cutting tests.

- To study the thermal characteristics of endmilling Ti6Al4V with PCD tools. By applying X-ray diffraction on failed tools the chemical components will be investigated. The cutting temperature in end milling will be monitored through the infrared camera. The new cutting temperature model will be developed by considering the influences of machining parameters. The highest cutting temperature on tool nose can be induced through the analysis of chemical components on PCD tools

- To study the tool wear of PCD mills. The surface of PCD tools will be examined by using a Philips XL 30 Scanning Electrical Microscope (SEM). Causes leading to tool failure will be discussed and simulated by using Finite Element Analysis (FEA) models.

- To study the quality of Ti6Al4V finished surface and chip morphology. The examination of finished surface will be performed with the Alicona optical microscope and chip morphology will be investigated based on the SEM scanning photos of used tools.

3 Electrical discharge characteristics of PCD

The electrical discharge characteristics of tool materials are important to determine the machining parameters. They include the discharge waveforms of voltage and current, the gap voltage, peak current and electrical dynamic resistance of the material. This study aims to investigate the influence of peak current on the discharge waveforms and obtain the relationship curve of gap voltage, and electrical resistance of PCD.

3.1 Introduction

3.1.1 Introduction to the EDM process

Electrical Discharge Machining (EDM) is a well-established non-contact machining method for the manufacturing of geometrically complex components and the shaping of hard-to-machine materials. It turns electrical power into thermal energy through a series of discrete electrical discharges occurring between an electrode and the workpiece. The thermal energy generates a channel of plasma between the two poles at temperature of up to 20,000 ^{o}C [71]. The high concentration of heat melts and evaporates the material from the surface of the workpiece. A material removal rate (MRR) of 2 - 400 mm^3/min can be achieved depending on applications [72, 73]. EDM can produce cavities with thin walls and fine features; can machine material with high hardness [74].

3.1.2 Principle of the EDM process

Figure 3.1 illustrates the principle of the EDM process. The part of the EDM system at which discharge occurs is similar to capacitor, the machining electrode and workpiece form the two plates. The gap between machining electrode and workpiece is filled with dialectical liquid (oil or water). The electrical field intensity near the negative plate increases quickly when an electrical pulse is generated by the EDM generator. When the electrical potential exceeds a critical value breakdown begins and, electrons will move to the positive electrode and a discharge plasma channel will be formed in a short time. Then, the gathered electrical energy goes through this channel in the form of current. Finally, the material will be removed from not only machining electrode, but also from the workpiece. Generally, the process of EDM can be described in following steps:

Step 1: The beginning of the electrical pulse.

Step 2: The electrical field intensity increases being highest at the point where the gap is shortest.

Step 3: When the electrical field intensity is great enough, the discharge channel is formed.

Step 4: The current goes through the discharge channel (spark appears) and local material is melted or evaporated.

Step 5: The electrical pulse stops and the associated bubble in the dielectrical implodes.

Step 6: The removed material is flushed by dielectrical liquid.

For the EDM process, the waveforms of voltage and current are important to the surface finish result. The general form for the voltage pulse is shown in Figure 3.2. The “On Time” represents the duration of the generator providing energy and the “Off Time” is the duration without energy supply. According to McGeough et al. [74], in practical application the voltage and current waveforms of EDM are similar to that shown in Figure 3.3. The value of breakdown voltage is determined by the electrical properties of dielectrical fluid, the electrode and workpiece. The ignition delay time is an important factor which can reflect the isolation conditions between the electrode and workpiece. A larger gap between electrode and workpiece will lead to a longer ignition delay time. According to Altpeter and Perez [75], monitoring the ignition delay time makes it possible to infer the gap width. However, the ignition delay time is considered constant when the same working conditions are applied in an experiment or process. For example, Chung et al. [76] assumed this value to be constant through the experiment.

There are four electrical pulses distinguishable for the EDM process: open gap voltages, short circuit, arcs and sparking. And the waveforms of these four cases are shown in Figure 3.4.

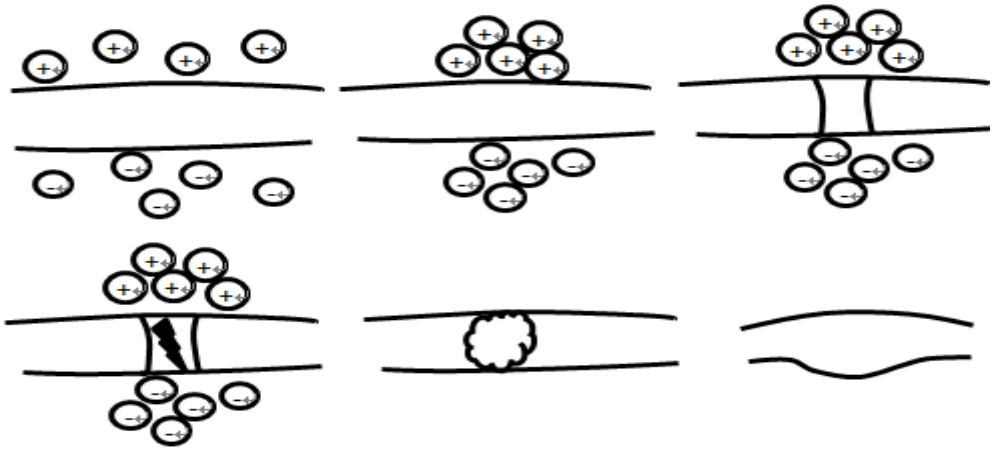

Figure 3.1 - Illustration of EDM principle.

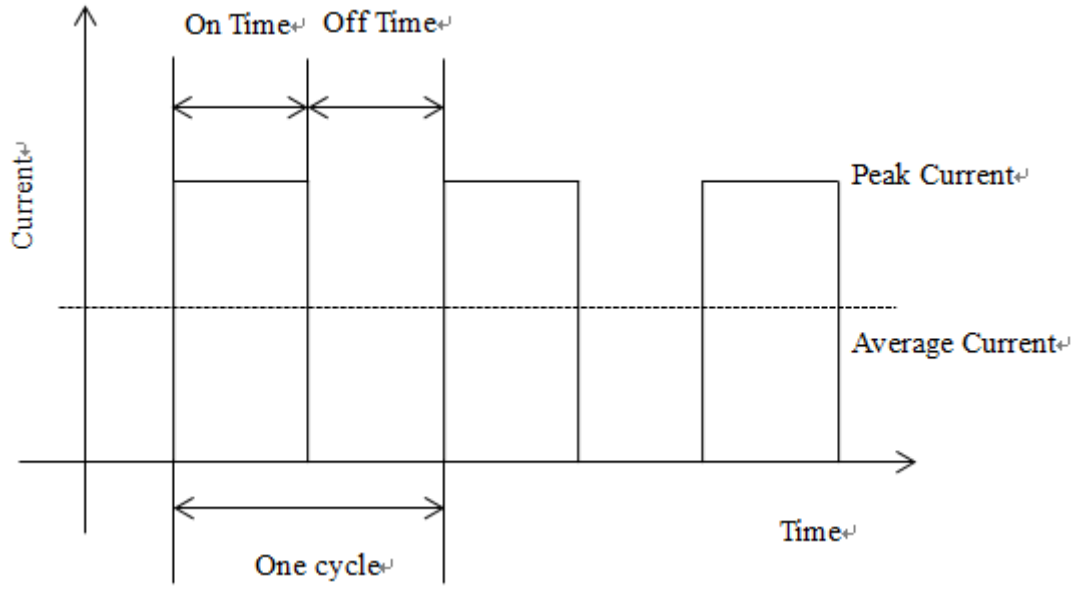

Figure 3.2 - The EDM current pulse provided by generator [74].

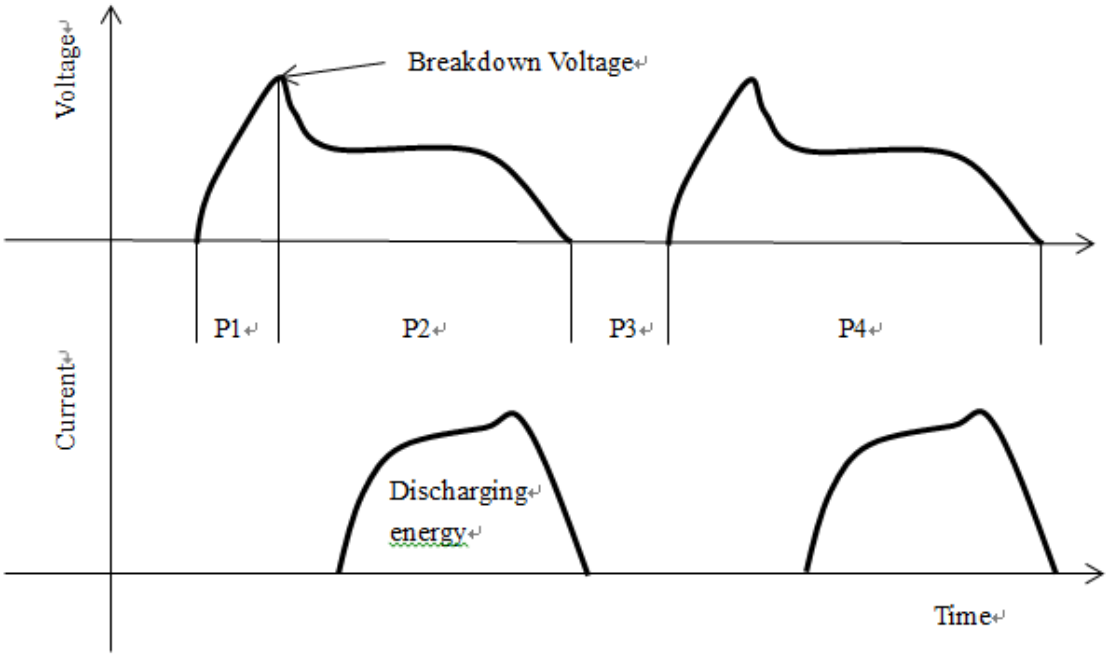

P1: Ignition delay time; P2: Discharging duration; P3: Off Time; P4: On Time.

Figure 3.3 - The practical discharge waveforms of voltage and current [74].

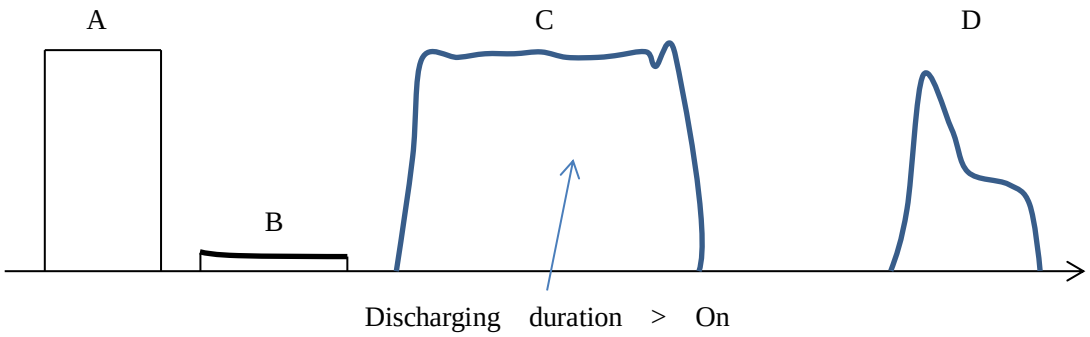

A: Open gap voltage; B: Short circuit; C: Arcing; D: sparking.

Figure 3.4 - Four electrical pulses of EDM [74].

The EDM process can be classified by applications; there are two main types of EDM in the industry: Sinker EDM and Wire EDM. Sinker EDM can also be called cavity type EDM or volume EDM. The electrode and workpiece are set into the working environment which fills with oil or dielectrical liquid as shown in the illustration of Figure 3.5 (a). The electrode used in the Sinker EDM process can be graphite or copper and it is shaped based on the process requirement. However, the Wire EDM process (Figure 3.5 (b)) uses a continuous metal wire as the electrode. The cutting angle in the Wire EDM process is very small due to the use of small-sized diameter wires. Generally, according to Hassan, the polarity used in the EDM process follows the suggestions given in Table 3.1. Moreover, according to Elman [77], the properties of the dielectrical fluid which need to be considered are the viscosity, stability and cooling performance. Silicon fluids and the fluid based on petroleum oils have shown extremely good results in the past studies.

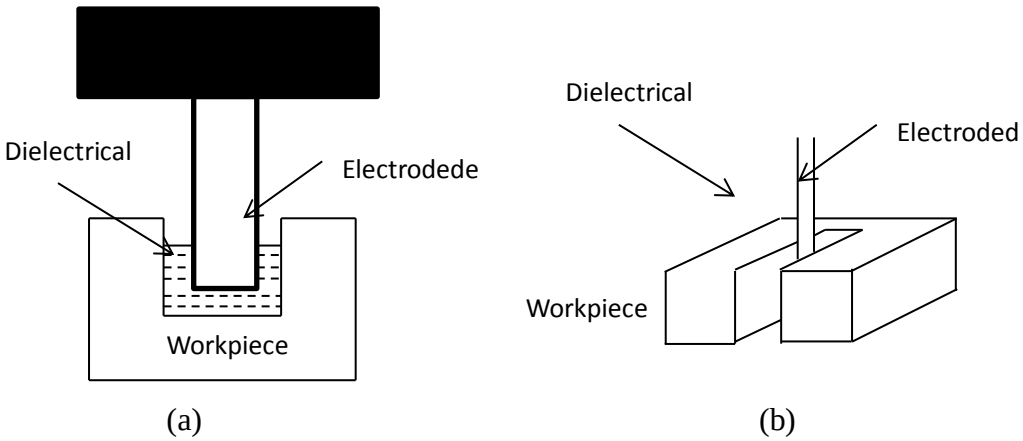

Figure 3.5 - The two types of EDM applications: (a) Sinker EDM; (b) Wire EDM.

Table 3.1 Electrode polarities for different workpiece materials [74]

	Workpiece				
Electrode Material	*Steel*	Tungsten Carbide	Copper	Aluminum	Ni-base alloy
Graphite	+,-	-	-	+	+,-
Copper	+	+,-	-	+	+
Cu-W	+	+,-	-	+	+
Steel	+,-	+	-	-	-
Brass	-	-		+	-

3.1.3 PCD properties

The super-high hardness and excellent wear resistance properties of Polycrystalline Diamond (PCD) have led to the wide application of PCD tools in woodworking and aerospace industries for the machining of hard wood, composite material and Titanium alloys [78, 79]. PCD discs are produced by sintering together graded and selected diamond particles with binding materials at temperatures of up to 2,000 oC and pressures of 5 - 7 GPa [80]. The grain size of diamond particles is in the range of 1 - 50 μm. The thickness of the PCD layer is in the range of 0.3 - 1 mm. The PCD is supported on a substrate of cemented carbide of 0.3-5 mm in thickness. The binding material is usually cobalt, which is electrically conductive making the PCD also electrically conductive. The bulk electrical resistivity is not constant; it varies with the percentage of binder and the grain size of diamond particles. Currently the diameter of commercial PCD blanks is up to 72 mm.

Figure 3.6 - PCD blanks and chips cut by W-EDM.

3.1.4 Machining PCD with EDM process

The cutting process of PCD compacts is usually done by laser or Wire-Electrical Discharge Machining (W-EDM) (Figure 3.6). However, since diamond is one of the hardest materials in the world, the grinding and shaping processes are extremely difficult.

Since PCD is electrically conductive, it is possible to grind PCD tools using EDM technology [81, 82]. Various researches in the Electrical Discharging Grinding (EDG) of PCD have been performed in the past decades [83]. Thoe et al. [84] examined the edge quality of various grades of PCD cutting tool blanks produced using an in-house EDG machine. The pulse generator had a maximum current of 30A, was programmable with a resolution of 1A, had a maximum open circuit voltage of 150V, an Time-on/Time-off range of 1 - 100 μs, and a minimum usable on-time of 6 μs. Olsen et al. [85] studied the effects of operating parameters on sparked surface/edge quality and efficiency by using a commercial EDG machine. Taguchi experiments were used to find the optimized parameters. The voltage applied in their tests was in the range of W×102 - 1.7W×102, the current was X×10 - 1.5X×10, the On-Time was Y - 2.0Y and Off-time Z×10 - 2.0Z×10, where the values of W, X, Y and Z are unfortunately unavailable in the paper.

Electrical discharge machining is a complex physical process. As PCD is a relatively low bulk conductivity material, the discharge characteristics of PCD are different from conventional materials such as carbide and High Speed Steel (HSS) [86]. Theoretically high voltage, smaller current and high frequency (short On-Time) should be applied to achieve better surface quality. In practice the values of these parameters should be determined based the discharge characteristics of the PCD workpiece. This is particularly important in the tool manufacturing industry. Unfortunately little research has been done in this field and no detailed information is available in the public domain.

3.2 Experimental setup and procedure

3.2.1 Experimental setup

In order to demonstrate the discrete nature of the arc discharge occurring in the process, an appropriate experimental instrumentation setup was used to capture the time dependence of voltage and current. The experimental setup is shown in Figure 3.7.

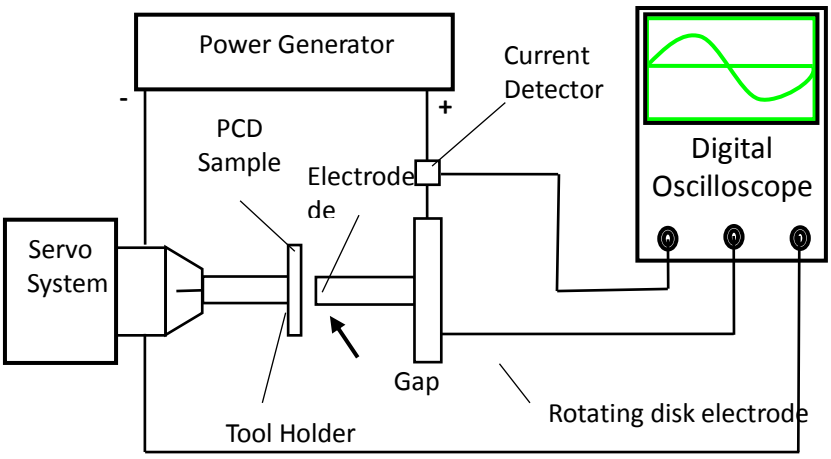

Figure 3.7 - Experimental setup and instrumentation.

The experiment was carried out on a new EDG machine equipped with a rotating disk electrode made of copper. The electrode was a copper bar (3 mm in diameter) installed in the axial direction of the grinding wheel. The test sample was brazed on the end face of a Tungsten carbide holder, which was clamped by the headstock spindle of the machine. The linear gap distance is adjustable in Z direction through the servo system. The EDM power supply is an in-house designed power generator which is able to generate short pulses with a minimum On-Time of 1 μs. The output voltage is in the range of 90 - 260V. The current is in the range of 1 - 20A. The discharge current was measured by using Tektronix TCP305 probe coupled with a Tektronix TCPA300 amplifier. Signals were record and exported to EXCEL spread sheet through a digital oscilloscope (Tektronix 2024B).

The grain size and percentage of metal phases in PCD inserts is believed to have influence on the machinability. Therefore, two different grain sizes of PCD samples made by Element Six (CTM302 and CMX850) were randomly chosen for this experiment. Detailed information of the two materials is shown in Table 3.2.

Table 3.2 Physical parameters of CTM302 and CMX850

Sample Number	Typs	Particle size (μm)	Diameter (mm)	Thickness of PCD (mm)	Thickness of substrate (mm)
1	CMX850-	0.5-1	20	0.5	1
2	CTM302-	2-30	20	0.7	3

3.2.2 Experimental Procedure

To analyze the relationship between gap voltage, gap distance, current, resistance and the

physical characteristics of PCD materials such as grain size and binding materials, a total of nine groups of experiments were conducted by applying parameters shown in Table 3.3. The power supply is able to generate both iso-frequency and iso-energy pulses. However, iso-energy model was applied because the mapping relationship between parameters is more straightforward under this working model.

Both normal and abnormal sparks have been recorded. In order to compare the discharge characteristic of PCD with that in ordinary EDM processes, experiments on Tungsten carbide samples were carried out before tests on PCD samples. The electrical parameters applied in the carbide and PCD tests are shown in Table 3.3.

3.3 Results and Discussion

3.3.1 Difference in waveforms caused by variation of materials

For this test, there was a not coated sample used. Discharge waveforms of carbide, CMX850 and CTM302 under the same machining condition are shown in Figure 3.8, 3.9 and 3.10. The yellow curves represent the signals of voltages and the blue curves are the signal of currents. It can be seen from the figures that the discharge waveforms of PCD are similar to that of Tungsten carbide. At the point of ionization, the sparking gap voltage is reduced to the machining voltage. The flow of current was begun at the ionization point and it continued for the complete On-time. The gap voltage is U_e and peak current is i_p.

Table 3.3 Experimental parameters

Materials	Experimental parameters			Test Number
	Open voltage (V)	Peak current (A)	Pulse width (μs)	
Tungsten carbide	120	1	40	B0001
CMX850	120	1	40	A0013
	160	1	40	A0001
	160	5	40	A0003
	160	10	40	A0004
CTM302	120	1	40	A0019
	160	1	40	A0027
	160	5	40	A0028
	160	10	40	A0029

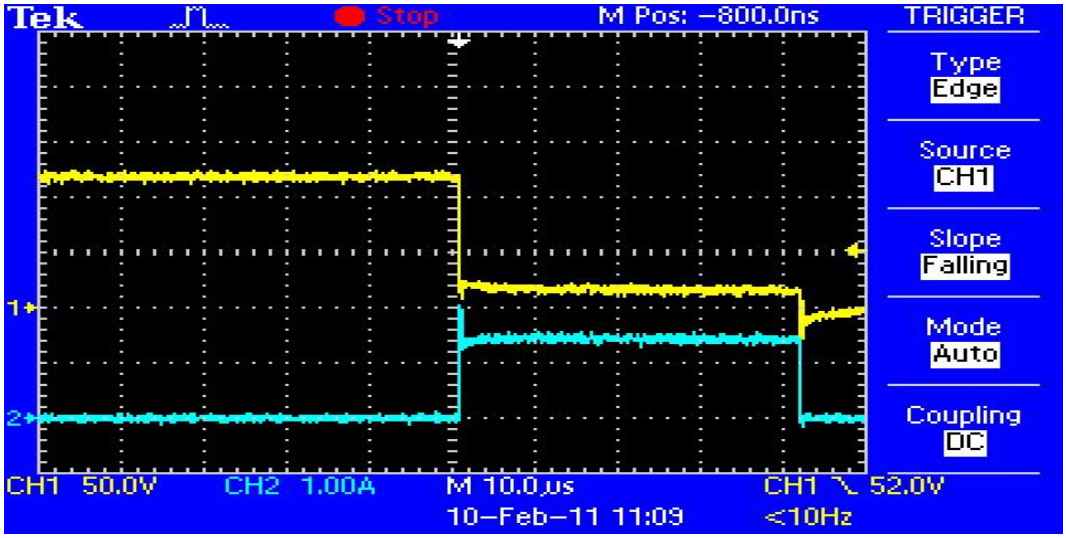

Figure 3.8 - B0001 discharging waveform.

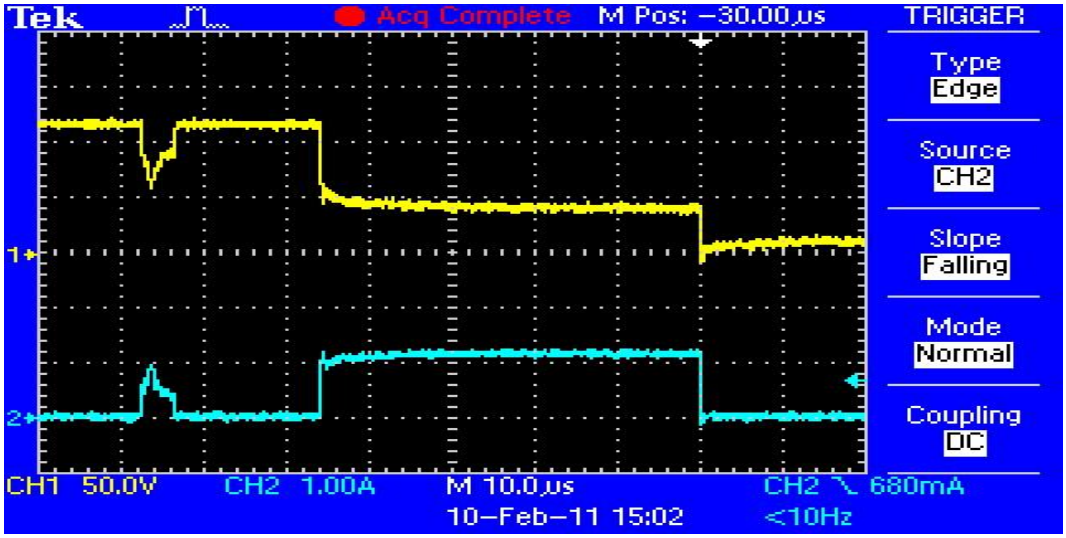

Figure 3.9 - A0013 discharging waveform.

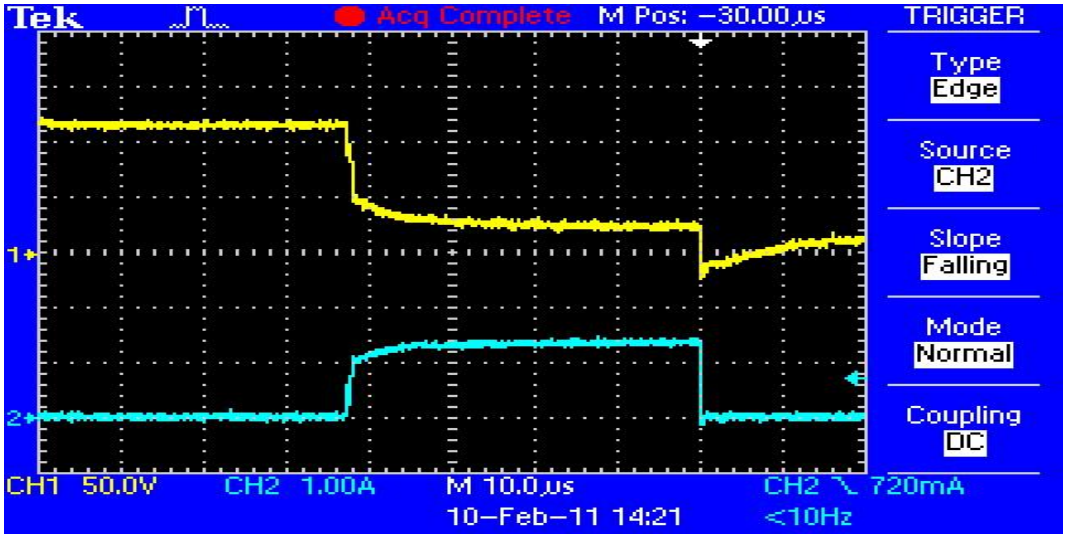

Figure 3.10 - A0019 discharging waveform.

To quantify the difference between the discharge waveforms, the voltage and current data recorded within the first 40 μs since the ionization was analyzed. Both the voltage and current were averaged at an interval of 5 μs in order to minimize the effect which could be caused by measurement error. The average results are shown in Table 3.4. The variances of voltage and current with time are drawn in Figure 3.11 and 3.12. It can be seen from the table and figures that the lowest gap voltage occurred in the machining of Tungsten carbide, which was 15.7V; the highest U_e occurred in the machining of CMX 850, which was 42.5V; while the maintaining voltage of CTM302 was 26V, which was in between carbide and CMX850.

Table 3.4 the average values of different materials in every 5μs

Materials	Record Number		0-5μs	5-10μs	10-15μs	15-20μs	20-25μs	25-30μs	30-35μs	35-40μs
Tungsten carbide	B0001	U	20. 2	17. 2	16. 5	16. 4	16. 1	15. 7	15. 8	15. 6
		I	1. 41	1. 45	1. 44	1. 45	1. 43	1. 43	1. 42	1. 42
CTM302	A0013	U	50. 2	33. 8	30. 1	28. 1	27. 0	26. 0	26. 0	26. 0
		I	1. 05	1. 29	1. 31	1. 33	1. 35	1. 36	1. 36	1. 36
CMX850	A0019	U	51. 6	46. 3	44. 6	43. 5	42. 6	42. 7	42. 3	42. 3
		I	1. 05	1. 12	1. 16	1. 17	1. 17	1. 16	1. 17	1. 16

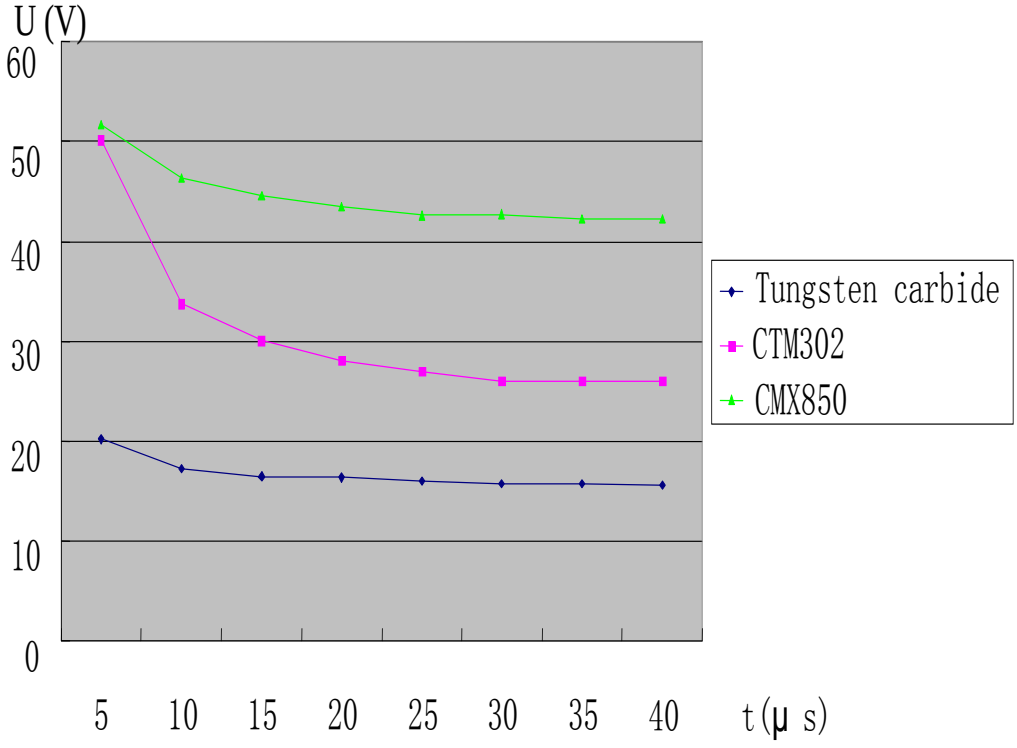

Figure 3.11 - Voltage curves of different materials.

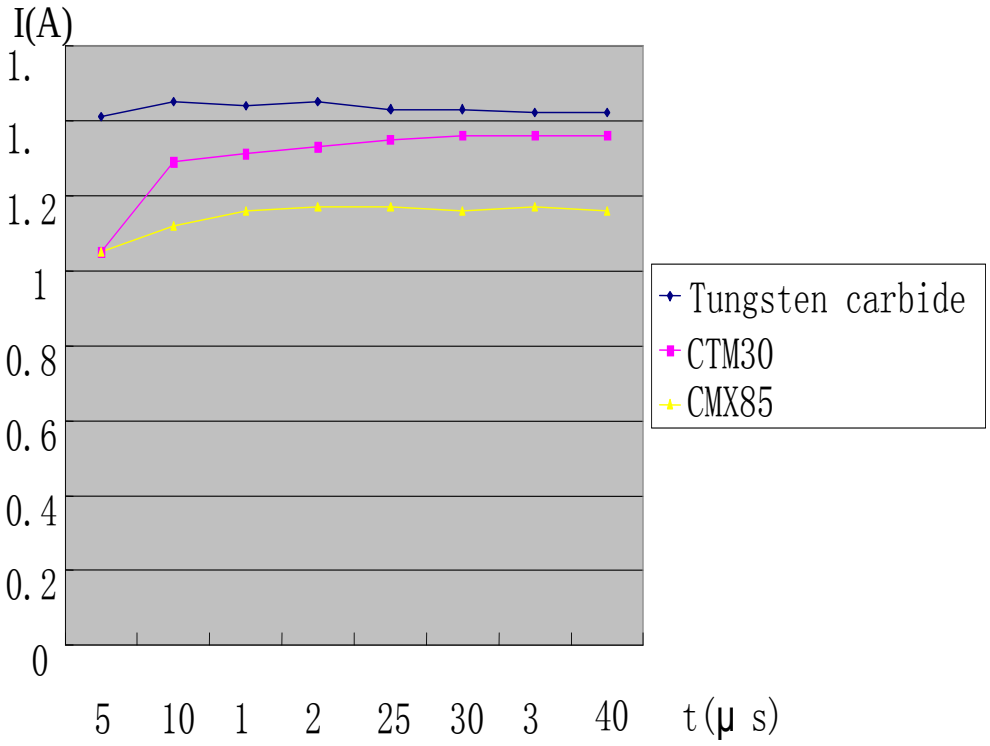

Figure 3.12 - Current curves of different materials.

This phenomenon can be explained by analyzing the electrical resistance of these materials:

In an EDM process the maintaining voltage is equal to the sum of the voltage across the discharging channel (U_g) and the voltage across the workpiece (U_r) caused by the resistance of the material, as shown in Figure 3.13. Value of U_g depends on the workpiece material, property of dielectrical and the value of gap distance. U_r is the product of workpiece resistance and discharging current. U_e can be expressed as Equation (3-1)

$$U_e=U_g+i_p \times R_c \qquad (3\text{-}1)$$

Where R_c is the value of workpiece resistance.

Because the resistance of Tungsten carbide is very small, U_r can be neglected. Therefore, in the machining of Tungsten carbide, U_e is equal to U_g.

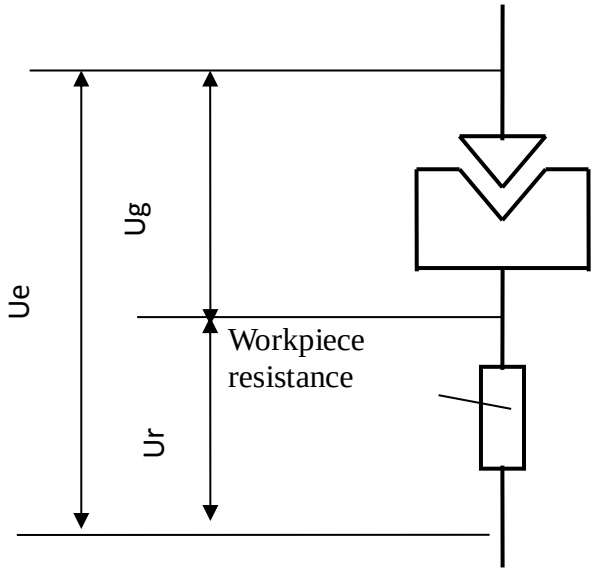

Figure 3.13 - Equivalent circuit in the machining of PCD.

PCD is a low conductivity material which is composed of a large portion of diamond particles which are electrically non-conductive. The electrical resistance of PCD is larger than Tungsten carbide. Therefore, even if the U_g of PCD was the same as in the machining of carbide, according to Equation (3-1), U_e of PCD is always higher than the U_e of carbide.

3.3.2 The influence of discharge current

Experiments with different electrical current were conducted to analyze the influence of resistance of PCD workpiece. The average voltage in the first 30 or 35 μs from ionization is taken as the maintaining voltage. Table 3.5 shows the maintaining voltage and the corresponding current, Figure 3.15 illustrates the relationship between maintaining voltage and spark current. It can be seen in Figure 3.15 that the maintaining voltage increases linearly with the increase in electrical current. This is in line with the previous analysis.

By substituting the start and end points of the curve in Figure 3.14 into Equation (3-1), U_g and R_c of CMX302 can thus be obtained:

$$U_g=24.9V;\ R_c=0.31\Omega$$

U_g and R_c of CMX850 are found to be:

$$U_g=39.5V;\ R_c=0.59\Omega$$

Therefore, the maintaining voltage of CMX850 (U_e1) and CTM302 (U_e2) can be described as Equation (3-2) and (3-3)

$$U_e1=24.9+0.31\times i_p \quad (3\text{-}2)$$

$$U_e2=39.5+0.59\times i_p \quad (3\text{-}3)$$

Based on above calculation, the resistance of CTM302 (0.59Ω) is found to be bigger than the resistance of CMX850 which is 0.31Ω. This is because the thickness of CTM302 (0.7mm) is bigger than CMX850 (0.5mm) although the resistivity of CMX850 is smaller than CTM302.

Table 3.5 Values of maintaining voltage and discharging current

Sample 1	Discharging current（A）	1．82	5．428	13．36
	maintaining voltage （V）	25．5	26．74	29．07
Sample 2	Discharging current（A）	1.635	4.797	11.75
	maintaining voltage （V）	40.48	44.02	46.4

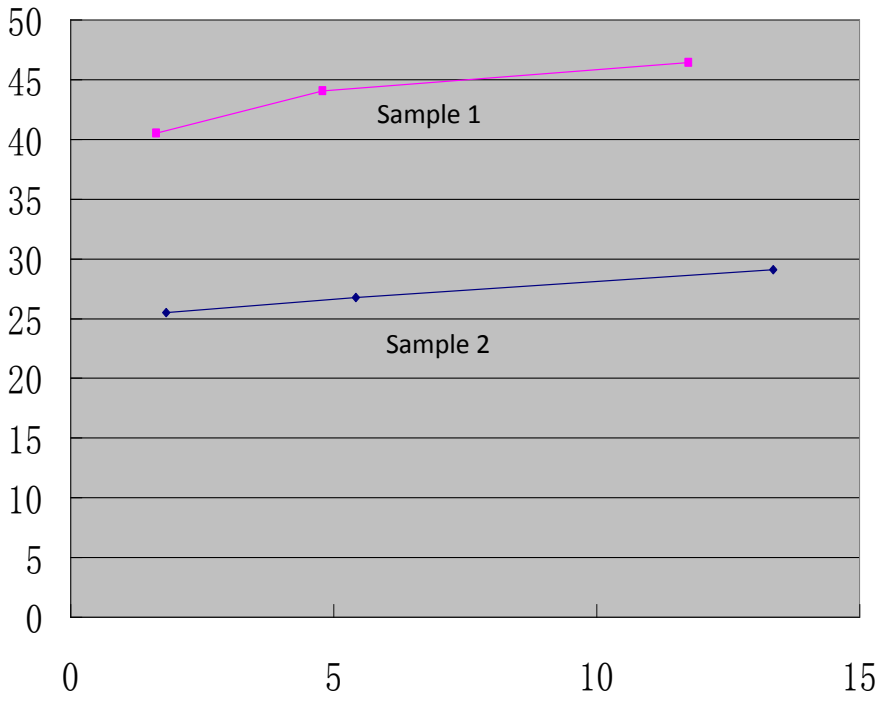

Figure 3.14 - Relationship between maintaining voltage and discharging current.

3.3.3 The impact of gap distance

Short-circuit is an abnormal working condition in EDM machining when the gap distance is

reduced to zero. Once the electrode contacts the workpiece in the feeding process, the maintaining voltage drops to zero instantaneously; in the meantime, there is a significant increase in current between the two poles. Usually the control system is able to detect this abnormal arcing and will retract the electrode to eliminate the possible damage that may be caused to the workpiece surface. The system will resume feeding once the short circuit is eliminated.

In the experiment with PCD samples, a controversial phenomenon which is totally different from Tungsten carbide was found: When the electrode contacted the surface of PCD workpiece (gap distance became zero), a normal discharging waveform rather than the waveform of short circuit was captured (Figure 3.15). The experiments were repeated for five times to eliminate the possibility of measurement errors or miss-operations. The non-short-circuit sparking appeared 3 times in the 5 experiments. It can be concluded that this was not a random phenomenon. On the contrary, it was the unique electrical discharge characteristic of PCD.

Actually this special characteristic complies very well with the physical structure of PCD, and the phenomenon can be reasonably explained based on the physical construction.

The structure of PCD is shown in Figure 3.16. Nonconductive diamond particles are bound with conductive metal particles such as cobalt. The conductivity of PCD relies on the conductive network formed by the binding metals. When the electrode contacted the PCD workpiece in the experiment, it was very possible that it touched only the diamond particles protruding from the binder. This protrusion prevented the contact of electrode with the conductive binder. Thus, it prevented the short circuit. When the high voltage was applied between the electrode and the workpiece, the normal sparking was observed between the electrode and the binder. By chance, what contacted the electrode may also be the binder which protrudes from the PCD sample. In this case, short-circuit were observed as expected.

Therefore, it may not necessarily lead to short-circuit in EDM machining of PCD materials when the electrode contacts workpiece surface or when the gap distance is zero. It is very possible for normal sparking to occur. However, due to the random protrusions of diamond and binder particles in PCD, the phenomenon is unpredictable.

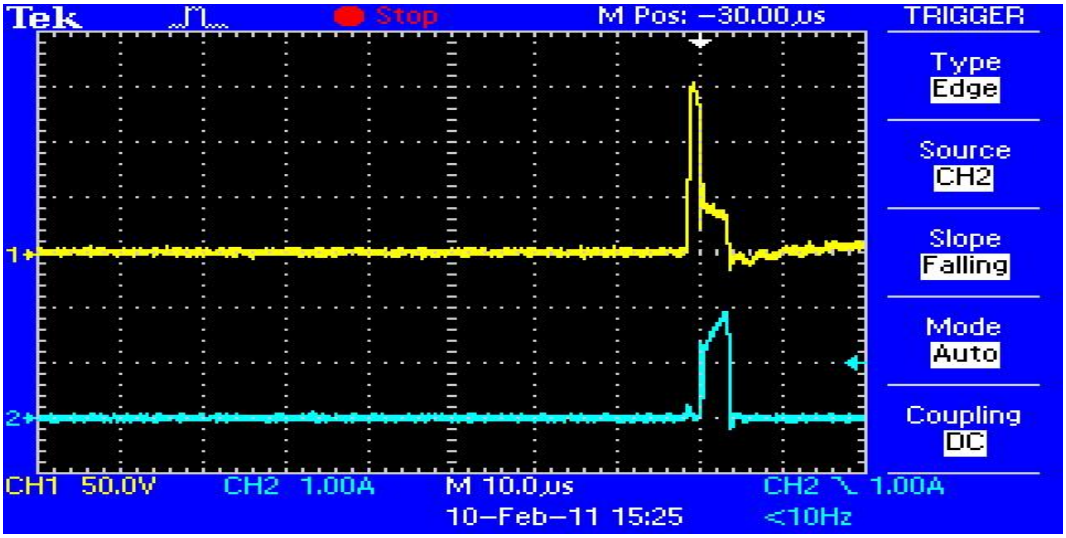

Figure 3.15 - Discharge waveform of zero gap distance.

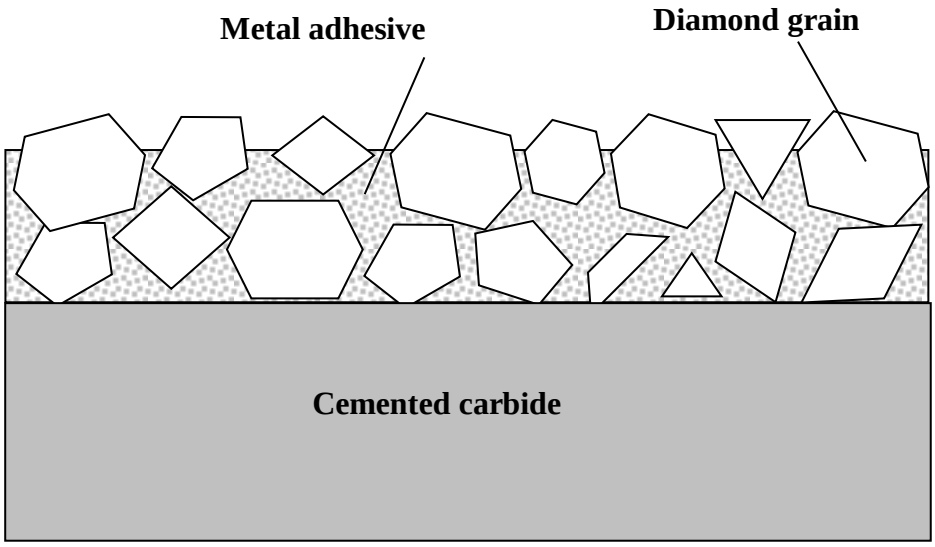

Figure 3.16 - Structure of PCD.

3.4 Summary

This chapter has introduced experimental electrical discharge characteristics. The relationship between gap voltage, peak current and electrical resistance of various PCD materials has been presented. From the experiments, the following results are found:

1. Discharge waveforms in machining PCD are similar to that found when machining ordinary materials such as Tungsten carbide.

2. The maintaining voltage in machining PCD is higher than that of conventional EDM machining of ordinary materials. The difference in the maintaining voltage varies significantly with the variation of PCD materials.

3. The maintaining voltage has the linear relationship with the increase in current.

4. Arcing was not observed throughout the experiment.

These conclusions are very important for the design of EDG machines specifically for machining PCD tools. The method for setting up an initial reference point by using electrode probes and the criterion for detecting scenarios of short-circuit during machining become invalid, and new methodologies are required using the discharge characteristics of PCD.

4 Instantaneous cutting force

This Chapter is aimed at developing a new model for instantaneous cutting force by deducing the mathematical relationship between the cutting forces and machining parameters. The model development is based on the analysis of the cutting coefficient and the relationship between cutting force and machining time. Through investigating the influence of cutting speed, feed and axial cutting depth, new expressions involving cutting coefficients are proposed. The prediction agrees closely with experimental results.

4.1 Introduction

4.1.1 Instantaneous cutting force

According to Groover [87], the instantaneous cutting force is generated by the shearing effect, friction effect and solid deformation in the metalworking process such as milling and turning. The cutting force is an important factor which influences the dynamic phenomena, roughness, tool wear, and so on [38].

4.1.2 Important factors for cutting force

There are many factors directly or indirectly affecting the cutting force values in metalworking processes:

- Mechanical properties of workpiece and tools, which include elastic modulus, plastic modulus, tensile strength, yield strength and compression limit, etc.
- The tool geometry and machining parameters, which include cutting speed, feed, axial cutting depth, radial cutting depth and flooding, etc.
- The processing system issues, which include vibration, chatter and runout effect.

For the turning and milling processes, the basic mechanism of material removal from workpiece is the shearing effect. As shown in Figure 4.1, the tool provides the shearing force with a certain cutting speed which can be predefined before the process. The shearing force leads to elastic deformation and plastic deformation at the beginning and finally causes the material separation. It is acknowledged that the cutting force is the results of the material resisting deformation and fracture. Also, the friction effect during the machining process contributes to the cutting force too. Thus, it is easy to understand that the mechanical attributes of workpiece have a direct effect on the cutting force. This can be seen from Figure 4.2 which shows the relation curve of cutting force coefficients and cutting speed [88]. In this experiment, Ti555.3 and Ti6Al4V were tested

under the same machining conditions. The results indicate that the Ti555.3 which has higher ultimate tensile strength resulted in the higher specific cutting force.

Moreover, the mechanical properties of some metal materials can be significantly affected by strain rate such as Ti6Al4V. According to Lee et al. [89], the stress-strain curve of Ti6Al4V is shown in Figure 4.3. The analysis shows clearly that the stress increase with the strain rate. The working temperature can also influence the mechanical properties of Ti6Al4V.

In a milling process, the cutting speed is normally very high. The reported strain rate for milling is up to 10^4 - 10^5 s^{-1} [90]. When Ti6Al4V deforms at such a high strain rate, it is reasonable to consider the strain rate effect.

In many research works, the cutting force model does not take into account the influence of strain rate, rather they focus on the effect of cutting speed, feed and axial cutting depth. These controllable machining parameters can also have an impact on the strain rate.

In term of the machining system issues, run out effect and chatter are two major aspects which were discussed in many studies. Generally, these two factors always affect the surface finish dramatically.

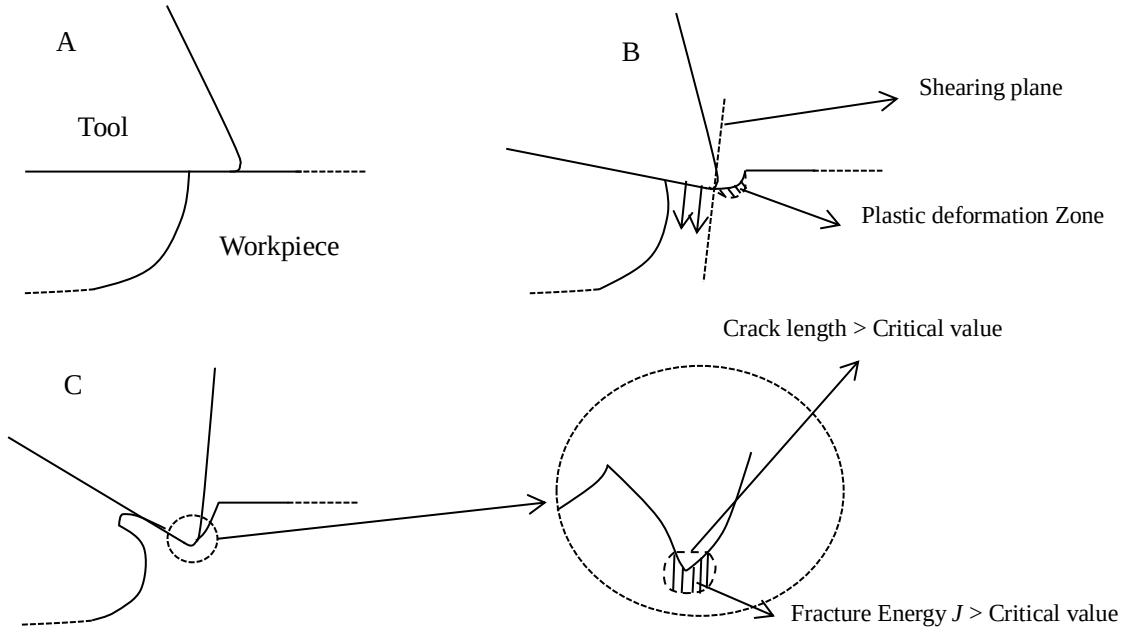

Figure 4.1 - The mechanism of cutting process.

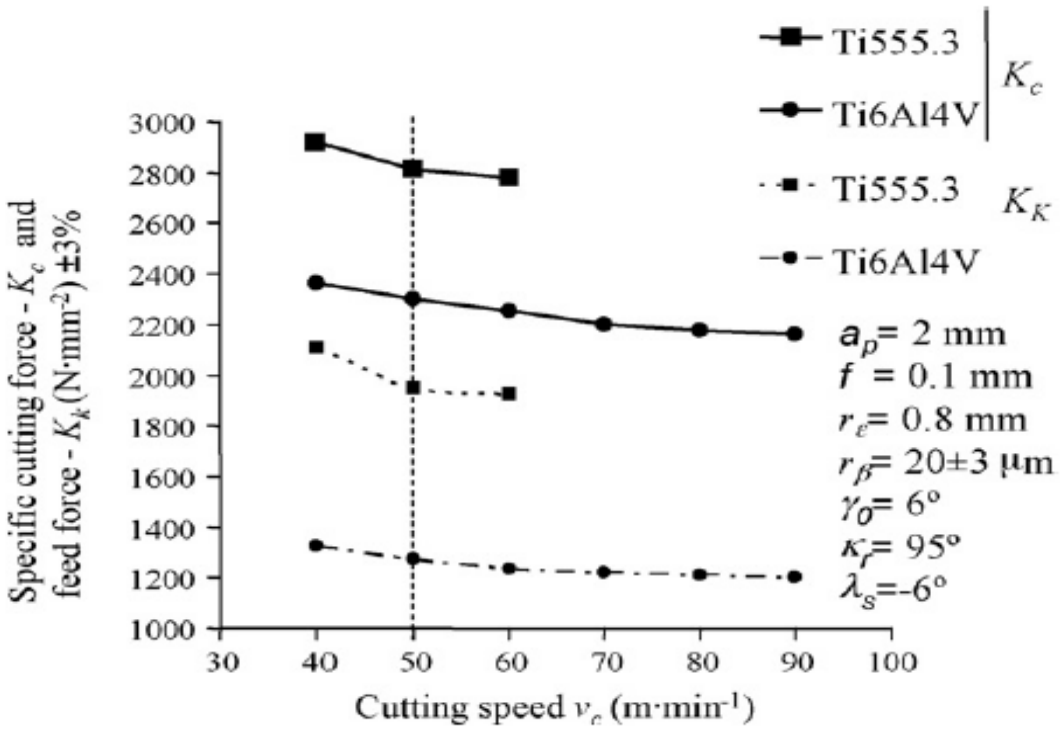

Figure 4.2 - The cutting force coefficients of Ti555.3 and Ti6Al4V with different cutting speed [88].

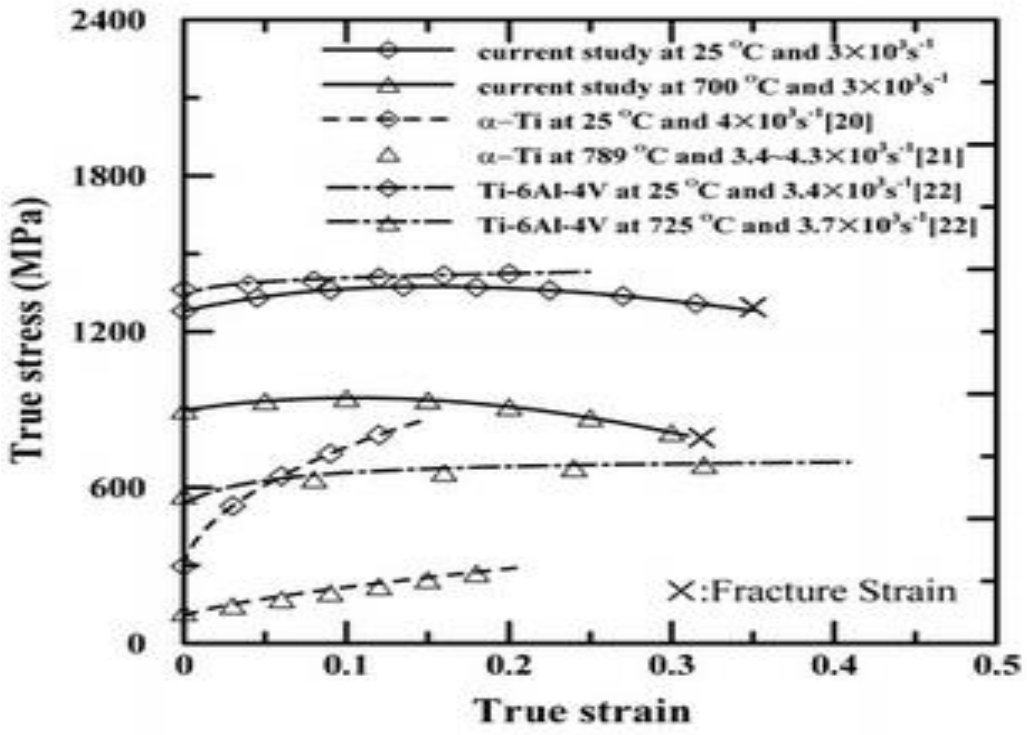

Figure 4.3 - The stress-strain curves of Ti alloy [89].

4.1.3 The basis of an analytical cutting force model

Lamikiz et al. [40] proposed a new analytical model for cutting force used in predicting the cutting force in the process of sculptured surface milling with a ball nose milling tool. The applied tool material was HM K10 t TiAlN and the workpiece materials were AISI H13 52 HRC and Al7075T6. The model was based on Equation (4-1) which was presented by Lee and Altintas [91]:

$$\begin{cases} \mathrm{dF_t} = K_{te} dS + K_{tc} t_n db \\ \mathrm{dF_r} = K_{re} dS + K_{rc} t_n db \\ \mathrm{dF_a} = K_{ae} dS + K_{ac} t_n db \end{cases} \tag{4-1}$$

In this assumption, each local cutting force component is comprises two parts: $K_e dS$ and $K_c t_n db$, where K_{te}, K_{te}, K_{te}, are shear specific coefficients which are equal to K_T, K_R, K_Z, respectively. And K_{tc}, K_{rc}, K_{ac} are edge specific coefficients. Also, t_n, is the undeformed chip thickness which is equal to $h(\varphi)$. S, dS, db are the length of the cutting edge, the differential value of S and length of differential cutting edge perpendicular to cutting direction. By considering the complex tool path and the geometry of the tool nose, Lee and Altintas deduced the integral expression for the cutting edge spline and the expression of theoretical chip thickness.

$$dS = \sqrt{[R'(\varphi)]^2 + R^2(\varphi) + \frac{R_0^2}{\tan^2(i_0)}} d\varphi \tag{4-2}$$

Where $R(\varphi)$, R_0, i_0 and φ are the radius of each circumference, tool radius, helix angle and cutting angle gap between the i cutting edge element and the tool point. The expression for t_n is given by below:

$$t_n = f \sin(\psi)\sin(\kappa), if \begin{cases} 0 \le \kappa \le \kappa_{\lim} \\ 0 \le \psi \le \psi_{\lim} \end{cases} \tag{4-3}$$

And

$$t_n = 0, if \begin{cases} 0 \le \kappa \le \kappa_{\lim} \\ 0 \le \psi \le \psi_{\lim} \end{cases} \tag{4-4}$$

Where κ and ψ are the positioning angle from the center point to an arbitrary point in the OXZ plane and OXY plane. The length of the differential cutting edge perpendicular to the cutting direction, db can be presented by Equation (4-5):

$$db = \frac{da_p}{\sin(\kappa)} \tag{4-5}$$

In this model, the author focused on the algorithm for calculating the undeformed chip thickness and the length of cutting edge which contacted the chip. The values of feed, axial cutting depth and the tool path indirectly affect the final values of cutting force components through the values of *S* and *b*. According to the comparison of prediction and experimental results in this cutting force model, the agreement is good.

However, in some analytical cutting force models, the cutting force components just involve the specific shear coefficients. For example, Wan et al. [33] developed a new cutting force model which was based on the expressions of cutting force components in the form of Equation (4-6):

$$\begin{cases} \mathrm{F_T} = K_T h(\varphi) a_p \\ \mathrm{F_R} = K_R h(\varphi) a_p \\ \mathrm{F_Z} = K_Z h(\varphi) a_p \end{cases} \tag{4-6}$$

Where F_T, F_R and F_Z are equal to the value of F_t, F_r and F_a in the equation (4-1), respectively. The cutting force coefficients K_T, K_R and K_Z are equal to K_{tc}, K_{rc} and K_{ac}. The undeformed chip thickness t_n is presented by $h(\varphi)$ and axial cutting depth by a_p. This model was developed based on a study of a cylindrical end milling tool. The cutting force coefficients quoted the expressions from Kline's proposed form which considered the run out effect. The influences of feed and axial cutting depth can be seen through the comparison of prediction and experimental result.

4.2 Modeling of instantaneous cutting force

4.2.1 The instantaneous cutting force

The local cutting force components F_R, F_T and F_Z at arbitrary rotating angle are shown in Figure 4.4. And F_X, F_Y, F_Z are the force components in the machine coordinate system.

According the cutting force model proposed by Wan et al. [33], the three components of the cutting force in the local coordinate system (Figure 4.4 (a)) can be described with the following equation:

$$\begin{cases} F_T = K_T h(\varphi) a_p \\ F_R = K_R h(\varphi) a_p \\ F_Z = K_Z h(\varphi) a_p \end{cases} \tag{4-7}$$

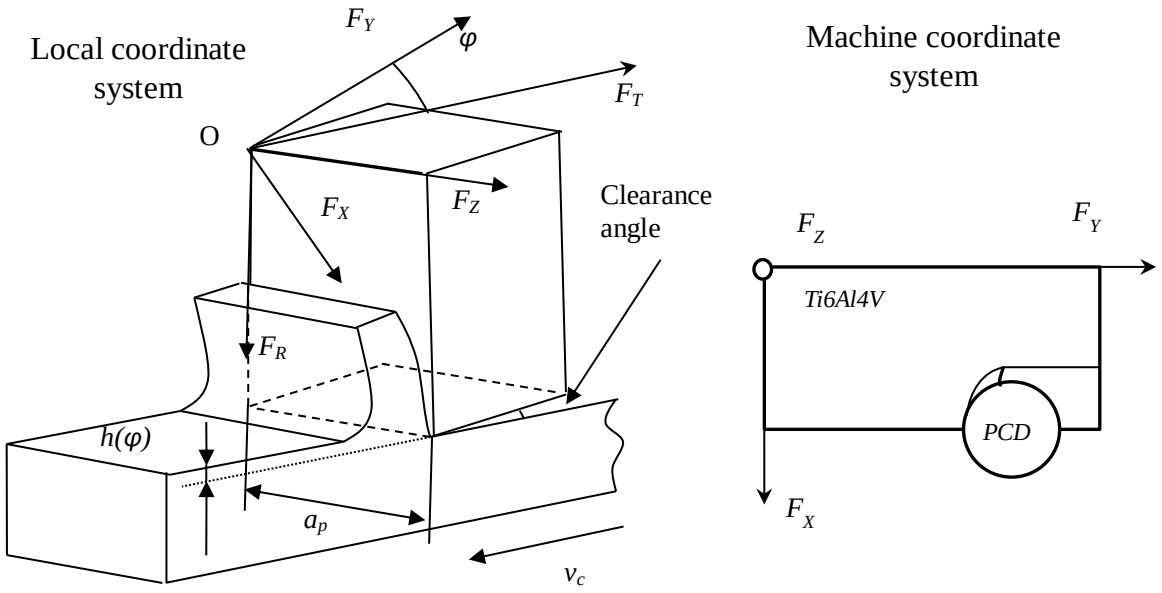

(a)

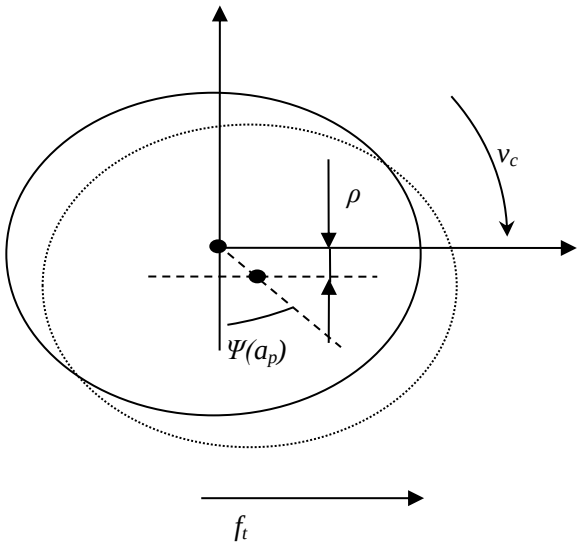

(b)

Figure 4.4 - The illustration of calculating cutting force (a) the illustration of cutting force components (b) the runout of cutting tool.

Where $h(\varphi)$ is the instantaneous uncut chip thickness and a_p is the axial cutting depth. K_T, K_R and K_Z are the cutting coefficients of the three force components and can be expressed as Equation (4-8).

$$\begin{cases} K_T = k_T[h(\varphi)a_p]^{-m_T} \\ K_R = k_R[h(\varphi)a_p]^{-m_R} \\ K_Z = k_Z[h(\varphi)a_p]^{-m_Z} \end{cases} \tag{4-8}$$

Where k_q and m_q (q=T, R, Z) are parameters relevant to the properties of the workpiece material. By substituting Equation (4-8) into Equation (4-7), the relationship between the uncut chip thickness and the components of local force can be written with Equation (4-9).

$$\begin{cases} F_T = k_T[h(\varphi)]^{1-m_T} a_p \\ F_R = k_R[h(\varphi)]^{1-m_R} a_p \\ F_Z = k_Z[h(\varphi)]^{1-m_Z} a_p \end{cases} \tag{4-9}$$

According to Kline and DeVor [32], the presence of runout increases the average chip thickness for the teeth actually engaged in the cut and increases the ratio of the maximum to average force. It also shifts the frequency of the force signal away from the tooth passing frequency to the spindle rotational frequency. The run out effect can be seen from Figure 4.4 (b). The centrifugal distance (ρ) and corresponding instantaneous rotation angle ($\Psi(a_p)$). It has been claimed that the theoretical chip thickness could vary by time changes. And, by considering the run out effect of the cutting tool, the uncut chip thickness $h(\varphi)$ can be described by Equation (4-10).

$$h(\varphi) = mf\sin(\varphi) + \xi \tag{4-10}$$

Where m is a parameter corresponding to the runout effect of the milling process, the relationship between time (t) and rotation angle (φ) can be expressed as t=($\varphi r/v$). Also, ξ describes the influence of the actual cutting radius on instantaneous uncut chip thickness:

$$\xi = \rho\cos(\lambda\text{-}\psi(a_p)\text{-}\frac{2\pi(\text{i-1})}{\text{N}})\text{-}\rho\cos(\lambda\text{-}\psi(a_p)\text{-}\frac{2\pi(\text{i-j-1})}{\text{N}}) \tag{4-11}$$

Where ρ is the parameter which represents the runout error.

Since the number of flutes of the PCD tools used in our experiment was one, according to Wan et al. [33], the instantaneous uncut chip thickness will not be affected by the runout effect. As such, the coefficients m and ξ will be defined as 1 and 0, and the instantaneous uncut chip thickness can be described by Equation (4-12).

$$h(\varphi) = f\sin(\varphi) \tag{4-12}$$

The measuring coordinate system is shown in Figure 4.4 (a). The tangential force (F_T), radial force (F_R) and axial force (F_Z) can be written in the matrix form as $[F]_{\text{T,R,Z}}$. The local cutting force matrix $[F]_{\text{T,R,Z}}$ can be obtained by multiplying the transformation matrix $[T]$ to the cutting force matrix $[F]_{X,Y,Z}$:

$$[\text{F}]_{\text{T,R,Z}} = [T][F]_{X,Y,Z} \tag{4-13}$$

Where matrix [T] can be expressed by Equation (4-14).

$$[T]=\begin{bmatrix} \cos\varphi & \sin\varphi & 0 \\ -\sin\varphi & \cos\varphi & 0 \\ 0 & 0 & 1 \end{bmatrix} \tag{4-14}$$

4.2.2 Cutting force coefficients

By substituting the machining parameters and values of the corresponding cutting forces in each test into Equation (4-7) and Equation (4-12), the cutting force coefficients for the same rotation angle which equals to 18^{o}, as illustrated Figure 4.5 can be arrived at. These coefficients are only relevant to the instantaneous uncut chip thickness, which is a function of feed and instantaneous rotation angle. However, according to the calculation results in Figure 4.5 (a) and (c), the changes of cutting speed and axial cutting depth could lead to dramatic variations of cutting force coefficients. In Figure 4.5 (a), the cutting coefficients K_T and K_R increase with an increase of cutting speed while there is less change in K_z when the cutting speed changes. As shown in Figure 4.5 (b), the three cutting coefficients drop with an increase of feed. Figure 4.5 (c) shows that coefficients K_R and K_Z decrease with an increase of axial cutting depth and K_T remains nearly constant. Therefore, it can be concluded that the change of feed has significant influence on the three cutting coefficients (Figure 4.5 (b)). The change of cutting speed can only affect the cutting coefficients K_T and K_R. Because the relationship between cutting speed and cutting coefficient are nonlinear, as illustrated in Figure 4.5 (a), the curves of K_T and K_R indicate that an exponential relationship exists between the two coefficients and the cutting speed. As shown in Figure 4.5 (c), the change of axial cutting depth significantly influences all the cutting coefficient*s* with an exception of K_T. The relationship between K_R, K_Z and axial cutting depth can also be assumed to be exponential.

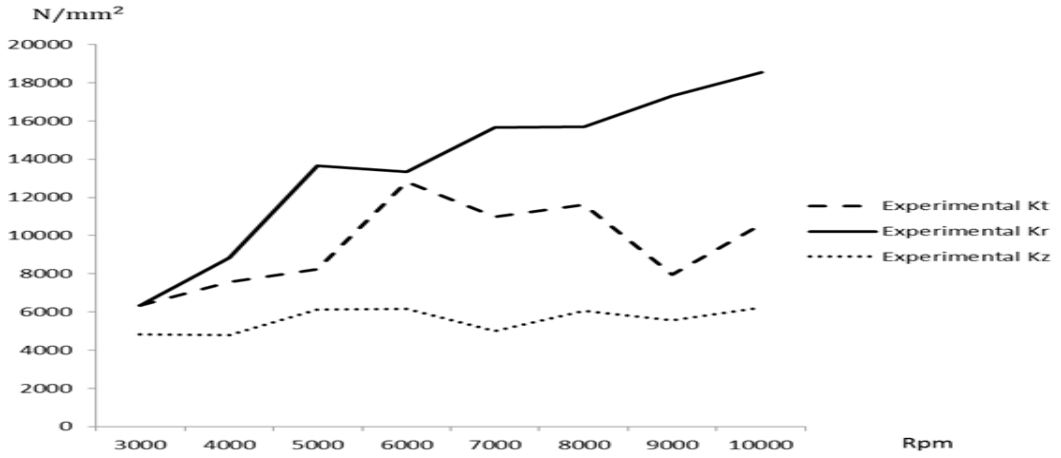

(a)

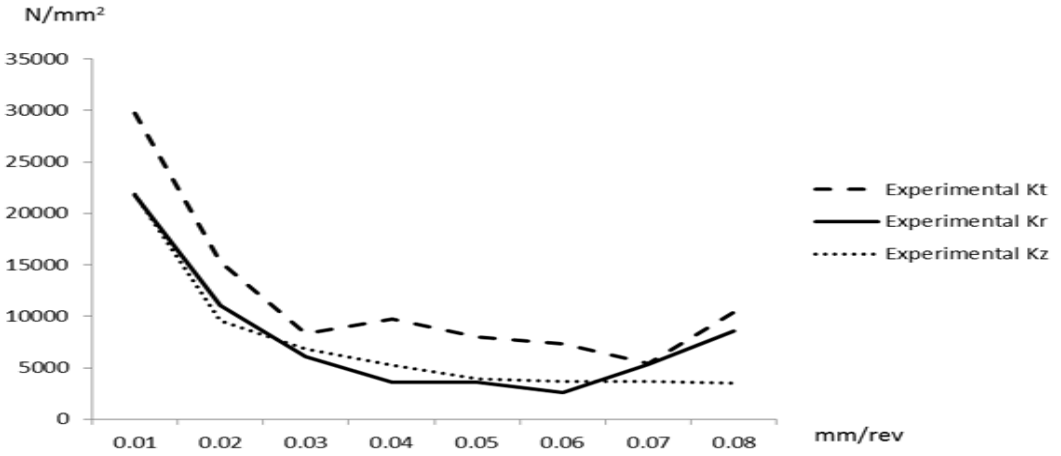

(b)

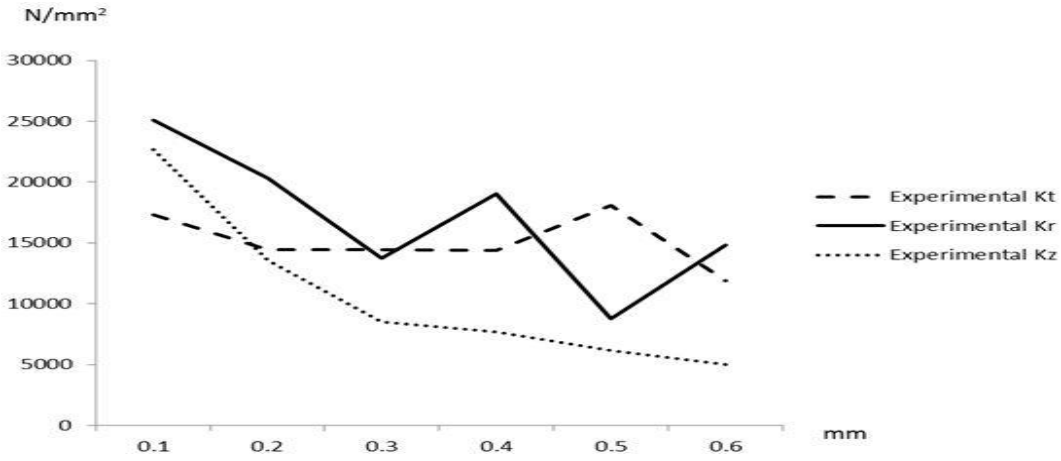

(c)

Figure 4.5 - The calculation of cutting coefficient with different machining conditions: (a) Effect of cutting speed; (b) Effect of feed; (c) Effect of cutting depth.

Hence, based on above conclusions and experimental results, an improved cutting coefficient can be described more accurately by Equation (4-15)

$$\begin{cases} K_T = k_t v^{n_T} h(\varphi)^{-m_T} \\ K_R = k_r v^{n_R} a_p^{l_R} h(\varphi)^{-m_R} \\ K_Z = k_z a_p^{l_Z} h(\varphi)^{-m_Z} \end{cases} \tag{4-15}$$

The cutting constants k_t, k_r, k_z, l_R, l_Z, n_T, n_R, m_T, m_R, m_Z can be calculated in three steps:

(1) Determine Constants m_T, m_R and m_Z.

In Tests 9 - 16, which were to investigate the effects of feed, the cutting speed and axial cutting depth were held constant. The calculation matrix for the three constants can be derived using Equation (4-16). According to the expressions of S_T, S_R and S_Z, though the rest of constants are still unknown, their values will not change because the values of cutting speed and axial cutting depth are constant. Therefore, by substituting the data of Figure 4.5 (b) and corresponding feed into Equation (4-16), the final values of m_T, m_R and m_Z can be calculated with the Levenberg-Marquardt Method [92][93].

$$\begin{bmatrix} K_{T,1} \\ \vdots \\ K_{T,N} \\ K_{R,1} \\ \vdots \\ K_{R,N} \\ K_{Z,1} \\ \vdots \\ K_{Z,N} \end{bmatrix} = \begin{bmatrix} S_T[f_1 \sin(\varphi)]^{-m_T} \\ \vdots \\ S_T[f_N \sin(\varphi)]^{-m_T} \\ S_R[f_1 \sin(\varphi)]^{-m_R} \\ \vdots \\ S_R[f_N \sin(\varphi)]^{-m_R} \\ S_Z[f_1 \sin(\varphi)]^{-m_Z} \\ \vdots \\ S_Z[f_N \sin(\varphi)]^{-m_Z} \end{bmatrix} \tag{4-16}$$

Where S_T, S_R and S_Z are as Equation (4-17).

$$\begin{bmatrix} S_T \\ S_R \\ S_Z \end{bmatrix} = \begin{bmatrix} k_t v^{n_T} \\ k_r v^{n_R} z^{l_R} \\ k_z z^{l_Z} \end{bmatrix} \tag{4-17}$$

(2) Determine Constants k_t, k_z, n_T and l_Z.

Based on the calculation in Step 1, Equation (4-18) can be derived from Equation (4-15). To calculate constants k_t and n_T, cutting coefficients K_N ($N=0, 1 \ldots 8, N \geq 2$) and machining parameters of Tests 1 - 8 were used. Similarly, cutting coefficients K_N ($N=0, 1 \ldots 6, N \geq 2$) and machining parameters of Tests 17 - 22 were used in calculating k_z and l_Z. It is worth noting that the rotation angles which were used to calculate cutting coefficients were the same, and the feed of Tests 1 - 8 and Tests 17 - 22 were 0.025 mm/rev and 0.03 mm/rev, respectively. Therefore, the values of F_T and F_Z should be constant in the calculation.

$$\begin{bmatrix} K_{T,1} \\ \vdots \\ K_{T,N} \\ K_{Z,1} \\ \vdots \\ K_{Z,N} \end{bmatrix} = \begin{bmatrix} k_t v_1^{n_T} F_T \\ \vdots \\ k_t v_N^{n_T} F_T \\ k_z a_{p,1}^{l_Z} F_Z \\ \vdots \\ k_z a_{p,N}^{l_Z} F_Z \end{bmatrix} \tag{4-18}$$

Where

$$\begin{bmatrix} F_T \\ F_Z \end{bmatrix} = \begin{bmatrix} [f \sin(\varphi)]^{-m_T} \\ [f \sin(\varphi)]^{-m_Z} \end{bmatrix} \tag{4-19}$$

(3) Determine Constants k_r, n_R and l_R.

Figure 4.5 indicates that the value of K_R is affected by cutting force, feed and axial cutting depth. And the relationship between this coefficient and the three machining parameters is exponential. Firstly, to calculate constant n_R, the cutting coefficients of Tests 1 - 8 and the corresponding cutting speeds are substituted into Equation (4-20). Then, by using the same method, constant l_R is calculated with the cutting coefficients of Tests 17 - 22 and corresponding cutting speeds. Finally, the last constant k_r can be obtained based on the calculation in Step 2.

$$\begin{bmatrix} K_{R,v_1} \\ \vdots \\ K_{R,v_N} \\ K_{R,a_{p,1}} \\ \vdots \\ K_{R,a_{p,N}} \end{bmatrix} = \begin{bmatrix} G_R v_1^{n_R} F_{R_1} \\ \vdots \\ G_R v_N^{n_R} F_{R_1} \\ H_R a_{p,1}^{l_R} F_{R_2} \\ \vdots \\ H_R a_{p,N}^{l_R} F_{R_2} \end{bmatrix} \tag{4-20}$$

Where

$$\begin{cases} G_R = k_r a_p^{l_R} F_{R_1} \\ H_R = k_r v^{n_R} F_{R_2} \\ F_{R_N} = [f_N \sin(\varphi)]^{-m_R}, N = 1,2 \end{cases} \quad (4\text{-}21)$$

4.3 Model validation

4.3.1 Material properties

The samples of PCD insert and disc and the customized PCD end milling tool of 6 mm in diameter is shown in Figure 4.6. The helix angle and clearance angle of the tool are: 0^o and 10^o respectively.

The fabrication of the PCD tool was carried out in three steps: (a) cut PCD blank into small inserts; (b) braze an insert on a carbide substrate; (c) grind and shape the cutting edges to the required dimension and surface finish. Since diamond is one of the hardest materials in the world, the cutting and grinding process (a) and (c) are very difficult. Wire Electrical Discharge Machining (W-EDM) was used to cut small PCD inserts from a large blank (Figure 4.6 (a)), and Electrical Discharge Grinding (EDG) was employed to grind the PCD insert brazed on the tool body to produce the desired geometry and surface roughness of the PCD cutting tool. Figure 4.7 (a) shows the SEM (Philip XL 30) image of the new PCD tool. It can be seen that tiny notches which are less than 10 μm exist on the edge of the PCD insert.

Figure 4.6 - Single tooth PCD tool.

Table 4.1 Properties of PCD

Type of PCD	Grain size (μm)	Elastic modulus(MPa)	Hardness (GPa)	Density (g/cm3)	Thermal conductivity (w/mk)
CTB010	2 - 30	890-900	50(8000HV)	4.12	540

The properties of PCD material are known to play an important role in the machining process. Different PCD materials may demonstrate different performance in the milling process due to the difference in particle sizes and the proportion of diamond particles to metal. Properties of the PCD material used in this research (CTB010 made by Element Six) are shown in Table 4.1 [94]. Chemical components measured with the X-ray diffraction method are illustrated in Figure 4.7. The vertical axis represents the count rate of chemical element; the horizontal axis represents the x axis is an angle (2 theta) it relates to the crystal spacing. It can be seen in Figure 4.7 (b) that the major component of the PCD is diamond, only a small amount are cobalt and tungsten carbide which comes from the substrate. This type of PCD material is suitable for applications requiring super-finishing, finishing and general purpose machining.

The material of the workpiece is Ti6Al4V. This is an "Alpha + Beta" type of Titanium alloy. It is widely used in aerospace industry and has demonstrated superior overall performance. Four blocks of such material were used in the experiments. The chemical composition and mechanical properties of Ti6Al4V are illustrated in Table 4.2 [95] and Table 4.3 [18] respectively.

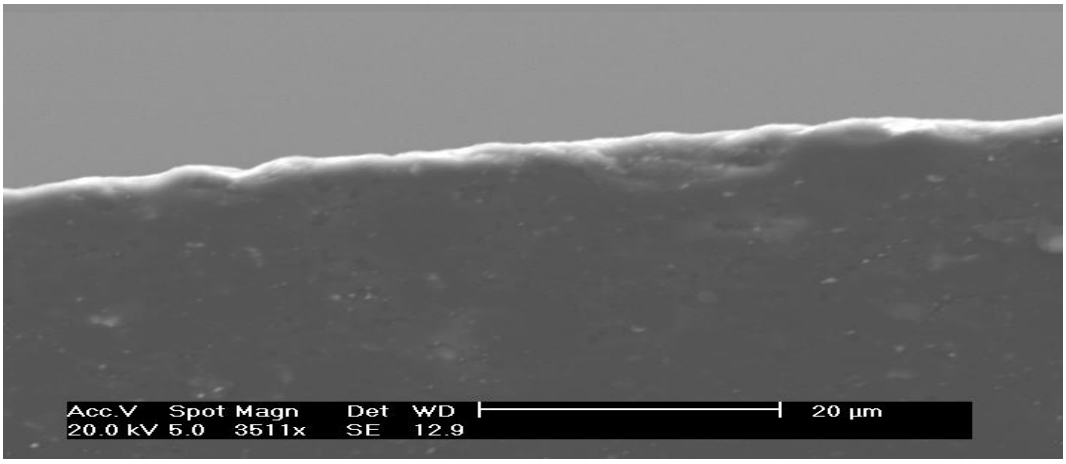

(a)

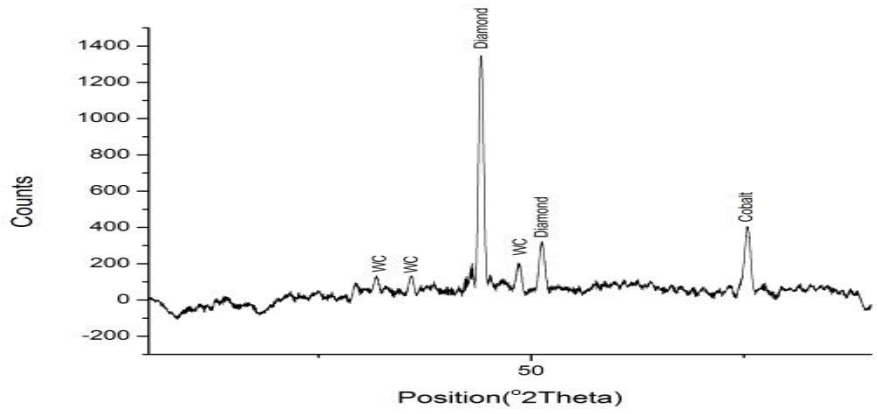

(b)

Figure 4.7 - (a) SEM image of the new PCD tool; (b) X-ray diffraction of PCD inserts.

Table 4.2 Chemical composition of Ti-6%Al-4%V

Contents	Al	V	Fe	O	C	H	N	Ti
Composition (wt %)	5.5-6.75	3.5-4.5	<0.25	<0.2	<0.08	<0.01	<0.05	Base

Table 4.3 Mechanical properties of titanium alloys

Tensile strength (Mpa)	Elastic modulus (GPa)	Poisson's ratio	Density (kg/cm^3)	Melting point (℃)	Hardness (HRC)	Thermal conductivity (W/mk)
932	114	0.33	4430	1668	36	6.7

4.3.2 Experimental set up

Twenty two cutting experiments were carried out on a 4-axis HAAS milling machine. An electrical signal proportional to cutting force was collected through a 6-channel dynamometer (Kistler 9257B) installed underneath the workpiece. The signal was amplified using a Kistler Multiple Charge Amplifier 5070. The force single was recorded via a DAQ (National Instrument model 6036E) card onto a personal computer. The sampling frequency is 20 KHz. The setup of the experimental system was illustrated in Figure 4.8. To simplify the analysis, the tool paths applied in the cutting tests were straight lines along the edge of the workpiece. The experiment was performed with the machining parameters of cutting speed, axial cutting depth and feed as in Table 4.4. The radial cutting depth was set to be constant as 3.5 mm and the cooling method was flooding.

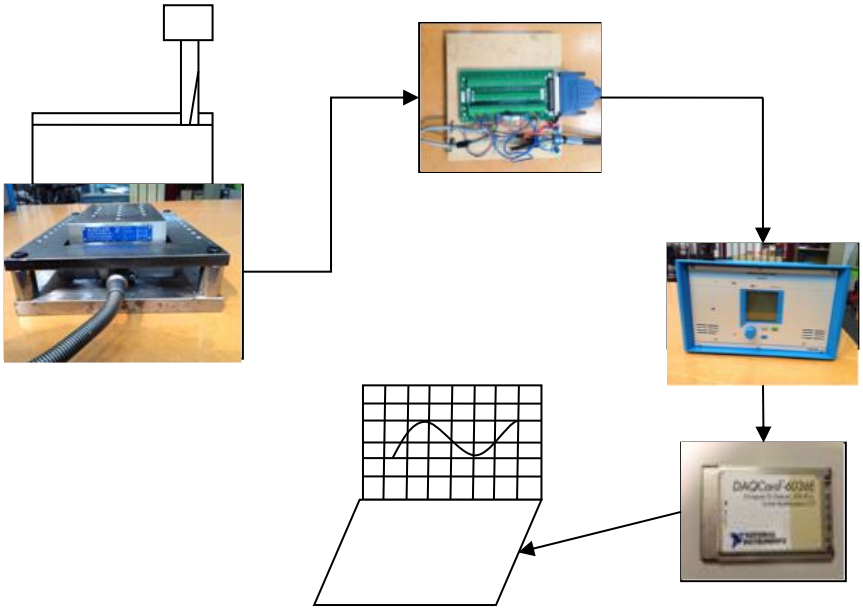

Figure 4.8 - Experimental system setup.

Table 4.4 Cutting parameters

Test number	Cutting speed (mm/min)	Axial cutting depth (mm)	Feed (mm/rev)	Material removal rate (mm^3/min)
1	65973.445	0.2	0.025	52.5
2	87964.593	0.2	0.025	70
3	109955.74	0.2	0.025	87.5
4	131946.89	0.2	0.025	105
5	153938.04	0.2	0.025	122.5
6	175929.19	0.2	0.025	140
7	197920.33	0.2	0.025	157.5
8	219911.48	0.2	0.025	175
9	131946.89	0.2	0.01	42
10	131946.89	0.2	0.02	84
11	131946.89	0.2	0.03	126
12	131946.89	0.2	0.04	168
13	131946.89	0.2	0.05	210
14	131946.89	0.2	0.06	252
15	131946.89	0.2	0.07	294
16	131946.89	0.2	0.08	336
17	131946.89	0.1	0.025	52.5
18	131946.89	0.2	0.025	105
19	131946.89	0.3	0.025	157.5
20	131946.89	0.4	0.025	210
21	131946.89	0.5	0.025	262.5
22	131946.89	0.6	0.025	315

4.4 Result and analysis

4.4.1 Influence of machining parameters

By using the cutting force record and the corresponding machining parameters, the calculation results of cutting coefficients are listed in Table 4.5 with the calculation method of step 1 - 3.

Table 4.5 Cutting force coefficients

kt	k_r	k_z	n_T	n_R
15.8601	0.0376	39.8531	0.3232	0.7346
m_T	m_R	m_Z	l_R	l_Z
0.7992	0.9401	1.0795	-0.3867	-0.8174

4.4.2 Comparison of simulation and experimental results

By substituting the cutting force coefficients in Table 4.5 into the cutting force model, the relationship between the average peak cutting force in each milling cycle and the three machining parameters can be generated (Figure 4.9). To simplify the analysis, the average

resultant forces of each milling cycle were calculated with Equation (4-22). The experimental values of F_T, F_R and F_Z were calculated with Equation (4-13) and the predicted results for these three values could be obtained from the cutting force model with cutting force constants of Table 4.5. As shown in Figure 4.9, the simulation results match the experimental results to a high degree of accuracy.

$$F = \sqrt{F_T^2 + F_R^2 + F_Z^2} \tag{4-22}$$

It is known that a change in machining parameters would directly affect the instantaneous cutting force. For example, in high speed milling of Ti6Al4V alloy with PCD tools, it was found that the cutting force dropped when the cutting speed was increased [7]. The cause which leads to such phenomenon was that the low thermal conductivity and insufficient heat dissipation results in the rise of regional cutting temperature when the cutting speed is increased. The consequent softening effect finally causes the drop of cutting force.

However, the situation is quite different in this study, by applying PCD in the process of milling Ti6Al4V with the conventional cutting speed, which is range from 65 m/min to 22 m/min, the cutting force increases with the cutting speed as shown in Figure 4.9 (a).

As shown in Figure 4.9 (a), the difference between the maximum and minimum resultant forces is around 12 N, and the experimental result shows an instability in the cutting force when the cutting speed was set to 175929.19 mm/min, which could be the combined results of the impact effect and the thermal softening effect of the machining process. As shown in Figure 4.9 (b), the cutting force increases exponentially with an increase of feed when the cutting speed and axial cutting depth were held constant. In Figure 4.9 (c), in contrast to the experimental result of feed, the speed of the increase of cutting force slowed down when larger axial cutting depth was applied while the cutting speed and feed were constant.

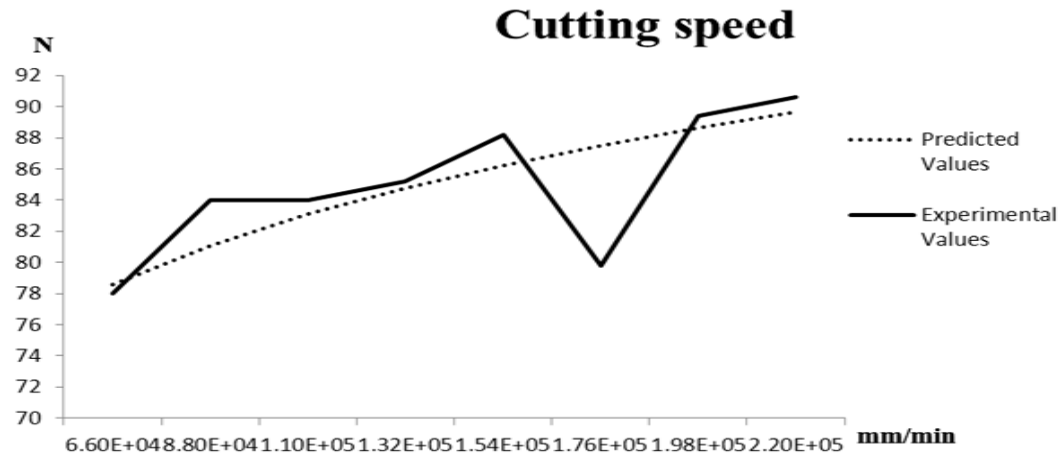

(a)

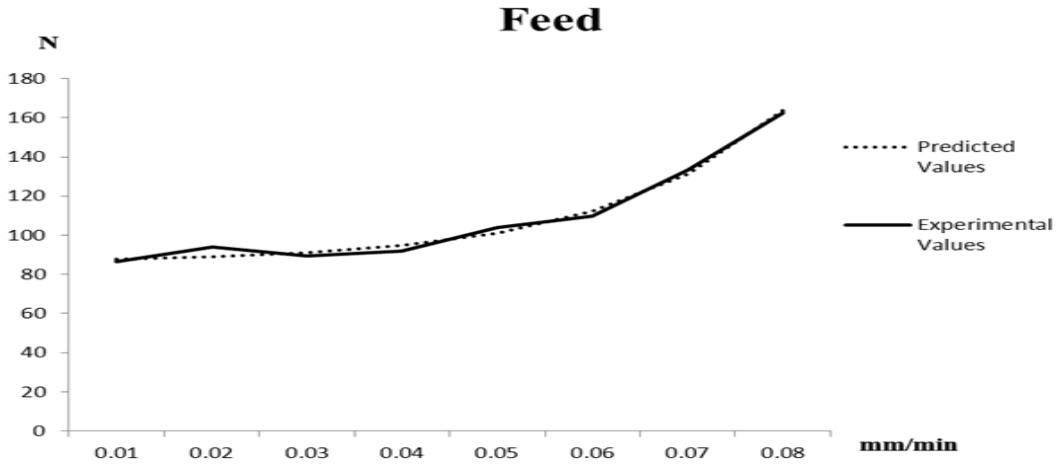

(b)

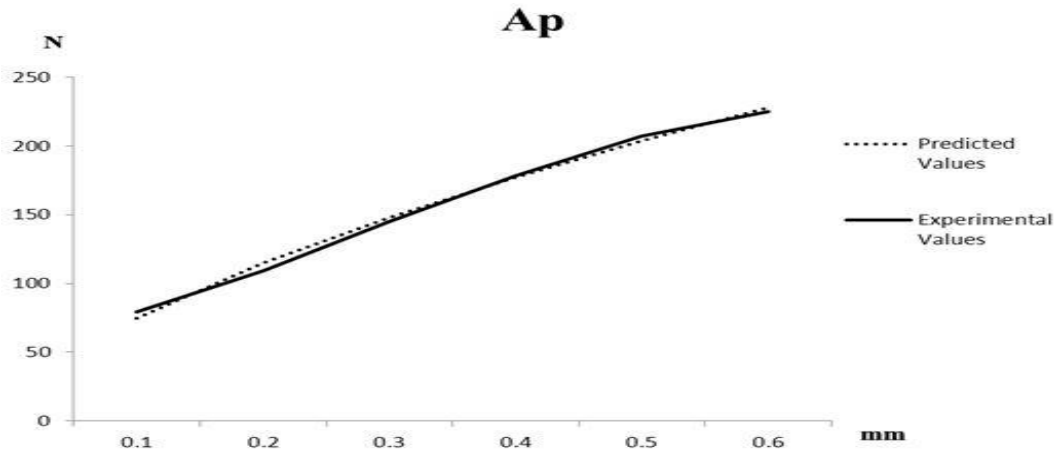

(c)

Figure 4.9 - Influence of machining parameters on cutting force: (a) the relationship of instantaneous cutting force and linear velocity of cutting tip; (b) The relationship of instantaneous cutting force and feed; (c) The relationship of instantaneous cutting force and axial cutting depth (Ap).

4.4.3 The instantaneous cutting force

Figure 4.10 shows the instantaneous cutting force curve of single milling cycle. The maximum value of cutting force can be found at the cutting angle 15^o - 20^o of most the instantaneous cutting force curves in the experiment. Then, a significant drop appears at the following stage before the next small peak. Theoretically, the fluctuation of cutting force in a single milling cycle is not supposed to exist. And many previous studies have not mentioned on these fluctuations [33] [96-98]. To solve this issue, the instantaneous cutting force can be deduced as Equation (4-23) which can accurately describe the instantaneous cutting force changes by time.

As Equation (4-23), the formulation of instantaneous cutting force F_{dy} is developed by introducing the Levenberg-Marquardt Method. The F_{max} equals to the peak cutting force which can be determined by the model described in section *4.2.1*. The value of time (t) is the only variable in the rest of the function and it is equal to $t=(\varphi r/v)$ where φ is the cutting angle of tool. According to the experimental results, the significant fluctuation of instantaneous cutting force finish at the cutting angle around 55^o and the exit angle of each cutting cycle is around 120^o.

Figure 4.11 illustrates the 2-step flow chart for the prediction of instantaneous cutting force.

- Step 1 is to determinate the cutting parameters with the method introduced in Sections 3.1 and 3.2;
- Step 2 is to calculate the peak value of cutting force with corresponding machining parameters and to calculate the instantaneous cutting force by iterating by time with Equation (4-23).

Figure 4.12 shows the predicted and real instantaneous cutting force of Test 6 and Test 8. The predicted tangential, radial and axial cutting forces highly match the experimental results. It can be seen that the maximum error in prediction (the difference between the predicted and real peak values) is less than 7 *N*.

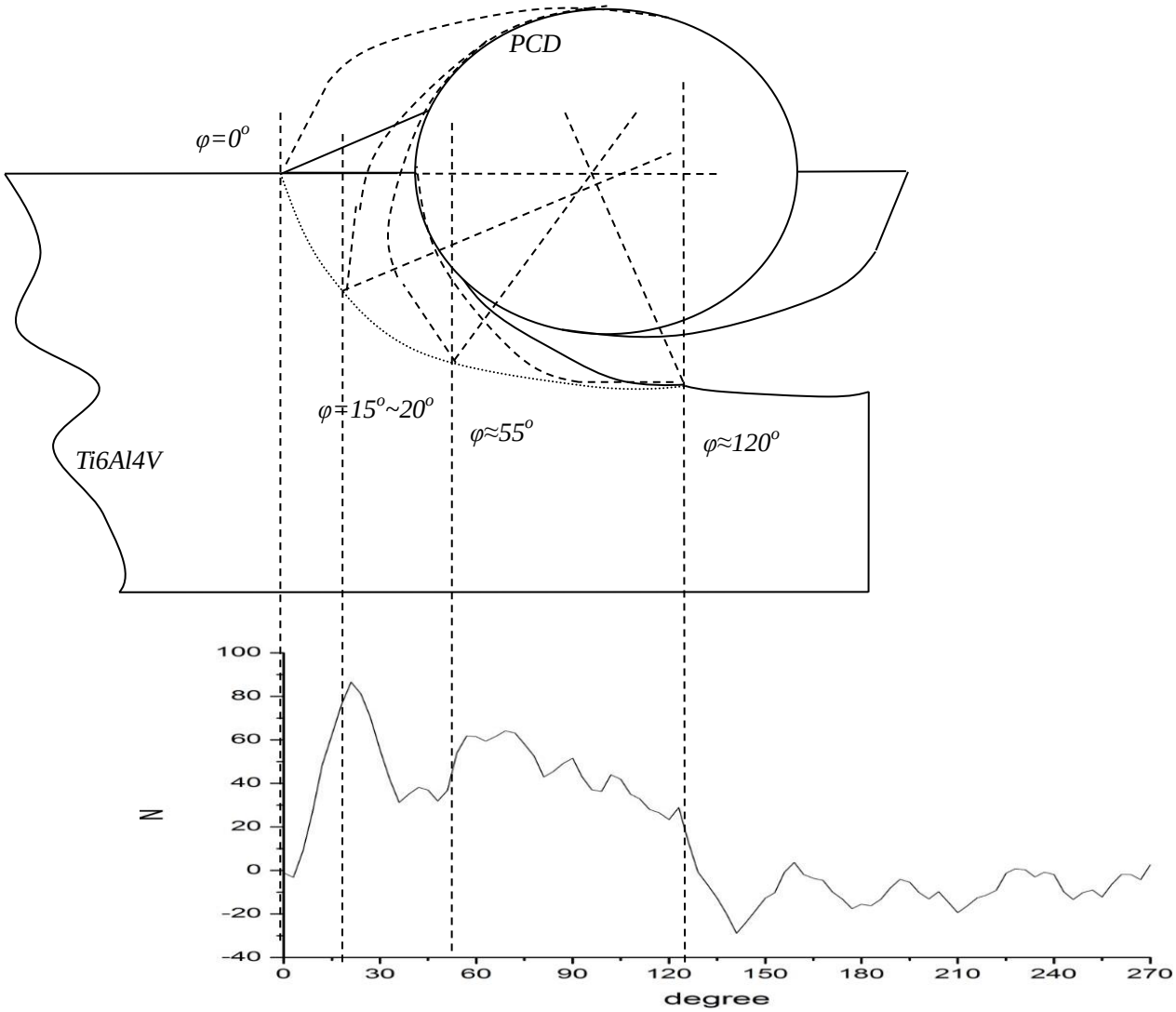

Figure 4.10 - Illustration of tool rotation and corresponding instantaneous cutting force.

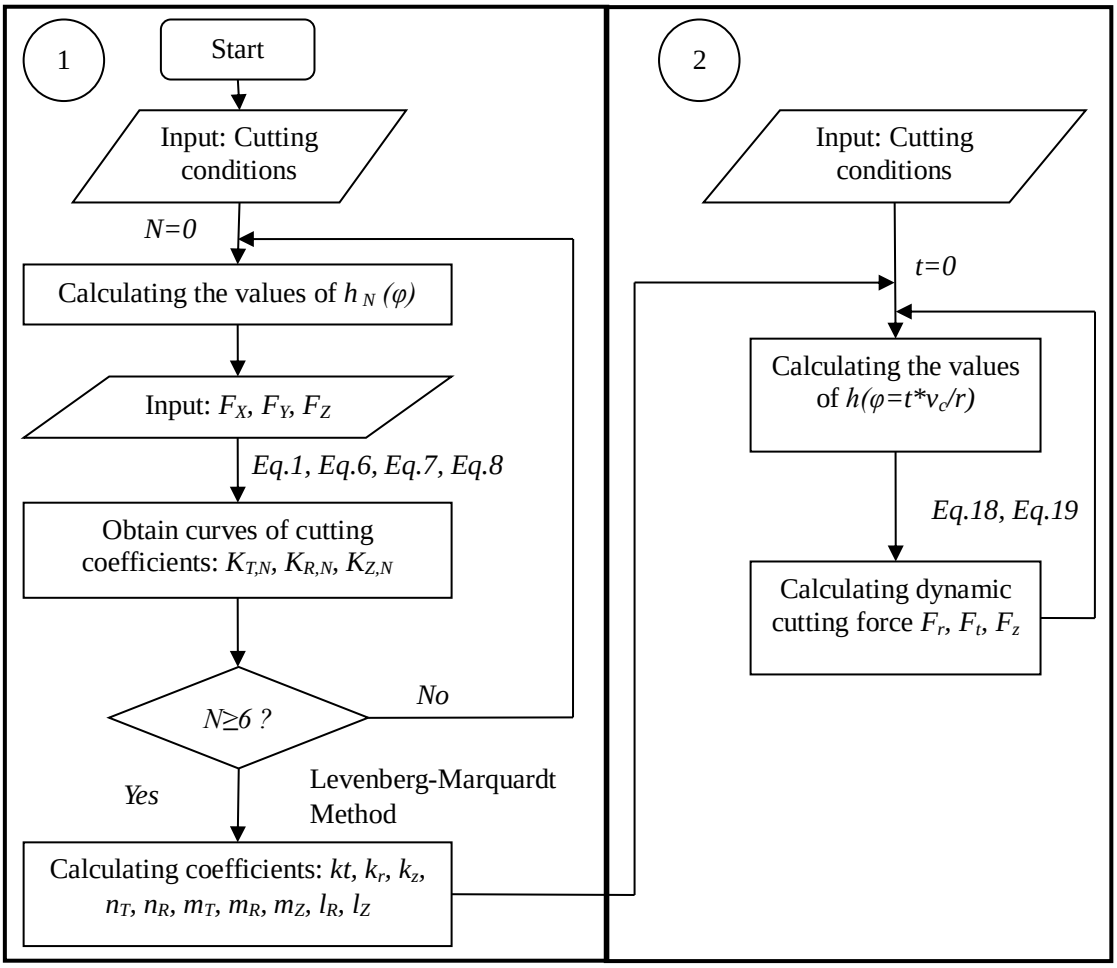

Figure 4.11 - Flow chart of instantaneous cutting force prediction.

$$F_{dy}=\begin{cases} F_{max}\left(0.536t+\dfrac{1.3333}{56.7492(t-0.2442)^2+1.3324}\right), 0<t\le\dfrac{55^o}{0.006n} \\ F_{max}(35.01874-25.4152t+13.72487t^2-4.58519e^t-10.1243/t), \dfrac{55^o}{0.006n}<t\le\dfrac{120^o}{0.006n} \end{cases} \quad (4\text{-}23)$$

Where

$$F_{max}=\begin{cases} k_t v^{n_T} f^{1-m_T} z \\ k_r v^{n_R} z^{1+l_R} f^{1-m_R} \\ k_z z^{1+l_Z} f^{1-m_Z} \end{cases} \quad (4\text{-}24)$$

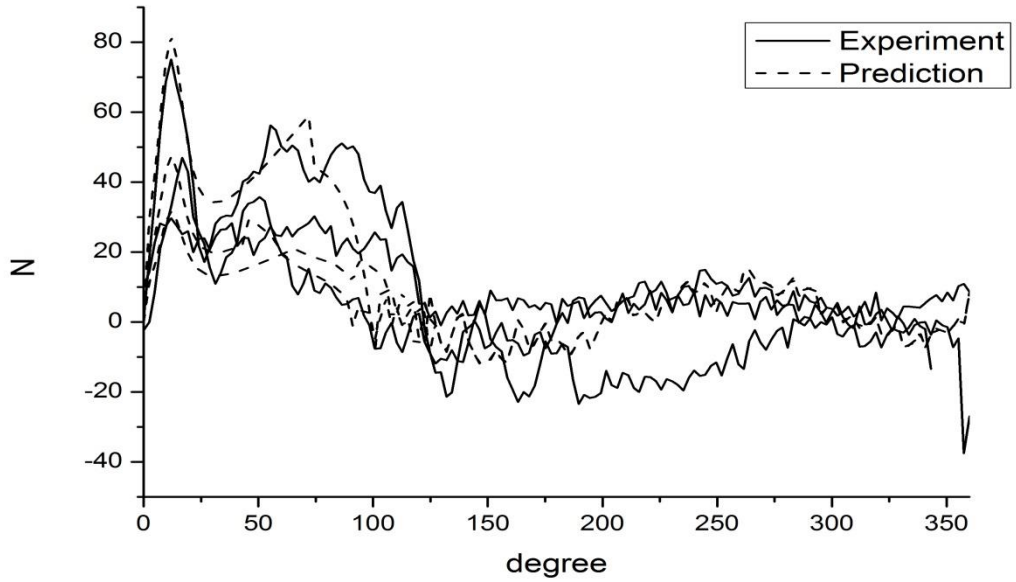

(a)

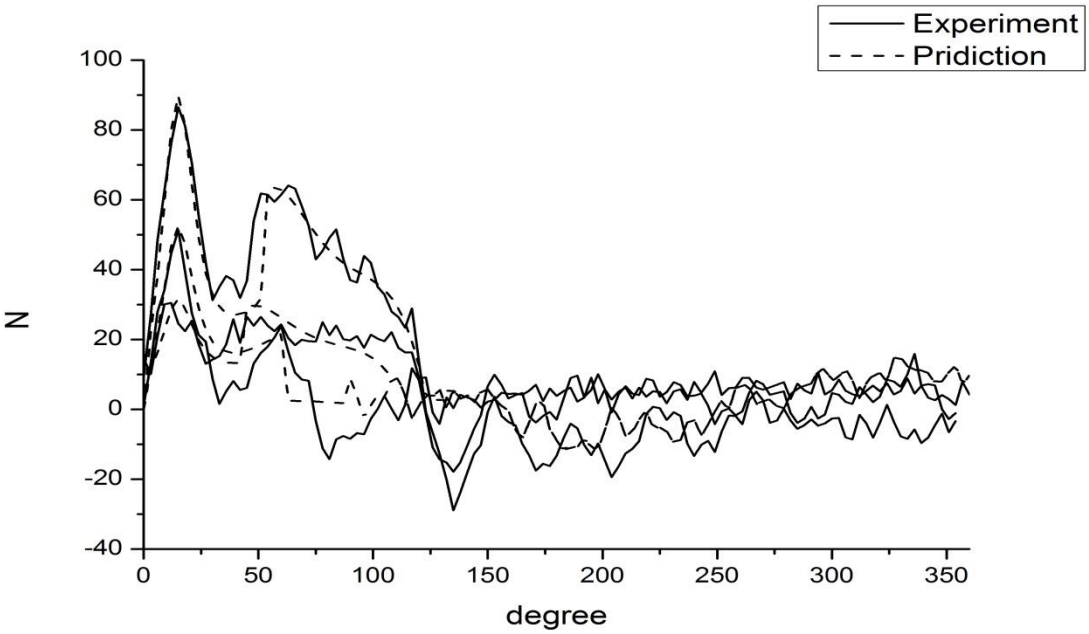

(b)

Figure 4.12 - The instantaneous cutting force curves: (a) Test 6; (b) Test 8.

4.5 Summary

A new cutting force prediction model was developed based on the variable machining parameters for the prediction of cutting forces in milling Ti6Al4V with brazed PCD tools. A new method which is applicable to a wide range of machining parameters has been proposed to improve the calculation of cutting force coefficients. It has been concluded that changes in machining parameters can significantly affect the values of the cutting coefficients. Based on this conclusion, the proposed model in this work can successfully predict the peak values of cutting force by entering the machining parameters. Furthermore, the experimental results show that fluctuations of cutting force existed in each milling cycle. To predict the instantaneous cutting force accurately, a time-dependent cutting force model has also been developed. Validation was conducted through cutting tests with single flute PCD end mills. The maximum predictive error of the peaks of cutting forces was found to be less than 7 N.

5 Thermal analyses

This chapter includes two main parts: the development of new cutting temperature model and the chemical analysis. Based on the analysis of experimental results cutting parameters such as cutting speed, feed and axial cutting depth were found to have significant influence on the cutting temperature. The research was focused on the deduction of cutting temperature equations by considering the influence of machining parameters. The chemical damage was one of the important failure forms. Through chemical analysis of used PCD tool, it was concluded that the temperature in local region of tool nose was up to 500^{o}C.

5.1 Introduction

5.1.1 Model of dynamic cutting temperature

According to Groover [87], nearly 98% of total energy consumed in machining is converted into heat. This heat always causes extremely high cutting temperature as discussed in many research works. Some workpiece materials such as the alloys which contain the element Titanium may have a chemical reaction with tool materials. Besides, the high cutting temperature may lead to the finished surface of workpiece becoming soft or undergoing deformation. Finally, the surface will be found to be poor quality. Therefore, the study of the characteristics of cutting temperature is one of the most popular areas for applying new tool materials. According to the current state of knowledge of predicting cutting temperature, there are three different methods: the simple analytical equation; quasi-closed form heat transfer analysis and FEM method. These models focus on analyzing the influence of different factors which can affect the cutting temperature. The factors are discussed in the following sections.

5.1.2 The factors involved in the empirical cutting temperature model

According to Cook [99], the simple analytical equation for predicting cutting temperature based on dimensional analysis can be expressed as Equation (5-1).

$$\Delta T = \frac{0.4U}{\rho C}\left(\frac{vt_o}{K}\right)^{0.333} \tag{5-1}$$

Where ΔT is the cutting temperature, U, ρC, K, v, t_o are specific energy in the operation, volumetric specific heat of the work material, thermal diffusivity of workpiece, cutting speed and undeform chip thickness respectively.

From this equation, the machining parameters (cutting speed v and undeformed chip thickness t_o)

have an exponential relationship with the cutting temperature. The thermal properties of the material, such as thermal conductivity *C* and thermal diffusivity *K*, can also directly affect the cutting temperature. However, in many studies involving cutting temperature, the thermal properties of the material are assumed to be constant for the whole process in order to simplify the analysis.

5.1.3 Important factors in the analytical cutting temperature model

An accurate way of predicting cutting temperature is to set up the quasi-closed form heat transfer analysis as in the method of Loewen and Shaw [100]. This method considers more factors which can affect the cutting temperature such as the geometrical factors, cutting heat and thermal properties of tool and workpiece. The thermal properties of tool and workpiece are always assumed to be constant. Many research works only focused on the algorithm of calculating cutting temperature by considering the dimensional factors and the factors related to cutting heat. The dimensional factors in the cutting temperature model include the location of the measuring point in different heat source coordinate systems, the tool geometrical parameters and the tool path geometrical parameters. The factors which can affect heat generation in the machining process include machining parameters such as cutting speed, feed, axial cutting depth, radial cutting depth and some other factors which can affect the cooling or the heat dissipation.

The algorithm for calculating the amount of heat generated in the cutting process and the heat transfer dimension are two aspects involved in the new cutting temperature model. By studying the transient temperature in a face milling process, Cui et al. [46] proposed a new cutting temperature model with the expression of cutting heat and tool-chip contact length as Equation (5-2).

$$\begin{cases} q(h(\varphi)) = 5.295\cdot 10^{14}\cdot h(\varphi)^2 - 4.414\cdot 10^{11}\cdot h(\varphi) + 2.066\cdot 10^{8} \\ L_Y = -2845\cdot h(\varphi)^2 + 3.145\cdot h(\varphi) + 1.065\cdot 10^{-5} \end{cases} \tag{5-2}$$

Where $h(\varphi)$ is the undeformed chip thickness.

The factors in expression of (5-2) were determined by experiment. The heat generation and tool-chip length are determined by the value of undeformed chip thickness. And the final expression of average cutting temperature is

$$T_{AVE} = \frac{1}{(x_b - x_a)(y_d - y_c)} \int_{x_a}^{x_b} \int_{y_c}^{y_d} \int_0^t \theta_{GR} \cdot q(\tau) d\tau dy dx \tag{5-3}$$

Where t, τ are the overtime and the differential time, the x_a, x_b, y_c, y_d,are the position of the calculating point. θ_{GR} can be expressed with the Green's function in the form of Equation (5-4).

$$\theta_{GR} = \frac{1}{4\sqrt{\alpha\pi(t-\tau)}} \exp\left(\frac{-z^2}{2\sqrt{\alpha(t-\tau)}}\right)\left(erf\left(\frac{L_X + x}{2\sqrt{\alpha(t-\tau)}}\right) + erf\left(\frac{L_X - x}{2\sqrt{\alpha(t-\tau)}}\right)\right)\left(erf\left(\frac{L_Y + y}{2\sqrt{\alpha(t-\tau)}}\right) + erf\left(\frac{L_Y - y}{2\sqrt{\alpha(t-\tau)}}\right)\right) \quad (5\text{-}4)$$

Where the L_X is the cutting depth and z is the normal distance of measuring point from the tool-chip interface. Figure 5.1 shows the illustration of heat source and measuring area.

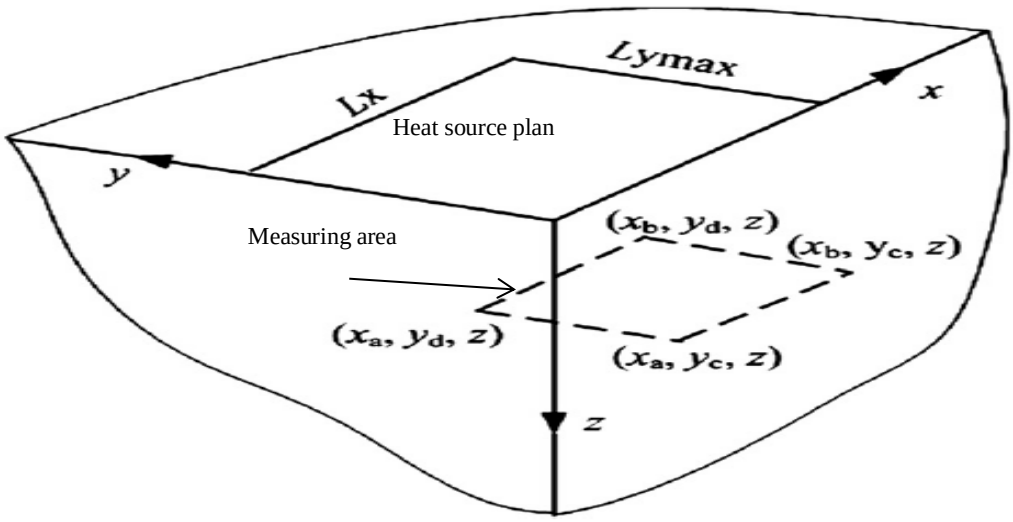

Figure 5.1 - Illustration of heat source and measuring area [46].

Based on a similar theory derived from solid heat conduction theory, Lin developed a new cutting temperature model which predicts the cutting temperature of an arbitrary point in workpiece. However, in contrast to Cui's model, Lin assumed that both shearing effect and friction effect contributed to the cutting temperature of any arbitrary point in the workpiece [45].

5.1.4 The impact factors in FEM model

The FEM simulation is convenient to predict cutting temperature. Generally, by applying the FEM simulation, the detailed temperature distribution and transient heat transfer can be obtained. And the amount of heat generated is easy to calculate. As for the impact factors of this method, the mesh quality, material model selection and the model idealization will affect final convergence of the temperature model. Another consideration is that, as mention in Chapter 4, long cutting lengths are is hard to simulate by FEM method due to excessive computation requirements.

5.1.5 The measurement of cutting temperature

Two major methods are applied in modern thermal analysis of machining process for cutting temperature measurement: Infrared Camera monitoring method; to use thermal couple wire; to use laser sensor.

The infrared camera is the most convenient way to measure the cutting temperature. There are some advantages by applying this method: the great adaptability of different process such as milling, turning and drilling; is the repeatable method, namely, measure the cutting temperature without any damage. As for the disadvantages, infrared camera method can just measuring the average temperature of the cutting area which means the accuracy of this method is lower by comparing with the method of using thermo-couple wire. Besides, the records cannot be saved as the exact value.

Generally, for applying the infrared camera measuring method, there are three simple steps to follow:

1. To fix the infrared camera within the available range in the machining system.
2. To manually record the cutting temperature.
3. To analyze the infrared pictures which record the cutting temperature of machining process.

By applying thermo-couple wire method, the wire needs to be wielded on the workpieces or cutters. The heat flux changes in the process will be transferred into the voltage signal. And this signal can be amplified through the amplifier. Finally, the voltage signal can be received and saved by the computer. The advantages for this method are: more accurate method for measuring temperature; continuous recording the dynamic cutting temperature; can acquire the exact data. The disadvantage this method is the adaptability is worse than infrared camera method. The preparation is too complex for different machining process.

In the experiment, the steps of measuring cutting temperature with thermo-couple wire methods are as follow:

1. To wield the thermo-couple on the objectives this needs to be monitored.
2. To connect the thermo-couple wire with amplifier.

3. To record the dynamic cutting temperature of measuring point.

4. To analyze the dynamic cutting temperature with the recorded values.

In the study of face milling Ti6Al4V, Pittalà and Monno [43] applied the infrared camera to monitor the cutting temperature of the process. The experiment setup is shown in Figure 5.2. And the thermo-couple wire was applied in Lin's experiment as shown in Figure 5.3. It is obvious that the infrared camera method is more flexible than thermo-couple wire method.

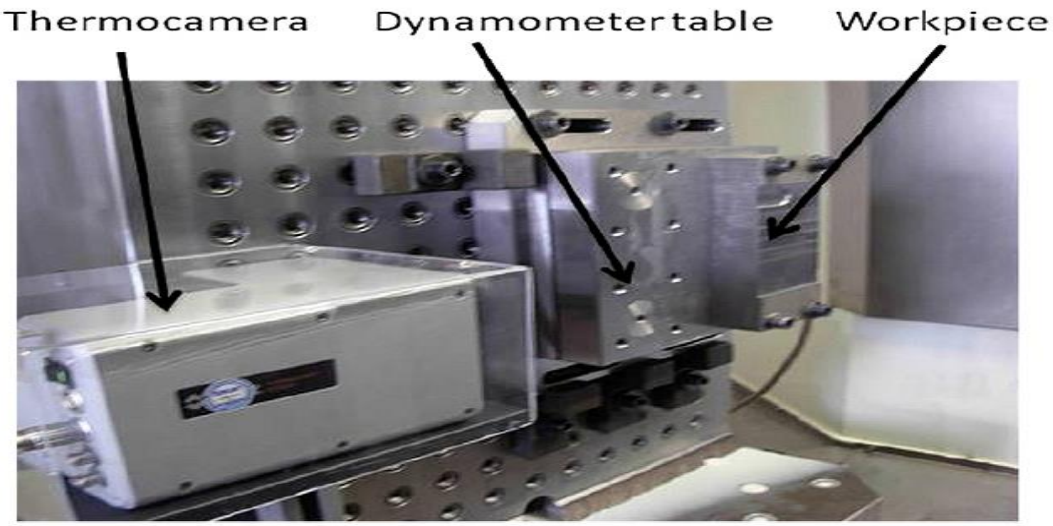

Figure 5.2 - Experimental setup for measuring cutting temperature with infrared camera [43].

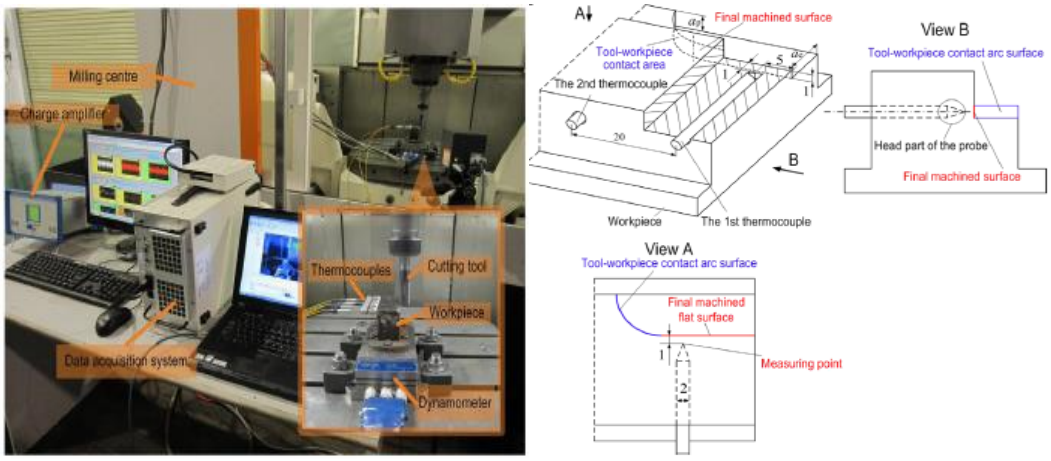

Figure 5.3 - The experimental setup by applying thermo-couple wire method [43].

5.1.6 The chemical reactions

The major chemical components of PCD compact are diamond, cobalt and WC. The chemical components of Ti6Al4V are shown in Table 5.1 [9]. The possible chemical reactions between PCD and Ti6Al4V are as follows:

1 The chemical reaction between Carbon and Titanium

Reaction conditions: 800°C ~ 2000°C

$$C + 2Ti \rightarrow Ti_2C \tag{C1}$$

Reaction conditions: 1500°C ~ 1700°C, to put the Ti into graphite with hydrogen flows

$$C + Ti \rightarrow TiC \tag{C2}$$

2 The chemical reaction between Oxygen and Titanium

Reaction conditions: 100°C ~ 1300°C, in air

$$\begin{cases} Ti + O_2 \rightarrow TiO_2 \\ 4Ti + 3O_2 \rightarrow 2Ti_2O_3 \\ 2Ti + O_2 \rightarrow 2TiO \end{cases} \tag{C3}$$

3 The chemical reaction between Aluminum and Titanium

Reaction conditions: > 583°C

$$\begin{cases} Ti + 3Al \rightarrow TiAl_3 \\ Ti + Al \rightarrow TiAl \\ 3Ti + Al \rightarrow Ti_3Al \\ 2Ti + 3Al \rightarrow Ti_2Al \\ Ti + 6Al \rightarrow TiAl6 \end{cases} \tag{C4}$$

4 The chemical reaction between Cobalt and Titanium

Reaction conditions: High temperature

$$\begin{cases} Ti + Co \rightarrow TiCo \\ 2Ti + Co \rightarrow Ti_2Co \\ Ti + 2Co \rightarrow TiCo_2 \end{cases} \tag{C5}$$

5 The chemical reaction between Tungsten and Oxygen

Reaction conditions: >400°C

$$\begin{cases} 2W + 3O_2 \rightarrow 2WO_3 \\ 8W + 11O_2 \rightarrow 2W_4O_{11} \end{cases} \tag{C6}$$

6 The chemical reaction between Tungsten and Carbon

Reaction conditions: >1400°C

$$\begin{cases} W + C \rightarrow WC \\ 2W + C \rightarrow W_2C \end{cases} \quad \text{(C7)}$$

7 The chemical reaction between Tungsten and Aluminum

Reaction conditions: >682°C

$$\begin{cases} W + 12Al \rightarrow WAl_{12} \\ W + 5Al \rightarrow WAl_5 \\ W + 4Al \rightarrow WAl_4 \\ W + 3Al \rightarrow WAl_3 \\ W + 2Al \rightarrow WAl_2 \\ 3W + 7Al \rightarrow W_3Al_7 \end{cases} \quad \text{(C8)}$$

8 The chemical reaction between Tungsten and Cobalt

Reaction conditions:

$$W + 3Co \rightarrow Co_3W \quad \text{(C9)}$$

9 The chemical reaction between Oxygen and Cobalt

Reaction conditions: ≈900°C

$$O_2 + 2Co \rightarrow 2CoO \quad \text{(C10)}$$

Reaction conditions: >300°C

$$\begin{cases} 3O_2 + 4Co \rightarrow 2Co_2O_3 \\ 2O_2 + 3Co \rightarrow Co_3O_4 \end{cases} \quad \text{(C11)}$$

10 The chemical reaction between Aluminum and Cobalt

Reaction conditions: >1400°C, in vacuum or inert gases

$$\begin{cases} Co + Al \rightarrow CoAl \\ 2Co + 5Al \rightarrow Co_2Al_5 \\ 3Co + 13Al \rightarrow Co_3Al_{13} \end{cases} \quad \text{(C12)}$$

Table 5.1 Chemical composition of Ti-6%Al-4%V

Contents	Al	V	Fe	O	C	H	N	Y	Ti
Composition (wt %)	5.5	3.5	0.3	0.14	0.08	0.01	0.03	50ppm	Balance

5.2 Dynamic cutting temperature

5.2.1 Model of dynamic cutting temperature

As illustrated in Figure 5.4 (a), it can be assumed that the cutting temperature at one fixed point in the cutting zone is caused by two heat sources from the shearing plane and the flank plane. According to Lin et al. [3], the temperature rise caused by each individual heat source at a fixed point M can be expressed by Equation (5-5).

$$\theta_i = \frac{Q_i}{8c\rho\sqrt{\pi\alpha\tau}} e^{\frac{-y_i^2}{4\alpha\tau}} (erf(\frac{x_i}{\sqrt{4\alpha\tau}}) - erf(\frac{x_i - W}{\sqrt{4\alpha\tau}})(erf(\frac{z_i}{\sqrt{4\alpha\tau}}) - erf(\frac{z_i - L}{\sqrt{4\alpha\tau}})), i = s, f \tag{5-5}$$

Where: c, ρ, W, L, α and τ are specific heat capacity, density, length and width of rectangular heat source, thermal diffusivity and time in actual milling process; s and f indicate shear plane and friction plane of the tool - chip interface as illustrated in Figure 5.4 (a). And the location of M in the local shearing and friction coordinate systems can be described as (x_s,y_s,z_s) and (x_f,y_f,z_f). Therefore, Equation (5-5) can be simplified to Equation (5-6).

$$\theta_i = K_i(x, y, z, \tau)Q_i, i = s, f \tag{5-6}$$

Where K=HJ, and the expression of H and J are as in Equation (5-7).

$$\begin{cases} H_i = \dfrac{e^{\frac{-y_i^2}{4\alpha\tau}}}{8c\rho\sqrt{\pi\alpha\tau}}, i = s, f \\ J_i = (erf(\dfrac{x_i}{\sqrt{4\alpha\tau}}) - erf(\dfrac{x_i - W}{\sqrt{4\alpha\tau}})(erf(\dfrac{z_i}{\sqrt{4\alpha\tau}}) - erf(\dfrac{z_i - L}{\sqrt{4\alpha\tau}})), i = s, f \end{cases} \tag{5-7}$$

To discuss the value of K_i, four assumptions were made in the calculation:

- The measuring point is at the same location in each milling cycle and the area of heat source remains the same value. Therefore, the coordination should be of the same value, i.e., the values of (x_s,y_s,z_s) and (x_f,y_f,z_f) are constant.
- The measuring time is the same in each milling test, namely, the value of τ is constant.
- The thermal parameters of the workpiece are constant.
- W and L equal to the values of feed per tooth and the axial cutting depth.

According to assumptions 1 - 4, the value of H is constant. However, J is still variable when

machining parameters are changed. Because the temperature measured in this experiment is considered to be the average cutting temperature, the location of measuring point P can be an arbitrary point anywhere on the surface of the chip. Therefore, it can be assumed that $x_s=x_f$, $y_s=y_f$, $z_s=z_f$. According to the experimental measurement of Tests 9 - 22, the location of point M in the friction heat source coordinate system can be defined as x_f=0.01mm, y_f= 0.2mm, z_f= 0.1mm and the processing time τ for one milling cycle is 3ms. By substituting this location, machining parameters and material parameters into the expression of J, it can be found that the range of J with different feed and depth of cut is from 0.003 - 0.03.

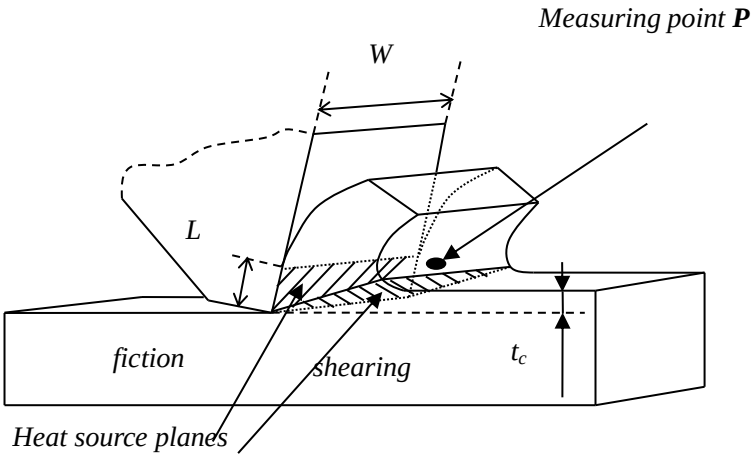

(a)

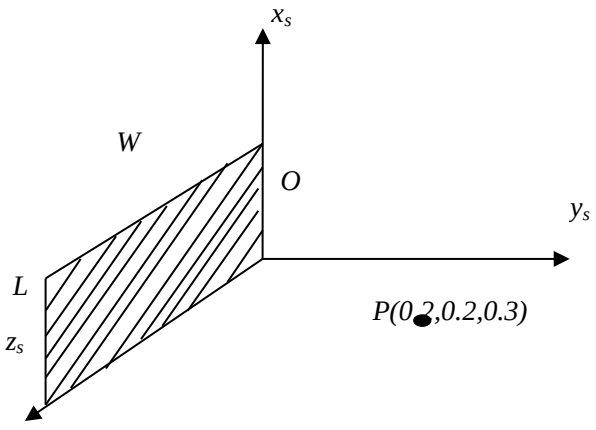

(b)

Figure 5.4 - The illustration of rectangle heat source and the position of measuring point (a) The position of heat source and measuring point on machining system (b) The assumed position of measuring point in friction plane coordinate system.

It is obvious that heat source Q is also an important factor which can determine the value of the temperature and it is proportional to the cutting temperature. Many models have been developed by different researchers to describe the cutting heat source. For example, Cui et al. [46] introduced the polynomial form of heat source in their model based on the least-squares method. However, the polynomial form cannot exactly reflect the principle of heat generation. Theoretically the heat source consists of two essential elements: the heat generated by shearing and the heat generated by friction. According to Abukhshim et al. [101], these two parts of heat can be described as Equation (5-8).

$$Q_i(v, f_t, a_p) = F_i(v, f_t, a_p)v\tau, i = s, f \tag{5-8}$$

Then, the cutting temperature can be rewritten as Equation (5-9).

$$\theta_i = HJ_iF_iv\tau \tag{5-9}$$

It is known that changes of v, ft and ap will result in a variation of the peak values of cutting forces. According to Anayet et al. [102], the empirical function of cutting force can be expressed as Equation (5-10).

$$F = Av^{m_1} f_t^{m_2} a_p^{m_3} \tag{5-10}$$

It is obvious that cutting force has an exponential relationship with machining parameters. And the variation of machining parameters will finally lead to the change of the average cutting temperature. By considering the sources of the cutting heat, the relationship between cutting parameters and the average temperature at point M is proposed as Equation (5-11) according to Equation (5-8) - Equation (5-10):

$$\theta_e = \theta_s + \theta_f = R_s v^{\alpha_1} f_t^{\alpha_2} a_p^{\alpha_3} + R_f v^{\alpha_4} f_t^{\alpha_5} a_p^{\alpha_6} \tag{5-11}$$

Where α_1, α_2, α_3, α_4, α_5 and α_6 are empirical constants. R_s and R_f are two functions of K_1 and K_2 which can be expressed as Equation (5-12).

$$R_i = C_iK_i, i = s, f \tag{5-12}$$

Where C_i (i=s, f) is a constant in the equation. And the values of Rs and Rf can be assumed as the function which is determined by the value of J_i (i=s,f). By substituting the experimental data of cutting temperature and corresponding machining parameters into Equation (5-11), the values

of these parameters can be calculated.

5.2.2 Experimental validation

The cutting experiments were carried out on a 4-axis HAAS milling machine. The cutting force signal was collected through an 8-channel dynamometer (Kistler 5070) installed underneath the workpiece. The coupler used was a 6-channel charge amplifier (Kistler 5070). The force single was recorded via a DAQ card (National Instrument model 9257). The setup of the experimental system was illustrated in Figure 5.5 (a). To simplify the analysis of relevant factors, the tool paths applied were straight lines along the edge of the workpiece. The FLIR Infrared Camera was fixed in the position shown in Figure 5.5 (b). Twenty two cutting tests were carried out. The detailed cutting parameters are listed in Table 4.4. The room temperature is around 25℃

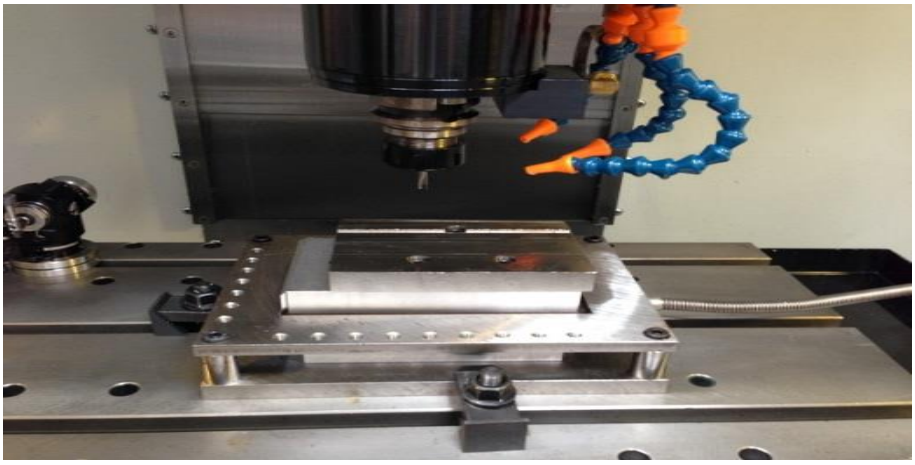

(a)

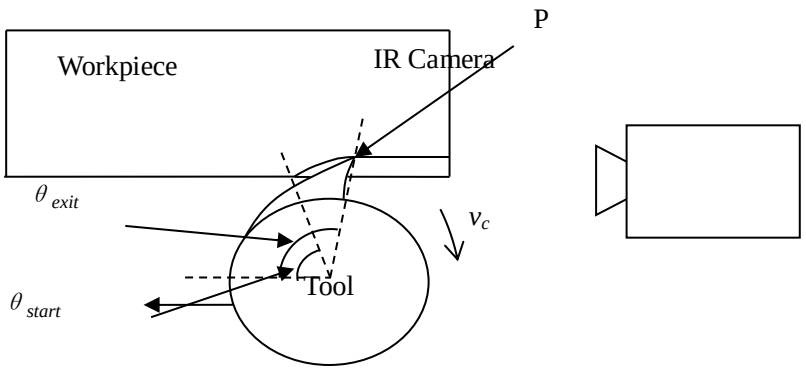

(b)

Figure 5.5 - Experimental system setup (a) the instantaneous cutting force monitoring system (b) the thermal monitoring system.

Cutting temperature is an important factor that affects cutting forces. High cutting temperature may soften the workpiece material and lead to a decrease of the cutting force. The cutting temperature at the cutting edge is dynamically changing in the cutting process and it is unevenly distributed along the cutting edge of the tool. However, due to the complexity of the rotating cutting tool and the disturbance of splashing coolant, it is impossible to accurately measure the cutting temperature at the cutting edge in real-time in the milling process. In practice it is more important to find out the relationship between cutting temperature in the cutting zone and cutting parameters and material behavior in the milling process, although the temperature obtained may not be the exact real-time temperature on the cutting edges.

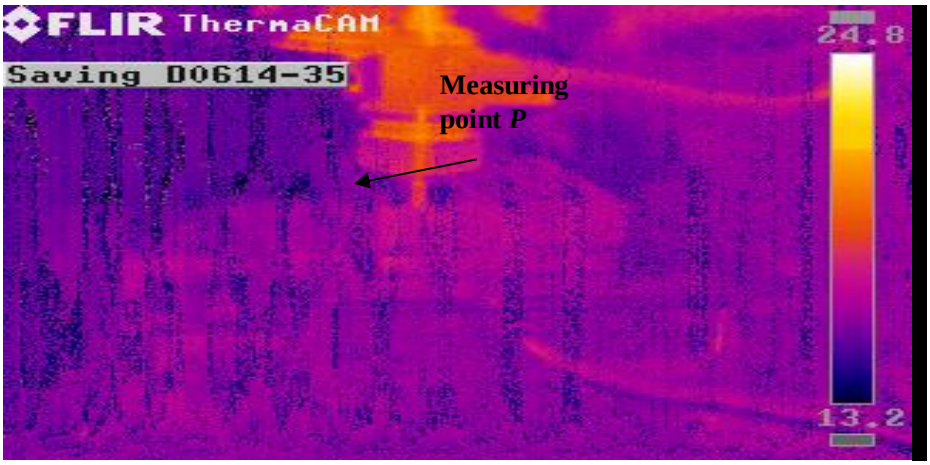

(a)

(b)

Figure 5.6 - Thermal images of milling process (a) the image before cutting (b) the thermal image of Test 13.

To investigate the relationship between machining parameters and the cutting temperature, the temperature measuring system shown in Figure 5.5 (b) was setup. Point P is the measuring point which is located in the cutting zone of tool. It is assumed that the temperature measured on point P represent the average cutting temperature in the cutting zone. The infrared image of the static milling system is shown in Figure 5.6 (a). Figure 5.6 (b) illustrates the infrared image captured in Test 13. It can be seen that the measuring point (P) is the average cutting temperature of cutting zone in the milling process as shown in Figure 5.6.

5.2.3 Prediction and Analysis

The parameters of the cutting temperature model are listed in Table 5.2.

Table 5.2 Parameters

Parameters Name	Values	Parameters Name	Values
α_1	-1.5490	α_4	1.7052
α_2	-0.6144	α_5	0.6273
α_3	0.1600	α_6	0.1600
R_5	40235.4520/J_5	R_6	0.0996/J_6

The comparison of predicted cutting temperature and the experimental results are shown in Figure 5.7, Figure 5.8 and Figure 5.9 It can be seen in these Figures that the predicted cutting temperatures are reasonably accurate. In Figure 5.7 the results from calculation match the experimental results at accuracy of up to 99.5% when the axial cutting depth is between 0.4 - 0.6 mm.

Figure 5.7 illustrates the predicted average temperature at point P and the actual temperature at the same location with various cutting speeds. The experimental data was collected in Tests 1 - 8 with the machining parameters listed in Table 4.4. The increase of cutting speed in the milling tests directly led to the rise of cutting temperature. The range of cutting temperature was found to be between 137 ^{o}C to 220 ^{o}C. Through generating more heat in the milling process, both shearing and friction

contributed to the increase in temperature caused by higher cutting speed. Due to the poor thermal conductivity of Ti6Al4V, there was a significant increase in the average temperature at point P at the final stage.

Similar experiments have been conducted by some other researchers as well. For example, Rao et al. [28] found that the temperature increased with an increase of cutting speeds when the applied cutting speed was lower than 150 m/min, but the temperature dropped when the cutting speed was higher. The small difference between their results and our findings was caused by the different thermal conductivity of different tool materials. In the experiments of Rao et al. [28], WC rather than diamond cutting tools were applied. The thermal conductivity of PCD is about five times higher than that of WC. Therefore, the temperatures measured in our experiments were lower than those obtained with WC tools.

To investigate the effect of axial cutting depth on cutting temperature, six cutting tests (Tests 9 - 14) were carried out in the same milling system. The results are plotted in Figure 5.8. Because the increase of axial cutting depth causes the increase of contact area between PCD tool and Ti6Al4V, which results in the generation of more heat, it can be seen in Figure 5.7 that the temperature raises from 100 ^{o}C to nearly 200 ^{o}C.

The thermal effects of feed are shown in Figure 5.9. The data is the results of Tests 15 - 22. Similar to the effect of increasing axial cutting depth, by applying larger feed, the interface area of front tool cutting plane and workpiece increased and this led to the rise of cutting temperature.

The 3-dimensional image of the PCD insert in Figure 5.10 was taken by using the Alicona Microscope. It can be seen in the image that the flank of the PCD tool was damaged by abrasive wear which was caused by the serious friction during the machining process. Such great change of flank wear had not been found in Tests 9 - 14. It is possible that the damage at the flank of the tool was caused by the Built-Up-Edge (B.U.E) and chipping. Then, the irregular surface of worn flank would

result in the generation of more heat at the later stage as illustration in Figure 5.11. Therefore, it can be concluded that the flank of the tool is more prone to damage with an increase of feed, and the average cutting temperature would rise due to the additional heat generated by the damaged surface.

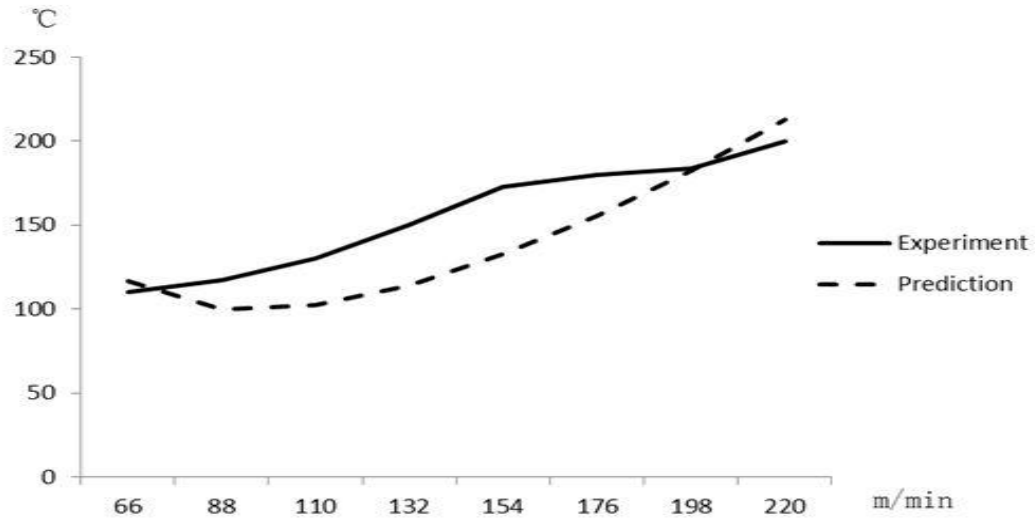

Figure 5.7 - The thermal effect of changing cutting speed (V_c).

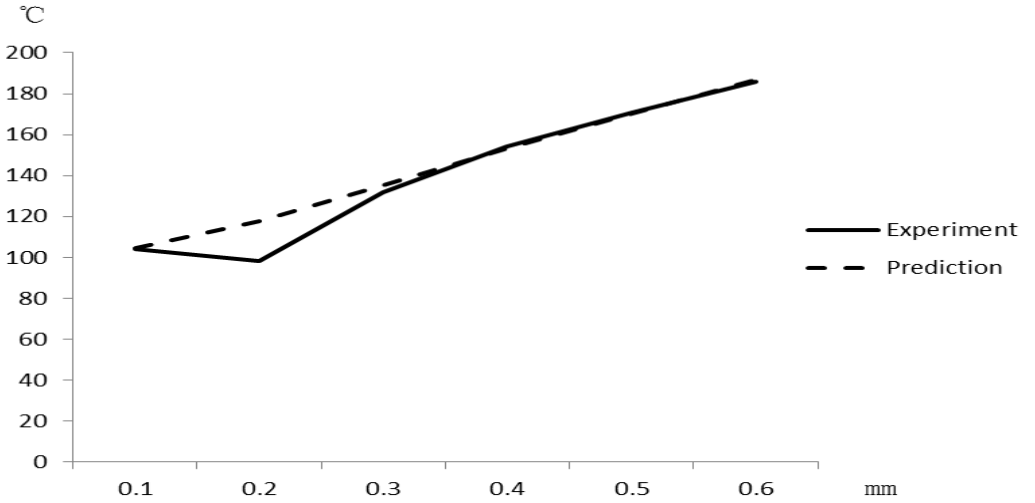

Figure 5.8 - The thermal effect of changing axial cutting depth (ap).

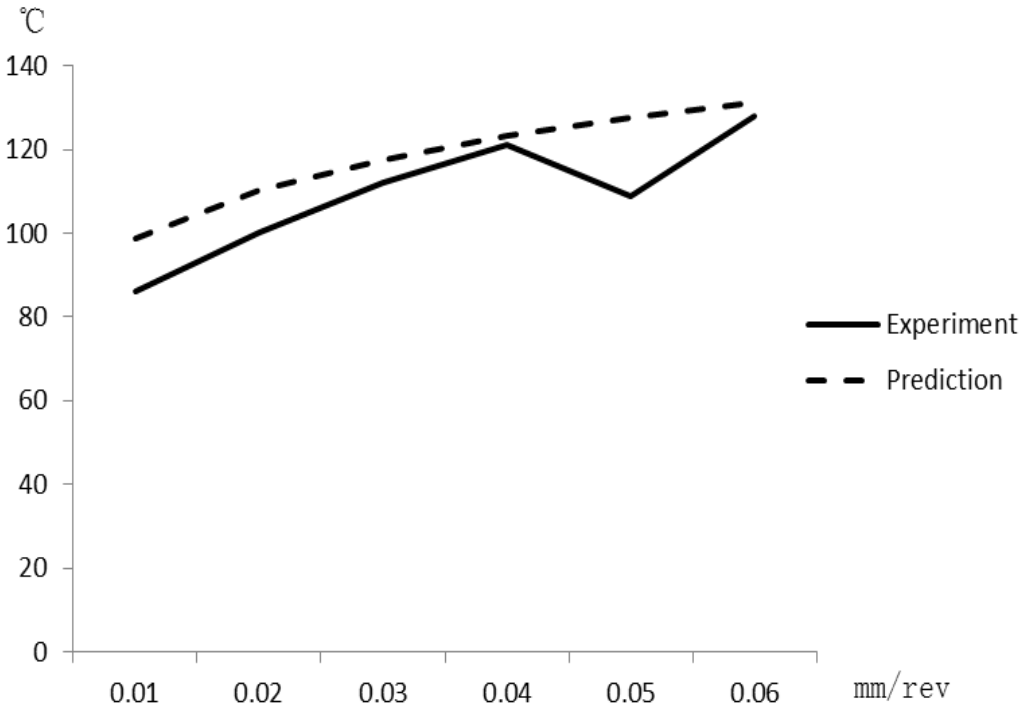

Figure 5.9 - The thermal effect of changing feed (f_t).

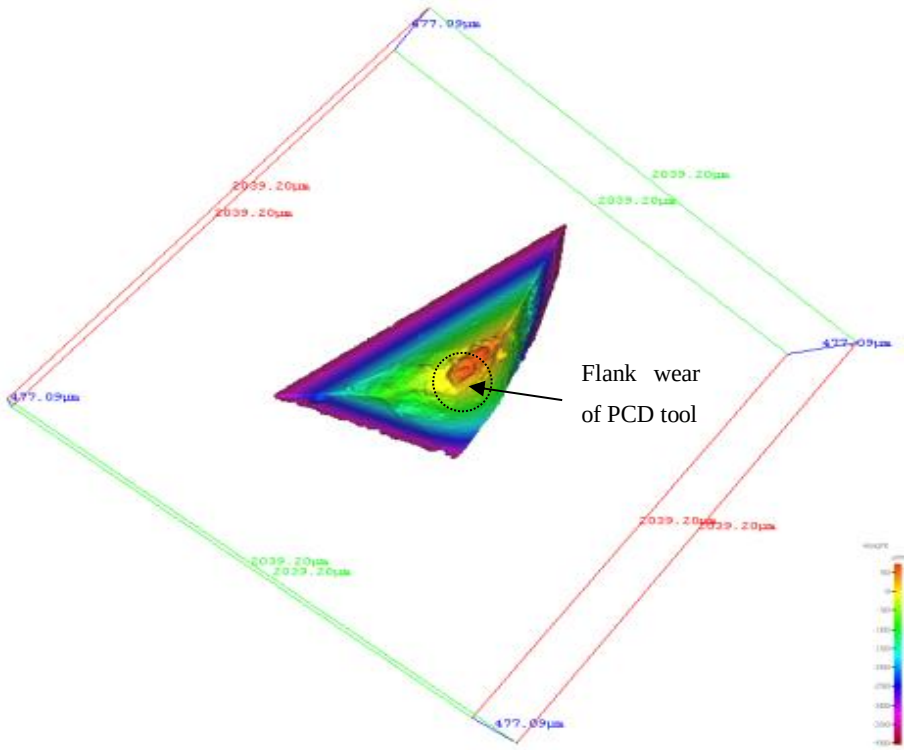

Figure 5.10 - The abrasive damage on flank of PCD tool.

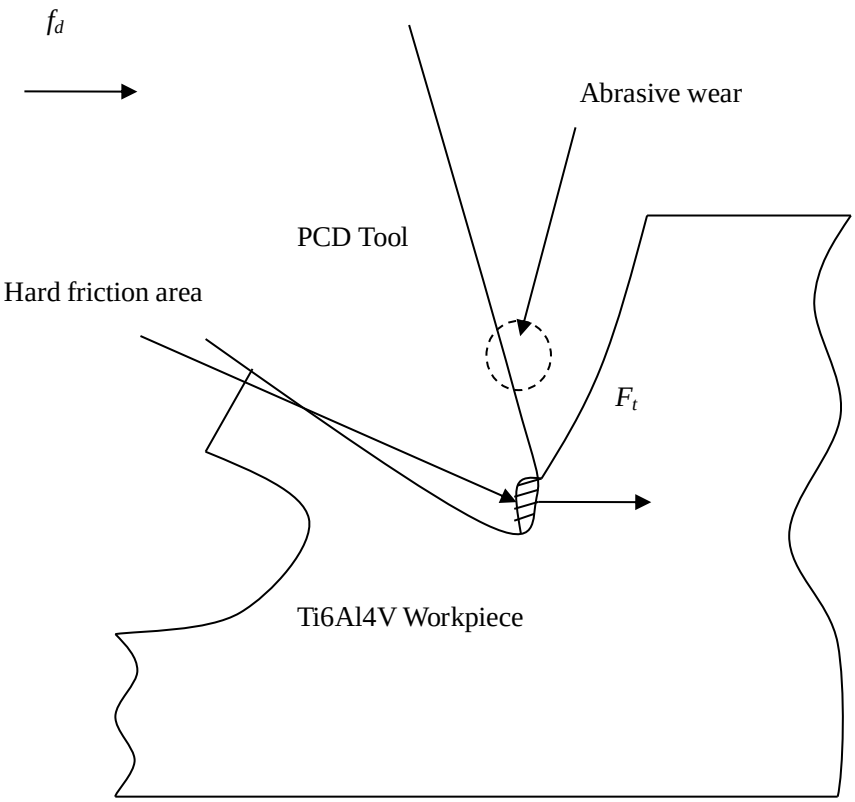

Figure 5.11 - The illustration of friction area on tool flank.

5.3 Residual chemical components on the PCD tool

5.3.1 The study of temperature distribution on tool nose

To illustrate the distribution of the temperature on the cutting tool in addition to the average temperature in the cutting zone, a three-dimensional FEA model (Figure 5.12 (a)) was developed by using the same machining parameters and cutting tool as applied in Test 14, and residual chemical components on the PCD tool were examined to find out if chemical reactions have taken place.

The Johnson-Cook constitutive equation (Eq. (5-13)) was used to describe the material behavior of Ti6Al4V. According to Umbrello [103], the material parameters A, B, n, C, m and the friction coefficient are listed in Table 5.3. It can be seen that the highest temperature in Figure 5.12 (b), which is close to 500 K (227^{o}C) is higher than the average cutting temperature measured in Test 14. Because the temperature measured in the cutting region is the averaged cutting temperature, theoretically it should be lower than the temperature at the cutting edge.

$$\sigma = [A + B(\varepsilon_p)^n][1 + C\ln(\frac{\dot{\varepsilon}_p}{\varepsilon_0})][1 - (\frac{T - T_r}{T_m - T_r})^m] \quad (5\text{-}13)$$

Table 5.3 Johnson-Cook parameters of Ti6Al4V

A	B	C	n	m	μ
1070MPa	*845MPa*	0.025	0.58	0.75383	0.67
A1	*A2*	A3	A4	A5	
0.0395	*1.0072*	1.9234	0.014	3.87	

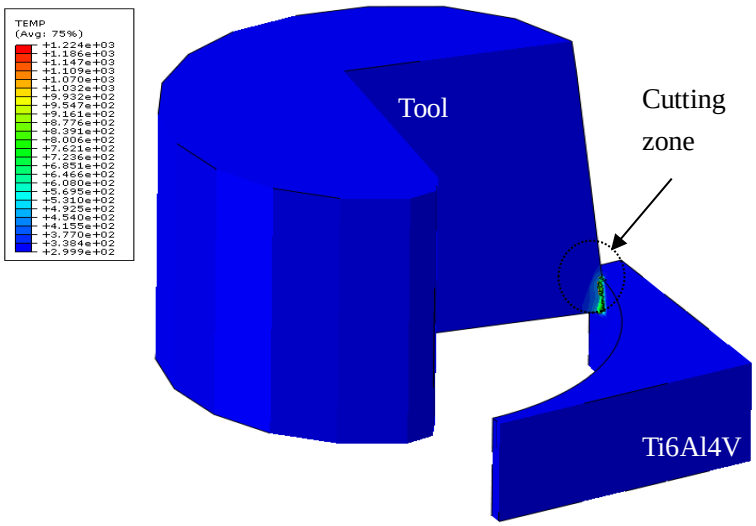

(a)

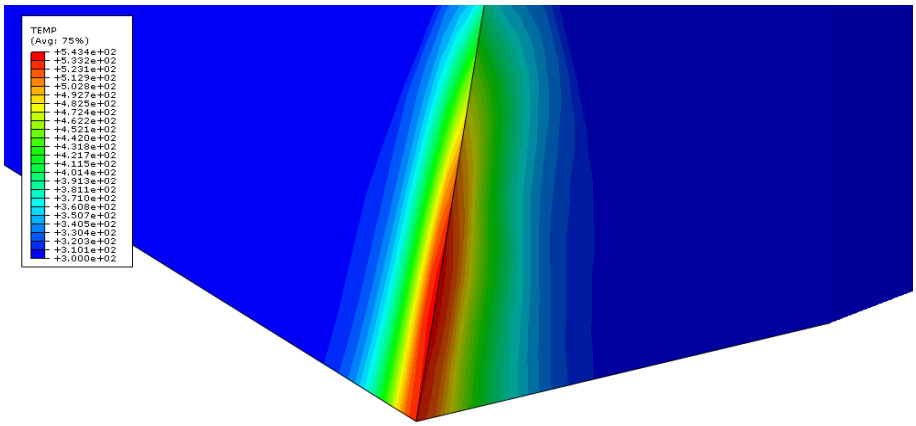

(b)

Figure 5.12 - The FEM result of milling process (a) the 3D milling model of Test 14 (b) the average cutting temperature nephogram of cutter.

5.3.2 The analysis of XRD results

Four PCD tools were examined with the XRD method to analysis the chemical components remaining on the tool surface. These tools were brand new before they were used in the experiments. The average machining time in each test was 3 mins. Figure 5.13 (a) and Figure 5.13 (b) show the XRD results of Tool 1 and Tool 2 which were used in Test 1 and Test 8, respectively. Machining parameters for these eight tests were listed in Table 4.4. The cutting temperature in Test 8 was higher than that in Test 1 due to the higher cutting speed applied. The chemical components remaining on Tool 1 were found to be the original materials: Tungsten Carbide (WC), Carbon (Diamond) and Cobalt (Co). More chemical elements such as TiC and W_2C were detected on the surface of Tool 2. Theoretically these materials can only be formed in chemical reactions at elevated temperature of up to 500 ^oC or higher. Therefore, it can be concluded that when the high cutting speed was applied in the milling process, the local temperature on the edge of the PCD cutter was high enough to initiate these chemical reactions.

Figure 5.13 (c) and Figure 5.13 (d) are the XRD results of PCD Tool 3 and Tool 4 which were applied in Test 9 and Test 14. Compared to Test 14, a smaller axial cutting depth was used in Test 9 while the other machining parameters remained the same. According to previous results, the increase of axial cutting depth can cause a rise of cutting temperature. The cutting temperature in Test 14 would have been higher than that in Test 9. From Figure 5.13 (d), it can be seen that chemical reaction did occur in Test 14, new material TiO_2 and WO_3 were found on the PCD surface of Tool 4.

However, the examination on PCD Tool 3 (Figure 5.13 (c)) shows no new components, which indicates that no chemical reactions occurred in Test 9 and the cutting temperature was low. PCD tool applied in Test 9 was found to have

remained in good condition.

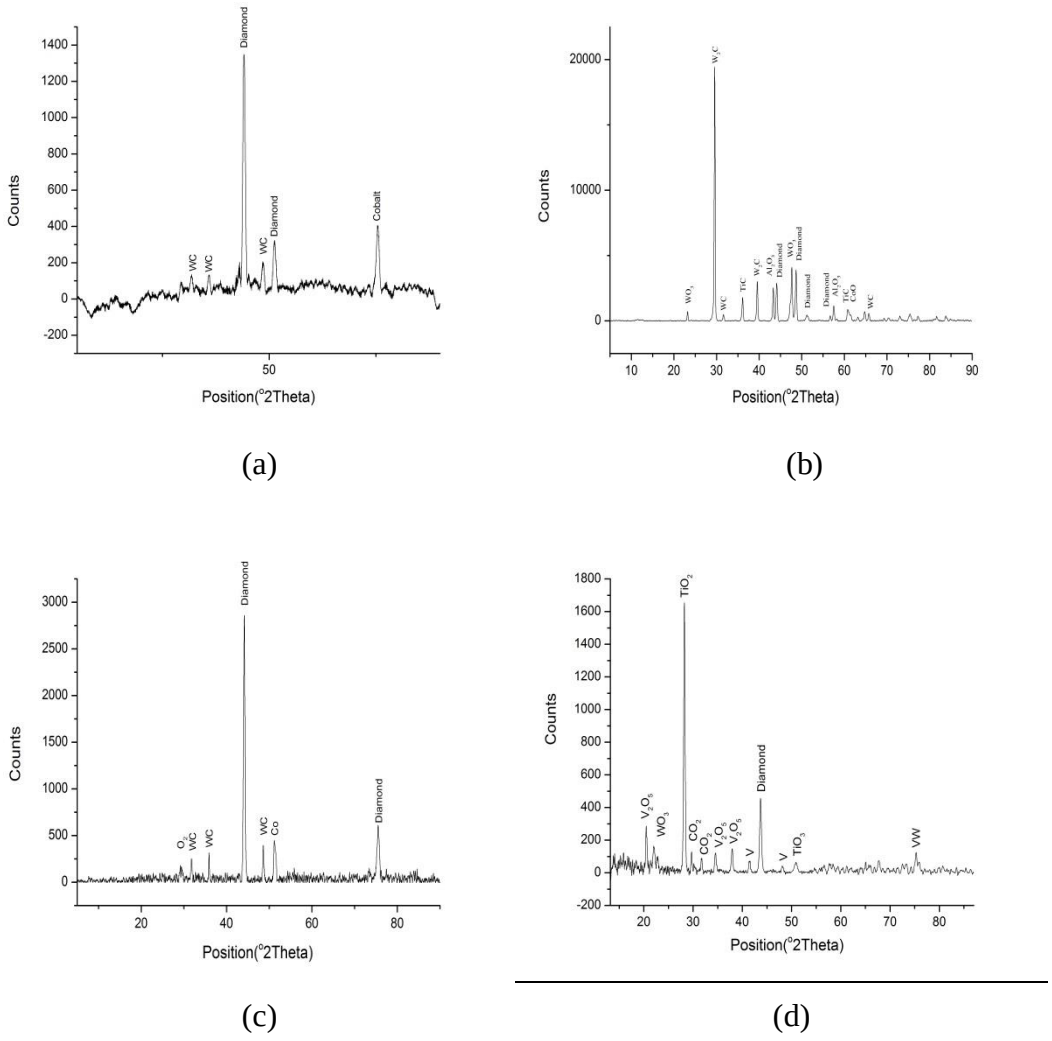

Figure 5.13 - 4 XRD results of used PCD tools (a) PCD tool used in Test 1 (b)PCD tool used in Test 8 (c)PCD tool used in Test 9 (d) PCD tool used in Test 14.

5.4 Summary

This chapter investigated the thermal characteristics in milling Ti6Al4V with PCD tools which include average cutting temperature, chemical components and chip morphology. A predictive model was developed and validated to calculate cutting temperature of PCD tools to investigate the relationship between the temperature and machining parameters. By defining the measuring point, the cutting temperature can be monitored experimentally with the Infrared Camera device. Experimental results show that the temperature increased with increase to v_c, f_t and a_p. Results from the model match the data measured in the cutting experiments.

Chemical analysis was performed by using the XRD method to check residual material on the PCD tools. New chemical components such as TiC and TiO_2 were detected on some PCD tools and indicated that the cutting temperatures were higher than 500^oC in these cutting tests.

6 Tool wear and failure

This chapter investigates tool wear in the end milling of Ti6Al4V with PCD tools. It includes three aspects: the initiation of cracking, tool life investigation and fractograph analysis. According to the analysis of SEM photos, the chipping and delamination were found to be the major wear forms. By simulating the milling process with FEM method, the results show that stress concentration and shearing can be the possible reasons for initiating the cracking on cutting edge of PCD tools. Besides, the tool life test investigates the time of chipping initiation and tool wear evolution.

6.1 Introduction

6.1.1 Criterion of tool failure

Tool wear analysis, as well as the study of cutting force and cutting temperature, is the most important aspects for selection and application of new tool material. To understand the tool wear characteristics is important for the practical applications. The catastrophic tool wear can cause unacceptable quality of surface finish. According to ISO 8688 -1 and ISO 8688 -2 [104], namely, tool life testing in face milling and end milling, the types of tool wear include: Flank wear (VB), Face wear (KT), Chipping (CH), Cracks (CR), Flaking (FL), Plastic Deformation (PD) and Catastrophic Failure (CF). The tool wear criterions of different wear forms are shown in Table 6.1. The flooding is used as the cooling method in the process. In Table 6.1, the meanings of the three characters need to be mentioned:

N (Normal):

To select the values of tool wear criterion by considering a reasonable compromise between reliability, costs of testing and normal deterioration intensity.

L (Large):

To select the values of tool wear criterion without probiting the cost of higher material consumption and and the tool can be used until final destruction.

S (Small)

To select the values when the costs of material consumption is very high.

Table 6.1 The criterion of tool wear [111]

Code	Description of tool deterioration					
Basic form Distribution Subdivision	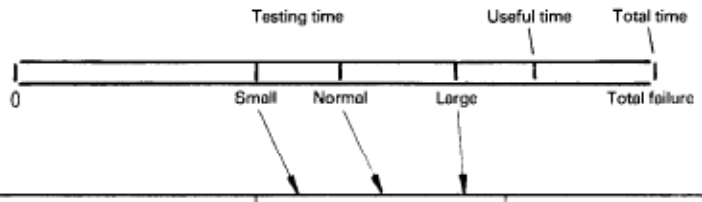					
	Tool deterioration phenomena		Criteria, mm S	N	L	Illustration
VB	**Flank wear**					
1	Uniform		0,2	0,35	0,5	
2	Non-uniform		0,9	1,2	1,5	
3	Localized		0,8	1	1,2	
KT	**Face wear**					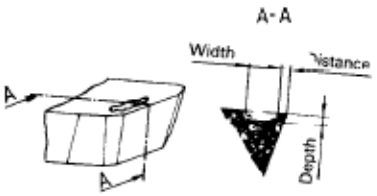
1	Crater wear :	Depth	0,05	0,1	0,15	
		Width*	.....	.....	.....	
		Distance*	.....	.....	.....	
2	Stair forms :	Depth	0,25	0,3	0,35	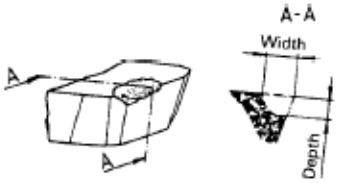
		Depth/width*	.....	.....	.....	
CH	**Chipping** (breakage)					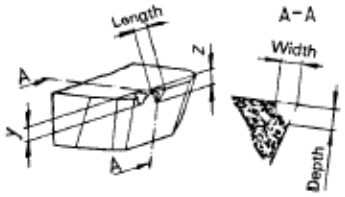
1	Uniform		For y or z with corresponding length values			
2	Non-uniform					
3	Localized					
		Length, mm				
A	Micro-chipping	< 0,3	0,2	0,25	0,3	
B	Macro-chipping	0,3 to 1	0,25	0,4	0,5	
C	Breakage	> 1	–	–	–	

Code	Description of tool deterioration		
Basic form Distribution Subdivis on	Tool deterioration phenomena	Criteria, mm S N L	Illustration
CR 1 2 3	Cracks Cracks perpendicular to the edge Cracks parallel to the edge Irregular direction	The number of the largest cracks and the mean distance between them shall be recorded	
FL	Flaking	Could be used as criteria in exceptional cases	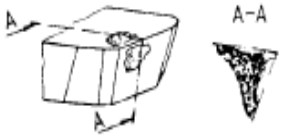
PD	Plastic deformation		
CF	Catastrophic failure		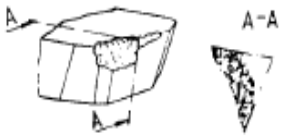

6.1.2 The failure of brittle material

PCD is the material sintered diamond particles with WC-Co substrate in the high pressure and high temperature process. There are two different chemical bonds of PCD: the Covalent bonds between diamond particles (D-D) and the Ionic between metal materials and diamond particles (D-M-D) [105]. The increasing tendency of brittle fracture is shown in Figure 6.1.

Metallic **Ionic** **Covalent**

Increasing tendency for brittle fracture

Figure 6.1 - The increasing tendency for brittle fracture [106].

Therefore, it is reasonable to believe that PCD compacts can show the significant

brittleness because there are a lot of Ionic and Covalent chemical bonds. The failure forms of brittle material include:

Cleavage - crack extension occurs by breaking of bonds across an atomic plane. Figure 6.2 shows the crack propagation of material with the form of cleavage. The major characteristics of cleavage fracture are:

1. Transgranular.
2. Low-energy fracture.
3. Low capacity of plastic deformation.
4. The crack tip stress is normally lower than the theoretical fracture stress.

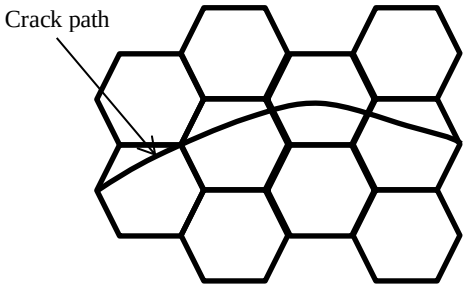

Figure 6.2 - The crack propagates in the form of cleavage [106].

Intergranular fracture - this is low toughness and low ductility fracture mode. The reasons for this type of fracture mode are weakness of grain boundaries, the brittle phase or impurity at the grain boundary, the excessive treatment with hydrogen or intergranular corrosion. Figure 6.3 shows the crack propagation with the form of intergranular fracture.

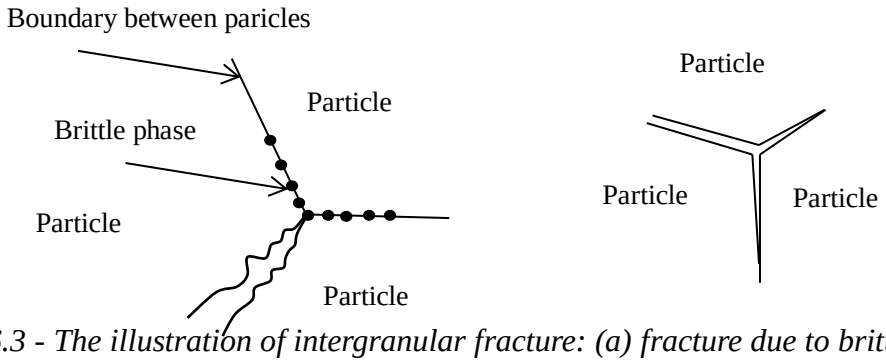

Figure 6.3 - The illustration of intergranular fracture: (a) fracture due to brittle phase at the boundary; (b) fracture due to the strong inner structural strength in particles [106].

Crazing - the initiation of this mode is similar to cracking. In the case of ploymers, when the temperature is lower than glass temperature, the material can fail with Crazing.

6.1.3 Relevant calculations

According to Groover [87], the tool life can be predicted with the Taylor's equation

$$vT_t^n = C \tag{6-1}$$

Where v is cutting speed (m/min); T_t is tool life (min); n and C are constants.

This empirical expression of tool life summarizes the relationship between cutting speed and tool life. However, the linear relation is not available for many situation of tool application. For the conventional process, the tool life can be determined by some factors such as, type of process (e.g. milling, drilling, turning, etc.), the material properties of the cutting tool and material of the workpiece, the cooling condition in the process and the machining parameters applied.

Another expression of determining tool wear is

$$W = \frac{K}{3}\frac{FL}{H} \tag{6-2}$$

Where W, K, F, L and H are the volumetric wear of the material, Archard wear coefficient, the contact force, cutting length and the hardness of softest material. And the contacting force expression is provided by Iliescu as Equation (6-3). [107]

$$F_a = Kf^{\alpha}v^{\beta}g(W) \tag{6-3}$$

Where K_c, α, β are calculating parameters for the expression; f and v are feed and cutting speed. The $g(W)$ is the function of the tool wear.

From equation (6-2) and (6-3), it can be induced that the feed and cutting speed have the exponential relationship with the tool wear.

A new tool wear model proposed by Hao et al. [108]as Equation (6-4).

$$h_o = CK\frac{pvt}{\sigma_f} \tag{6-4}$$

Where C and K are empirical constants; p, v and t are normal load, cutting speed and cutting time. And the fraction intension of the WC tool is

$$\sigma_f = 371 + \left(\frac{1766}{1+e^{(\theta-788)/54}}\right) \tag{6-5}$$

The Equation (6-3) and (6-4) describe the relationship between machining parameters and tool wear. The Equation (6-3) uses the exponential function form to estimate the tool wear. And the Equation (6-4) describes the linear relationship. Due to the complexity of PCD failure evolution in this experiment, these models cannot agree well with the experimental result.

In this study, the Taylor's equation has been modified based on the experimental

results. The influence of feed is more significant than cutting speed. Therefore, the Taylor's Equation can be rewritten as Equation (6-6).

$$fT_t^n = C \tag{6-6}$$

And the calculation parameters were obtained by substituting the data of tool wear and corresponding time values.

6.1.4 Measurement method

There are two main methods for measuring tool wear in modern industry: Scanning Electrical Microscope and optical microscope. For this study, the Philips XL 30 SEM and Alicona optical microscope are used for examining the used PCD tools.

According to the Alicona's manual, the measuring parameters are shown in Figure 6.4. "a" represents the distance from the point where the profile path leaves the straight line up to the point where "a" subtends "b". And "b" is the length from the point where the profile path leaves the straight line up to the point where "b" subtends "a". "a" is the value applied for evaluating the tool wear.

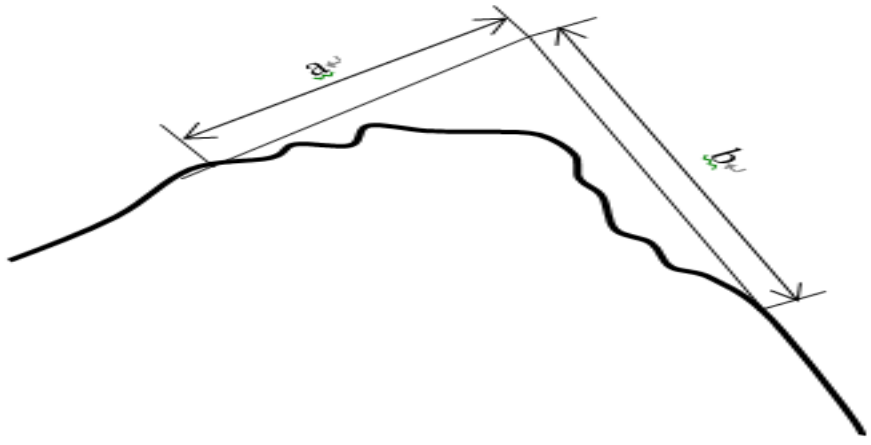

Figure 6.4 - The measuring parameters on tool nose.

6.1.5 The structure and objectives

To study the PCD tool wear in endmilling Ti6Al4V process, there are three aspects

involved:

- The analysis of cracking initiation in the process;
- The analysis of tool wear evolution;
- The analysis of tool fractographs.

And the structure outline is shown in Figure 6.5.

For the first aspect, the study of tool wear initiation is performed based on the observation of PCD SEM scanning results and the FEM simulation with Abaqus software. According to the summary of the PCD tool wear at the early stage of process, the crater wear and chipping occurred at the cutting edge. The FEM model is setup by applying the cutting force obtained from experiment. And the material failure analysis of FEM uses extended finite element method (XFEM) technology to simulate the situation of shearing damage and stress concentration of notched section.

The second aspect focuses on the study of tool wear evolution. The used PCD tools were examined by Alicona optical microscope. By analyzing the measurement of PCD tool wear in different cutting length, the tool wear evolution relation curve is summarized. The investigation of tool wear fractographs is performed based on the observation of PCD SEM scanning results.

The objectives of PCD tool wear analysis are set to:

1. Find out the reason of tool wear initiation.
2. Setup the relationship curve of tool life.
3. Identify the characteristics of brittle fracture.

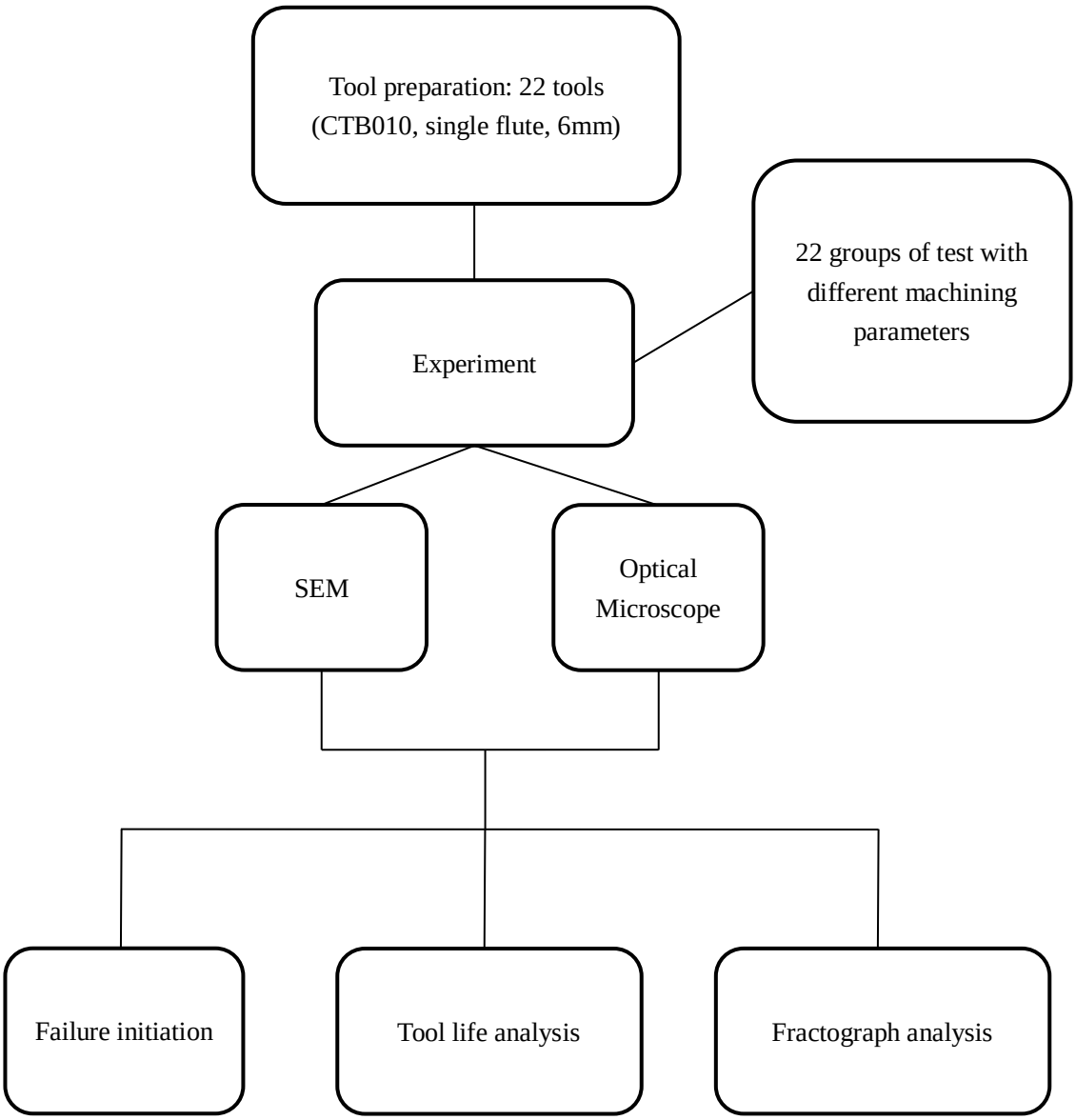

Figure 6.5 - The structure of tool wear analysis.

6.2 Experiment setup

The cutting experiments were carried out on a 4-axis HAAS milling machine. Signals of cutting force were collected through an 8-channel dynamometer (Kistler 9257B) installed underneath the workpiece. The coupler used was a 6-channel charge amplifier (Kistler 5070). The force signal was recorded via DAQ card (6036E, National Instrument). The setup of the experimental system is illustrated in Figure 6.6 (a). Furthermore, the tool wear evaluation method is illustrated as Figure 6.6 (b). By measuring the value of T_t, the evolution of tool wear can be investigated. To reduce the effects of noise factors, the tool paths used in the cutting tests were straight lines along the edge of the workpiece.

It is understood that three machining factors may affect the surface quality and machining efficiency: cutting speed, feedrate and axial cutting depth. In the experiment, a total of 31 tests were carried out and the cutting parameters applied in the experiment are listed in Table 6.2. The symbolic v, a_p and f are cutting speed, axial cutting depth and feed, respectively. To eliminate the effect of tool wear on cutting force and surface quality of workpiece, six new tools which had the same geometrical parameters and grain size were used in this experiment. The radial cutting depth is 3.5mm, flooding cooling was applied.

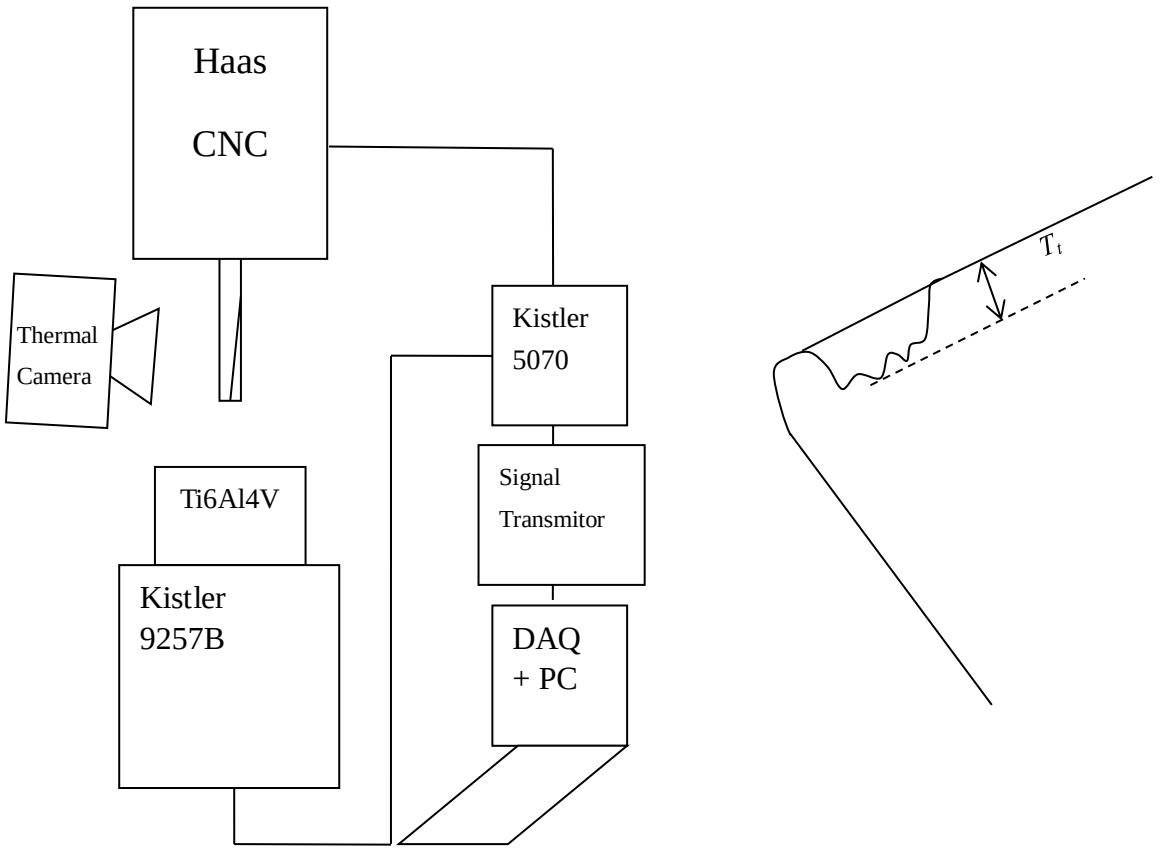

(a) Milling system setup *(b) Tool wear evaluation method*

Figure 6.6 - Milling system setup and tool wear evaluation method.

Table 6.2 Cutting parameters.

Tool Number	Test Number	Cutting speed Vc m(m/min)	Axial cutting depth ap (mm)	Feed fz(mm/rev)	Material removal rate (mm3/min)	Contact Area (mm2)
Tool 1	1	87.96	0.2	0.020	112	0.004
	2	87.96	0.4	0.025	280	0.010
	3	87.96	0.6	0.030	504	0.018
	4	131.95	0.2	0.016	140	0.003
	5	131.95	0.4	0.020	336	0.008
	6	131.95	0.6	0.013	327	0.007
Tool 2	7	175.93	0.2	0.015	168	0.003
	8	175.93	0.4	0.01	224	0.004
	9	175.93	0.6	0.012	420	0.007
Tool 3	10	65.97	0.2	0.025	105	0.005
	11	87.96	0.2	0.025	140	0.005
	12	109.95	0.2	0.025	175	0.005
	13	131.94	0.2	0.025	210	0.005
	14	153.93	0.2	0.025	245	0.005
	15	175.93	0.2	0.025	280	0.005
	16	197.92	0.2	0.025	315	0.005
	17	219.91	0.2	0.025	350	0.005
Tool 4	18	131.95	0.1	0.030	126	0.003
	19	131.95	0.2	0.030	252	0.006
	20	131.95	0.3	0.030	378	0.009
	21	131.95	0.4	0.030	504	0.012
	22	131.95	0.5	0.030	630	0.015
	23	131.95	0.6	0.030	756	0.018
Tool 5	24	131.95	0.2	0.010	84	0.002
	25	131.95	0.2	0.020	168	0.004
	26	131.95	0.2	0.030	252	0.006
	27	131.95	0.2	0.040	336	0.008
Tool 6	28	131.95	0.2	0.050	420	0.010
	29	131.95	0.2	0.060	504	0.012
	30	131.95	0.2	0.070	588	0.014
	31	131.95	0.2	0.080	672	0.016

6.3 Results and analysis

6.3.1 Shearing damage

The shaded area in Figure 6.7 (a) indicates the contact area between PCD cutting tool insert and Ti6Al4V workpiece. In each milling cycle, shearing occurrs on the boundary of the contact region. As calculated in Table 6.3, the range of pressure on the PCD is from 3419.20 N/mm2 to 7861.53 N/mm2 (i.e. from 3.4 GPa to 7.86 GPa). Among the first nine tests, the pressures in Test 1 and Test 7 are significantly greater than the others. When the PCD inserts were periodically loaded under these pressures, brittle cracks could be initiated on the shear plane and progressively resulted in tool failure in the milling cycles.

Table 6.3 Cutting Forces (Unit: N).

Test Number	Fx	Fy	Fz	Resultant force (F)	Pressure P N/mm2(GPa)
1	18.91	13.39	9.48	25.04	6262.03(6.26)
2	38.01	21.44	12.37	45.34	4536.90(4.53)
3	48.88	36.39	8.52	61.56	3419.20(3.42)
4	12.37	9.42	10.15	18.55	5572.60(5.57)
5	33.69	18.25	9.96	39.57	4949.99(4.95)
6	21.26	15.07	8.88	27.50	3442.32(3.44)
7	15.73	15.73	7.80	23.60	7861.53(7.86)
8	7.32	10.99	7.14	15.01	3754.92(3.75)
9	24.14	21.50	8.82	33.51	4468.74(4.47)

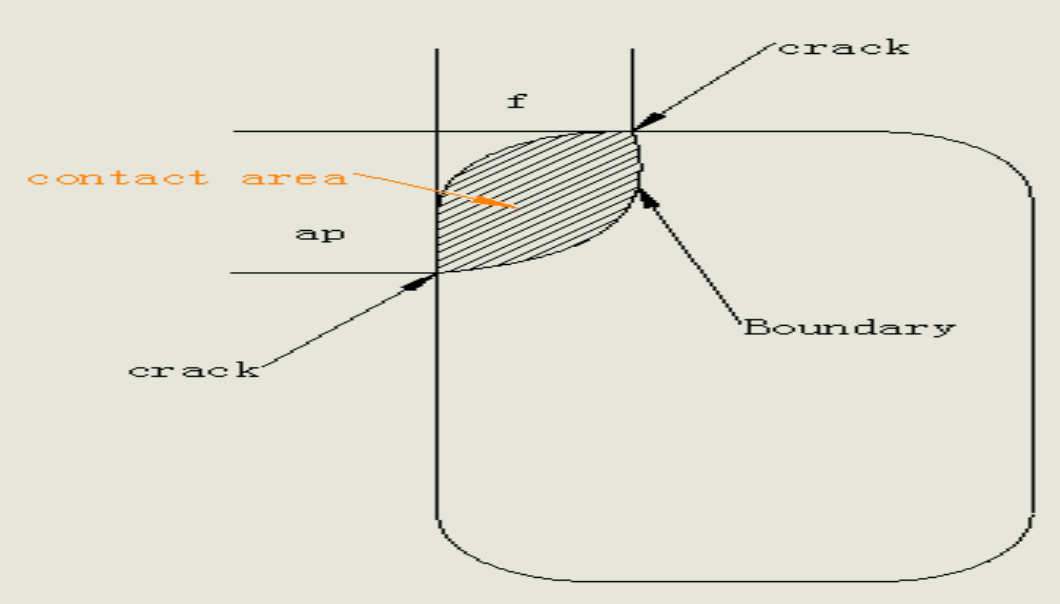

(a)

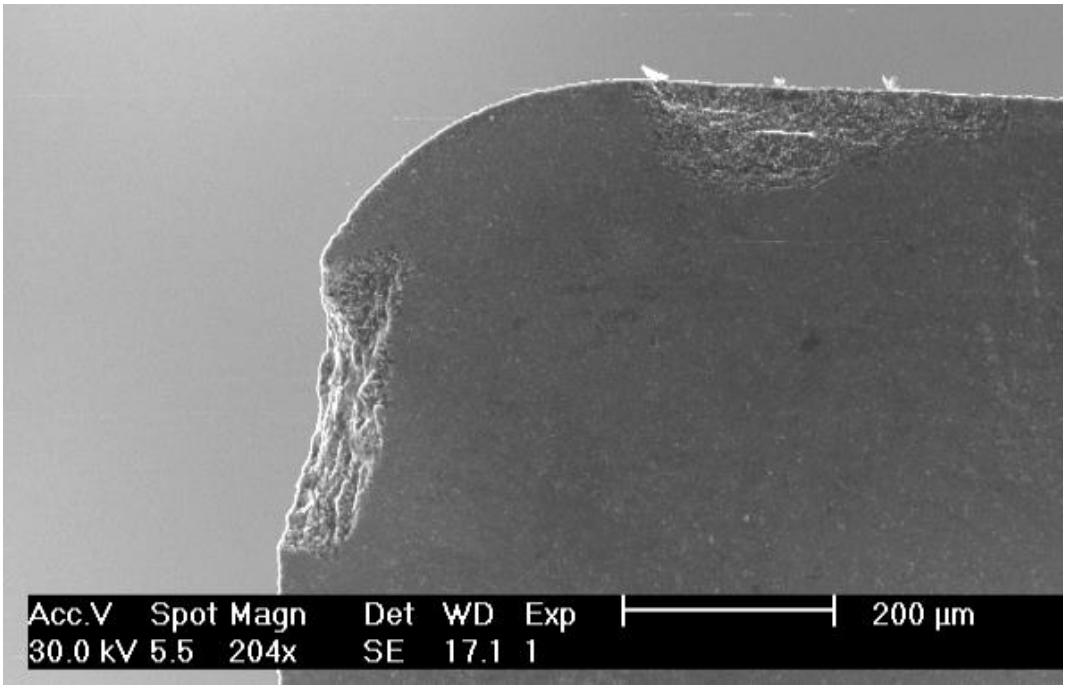

(b)

Figure 6.7 - The illustration of PCD insert and the SEM of the worn PCD tool: (a) The sketch of contact zone between PCD cutting tool insert and workpiece; (b) Side view of damaged PCD insert.

6.3.2 Stress concentration

Stress concentration was one of the possible reasons which lead to cracking. Figure 6.8 (a) shows a new PCD insert with a tiny notch at the cutting edge; Figure 6.8 (b) shows that the chipping occurred at the same location of the insert after the tool was damaged in the machining process. This indicates that the existence of innate notches could possibly initiate cracks. Normally, the stress concentration always occurs on the blunt edge or the place with notches.

In order to further analyze the failing process of PCD tools, two finite element analysis (FEA) models were developed by using the commercial software program Abaqus. In the FEA models the same geometric parameters and material properties of the PCD inserts used in the cutting test were applied. Two simulations were conducted: the simulation of stress concentration on PCD tool edge with notches, and the simulation of brittle cracking on PCD tool edge. In the first model, Extend Finite Element Method (XFEM) was used to simulate the cracking on the notched edge of the PCD tool. The maximum stress principle (MAXPS) was employed as the failure criterion. The maximum compressive stress was 2.1 GPa [109], the failure displacement of specimen was 0.2 mm [110]. The pressure in contact area was set to be the 5.5 GPa as shown in Table 6.3.

The second FEM model was developed to simulate the catastrophic damaged on the nose of PCD insert at the last period of milling test. The material model was brittle cracking in which Rankine criterion was used. The direct stress after cracking was the same as the compressive limit in the first model. The failure displacement was 0.2 mm.

The result of the first simulation is shown in Figure 6.9 (a). It can be seen that stress concentration occurred at the notch of PCD insert after the pressure of 5.5 GPa was loaded on the contact area, and the initiated cracks appear on the notch. This indicates that the cutting edge of PCD which has a notch is prone to stress concentration during the milling process and will lead to tool failure. Therefore, a well ground PCD tool with sharp cutting edges is needed to avoid the crack initiation on the cutting edge. The catastrophic damage shown in Figure 6.9 (b) illustrates that the PCD collapse

along the shearing boundary of contact area. This result matches the fractograph of the damaged tool.

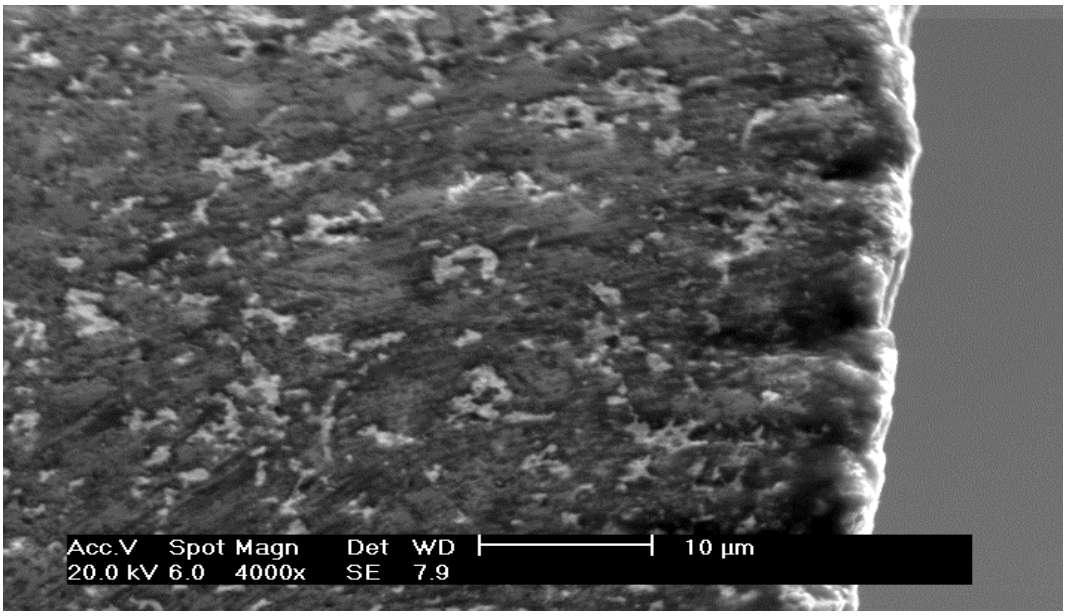

(a)

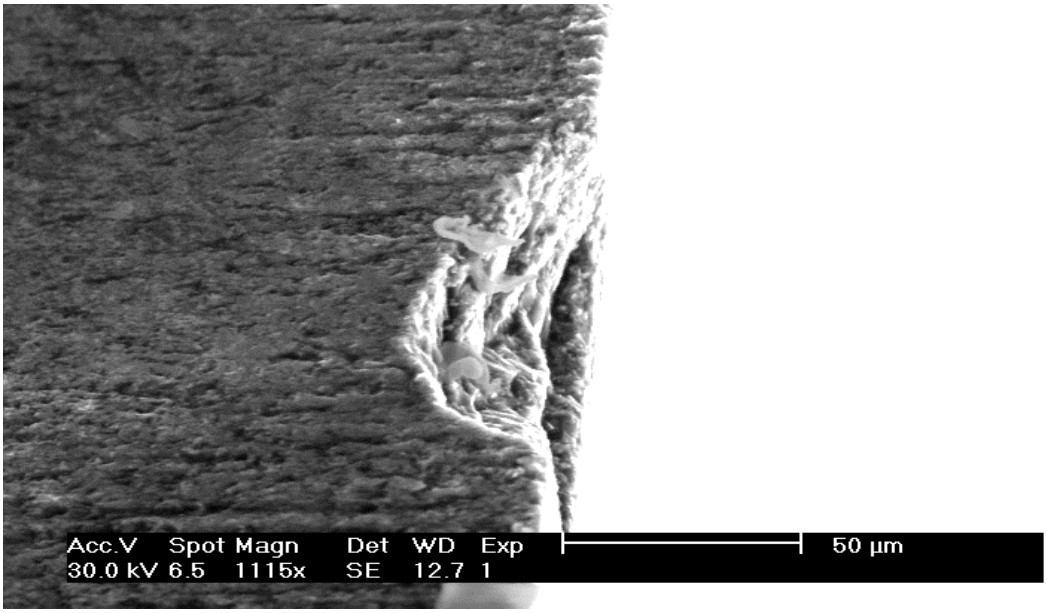

(b)

Figure 6.8 - SEM photos of cracking on the PCD insert (a) the irregular cutting edge of new, PCD insert (b) the damaged spot on the same PCD insert.

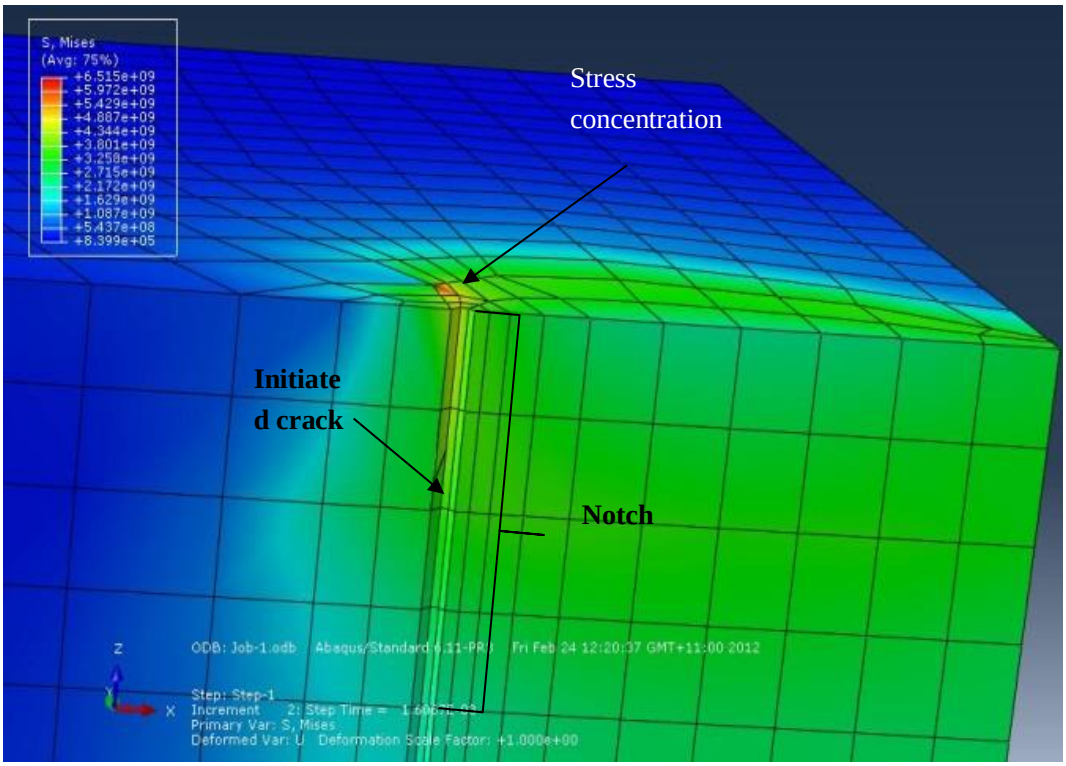

(a)

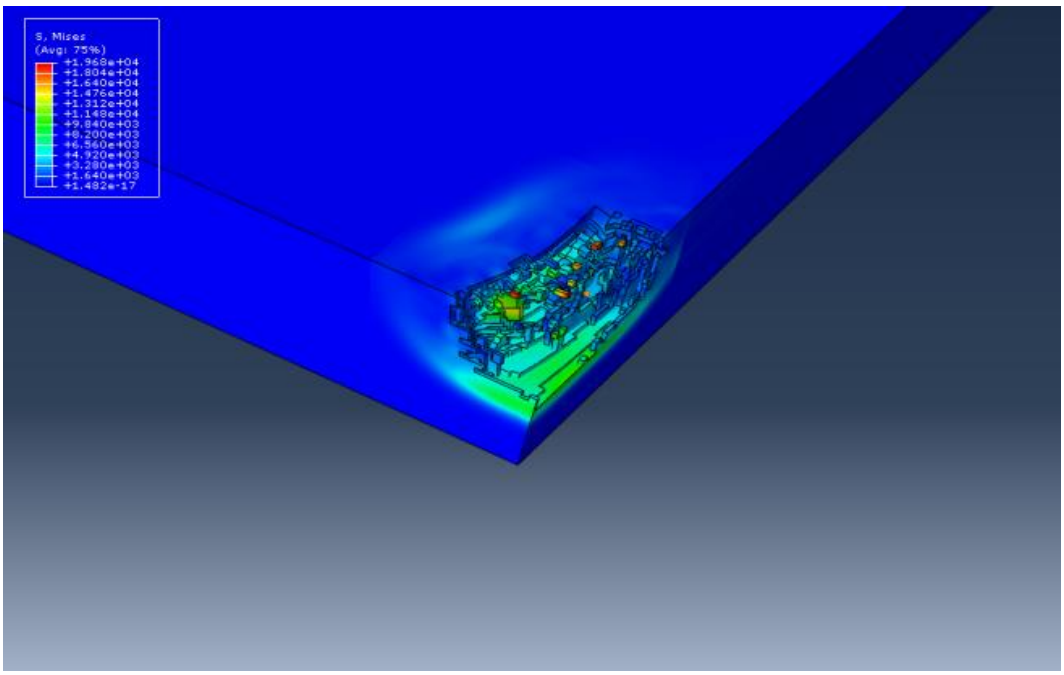

(b)

Figure 6.9 - The simulation of crack initiation with the load of 7.9 GPa: (a) The simulation of cracking initiation; (b) The simulation of use PCD material collapse.

6.3.3 Analysis of fractographs

Due to the special inhomogeneous structure of PCD, the wear and failure mechanism of PCD tool is more complicated than conventional cutting tools made of homogeneous such as Carbide and Carbon Tungsten. The wear and failure could be caused as the forms of adhesion, abrasion, brittle chipping, fatigue, graphitization, and chemical reactions [111], or the combination of multiple factors above. In the experiments conducted, brittle and fatigue damages (Figure 6.10) were found to be the main forms of PCD tools wear. And the details of PCD fractograph and causes of tool wear were discussed as following paragraphs.

Figure 6.10 (a) shows the cleavage-like fractograph of the PCD tool. It was found on the tool used in Test 7. Figure 6.10 (b) shows the fractograph of the delamination and cohesive rupture on the PCD tool used in three tests (Tests 1 - 3). Figure 6.10 (c) shows the cracks propagated in two directions; the tool was examined after the eight tests (Tests 10 - 17) were completed.

As shown in Table 6.3, the average pressure on the PCD tool in Test 7 is around 7.86 GPa. It can be seen in Figure 6.10 (a) that no significant plastic deformation occurred and no dimple ruptures could be found. Flank wear at the edge was visible. It is reasonable to assume that the chipping section of PCD insert was rubbing in the milling process. The friction effect was the main factor for this kind of failure. The rubbing action removed a small amount of material from the original fractograph and "polished" it.

Delamination was found on both Figure 6.10 (b) and Figure 6.10 (c). Being the sintering material, the inside physical structure of PCD, the binding between Cobalt and Diamond particles and the binding between Diamond and Diamond particles, determines the mechanical properties. The break of these bindings or the dislodgement of diamond particles from the structure is unpredictable. The delamination in the fractograph is caused by the inhomogeneous property of PCD. The innate voids of the material distribution inside PCD can contribute to such kind of failure.

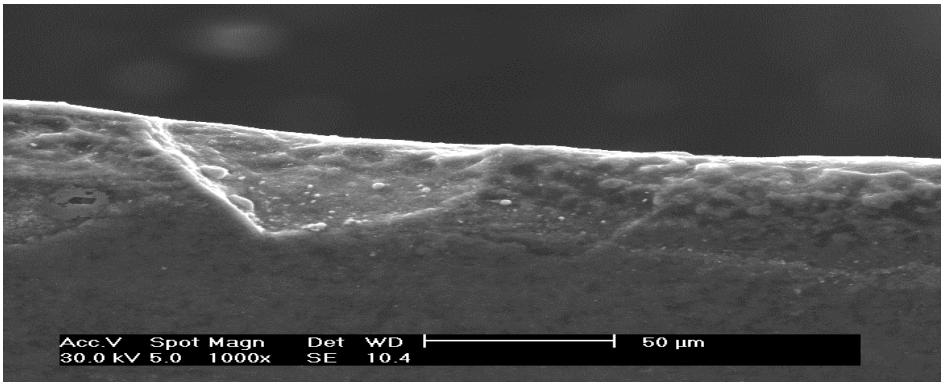

(a)

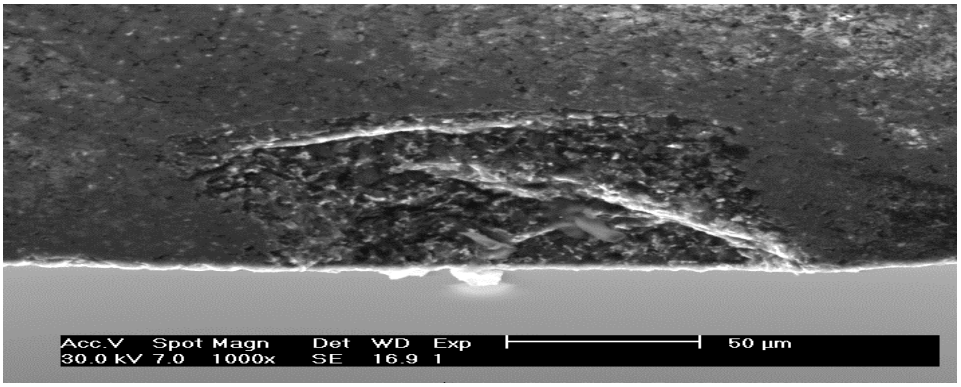

(b)

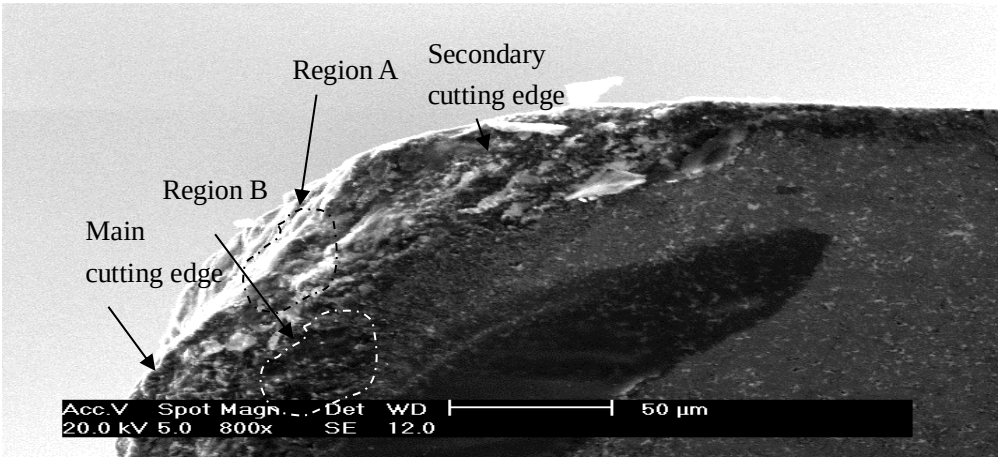

(c)

Figure 6.10 - SEM image of damaged PCD Samples: (a) cleavage-like fractograph on the secondary cutting edge; (b) the cohesive rupture and delamination on the secondary cutting edge (c) the directional damage at different regions on the PCD insert.

In Figure 6.10 (c), the damage area on the insert can be roughly divided into two different regions: Region A and Region B. In Region A, the crack or the fracturing path propagated along the direction which is vertical to the cutting surface; In Region B, the rubbing occurred at the main cutting edge. Region A is the result of the over loading on brittle material. The brittle cracking happened when the pressure became higher than the compressive limit. The cracks propagated in the direction of pressure, and finally led to the collapse of the PCD. As for Region B, this area suffered less stresses in the process. When the normal pressure was above the compressive limit of PCD, the shearing occurred at the contact boundary of the secondary cutting edge. But the area of Region B might bear the low normal pressure which was lower than the compressive limit of PCD. Therefore, it is reasonable to believe that the friction effect dominates this area.

6.3.4 Tool life and tool wear evolution

Unlike the turning process, the cutting edge of a milling tool is under continuous cyclical impact of the periodical cutting force. A few loading cycles would not result in obvious cracks on the PCD surface [109], this generated were 100 to 1000 indentations. With the increase in the number of cycles, fatigue fail may cause damage to the PCD. Similar phenomenon had been observed by Lin et al. [109]: the PCD was broken after 5000 loading cycles with a load of 30 KN. The compressive strength of notched PCD compact varied from 1.9 to 4.7 GPa, the PCD tool was broken after 28671 cycles when quasi-static loads were applied.

In the cutting experiments, when the normal pressure was up to 4.9 GPa, no obvious crack was found on the edge or the normal surface of the PCD insert after 4265 cycles (Figure 6.11). When the number of cycles reached 27750, micro chipping appeared (Figure 10 (b)). Also, inconsistent tool life was found among the same type of PCD tools: under the same cutting conditions, different tools made with the same type of PCD showed different tool life or cutting performance. Figure 14 illustrates the photos of the tools which were taken after 24000 cycles. It can be seen that one tool (Figure 6.11 (b)) maintains sharp cutting edge, but damages occurred in the other tool (Figure 6.11 (c)). The cause that leads to such ununiformed performance is the random distribution of initial defects in the PCD material. The numbers of defects

and some large voids in PCD can reduce the Young's Modulus and density distribution inside the PCD. [112]

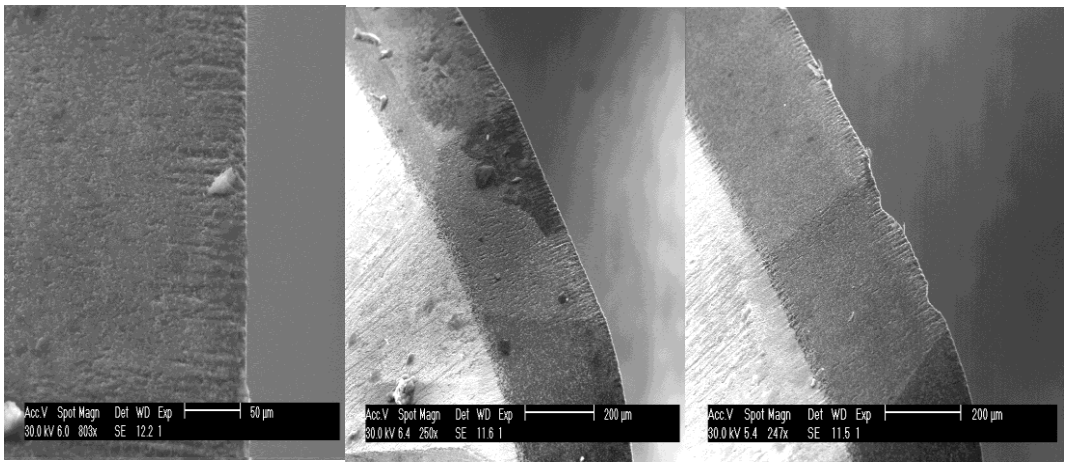

(a) (b) (c)

Figure 6.11 - SEM images of 2 PCD samples after the same loading cycles: (a) SEM image of the PCD tool after 4265 loading cycles; (b) the new-like PCD sample which was examined after 24000 milling cycle; (c) the damaged PCD sample which was examined after 24000 milling cycle.

In the experiment observations made on the cutting tool wear and fractographs revealed that the tool wear along chip flow direction is significant. It is observed that due to combined effect of high Yield stress and Low Young's Modulus (114GPa) ratio which allows titanium alloys only small plastic deformations resulting wear on the cutting edge causes 'Flute' type of Fractograph which appear similar to plates in drapes or long parallel grooves on architectural columns [113]. Figure 6.12 shows the comparison of Wear from the experimental tool to the ASM Metals hand book

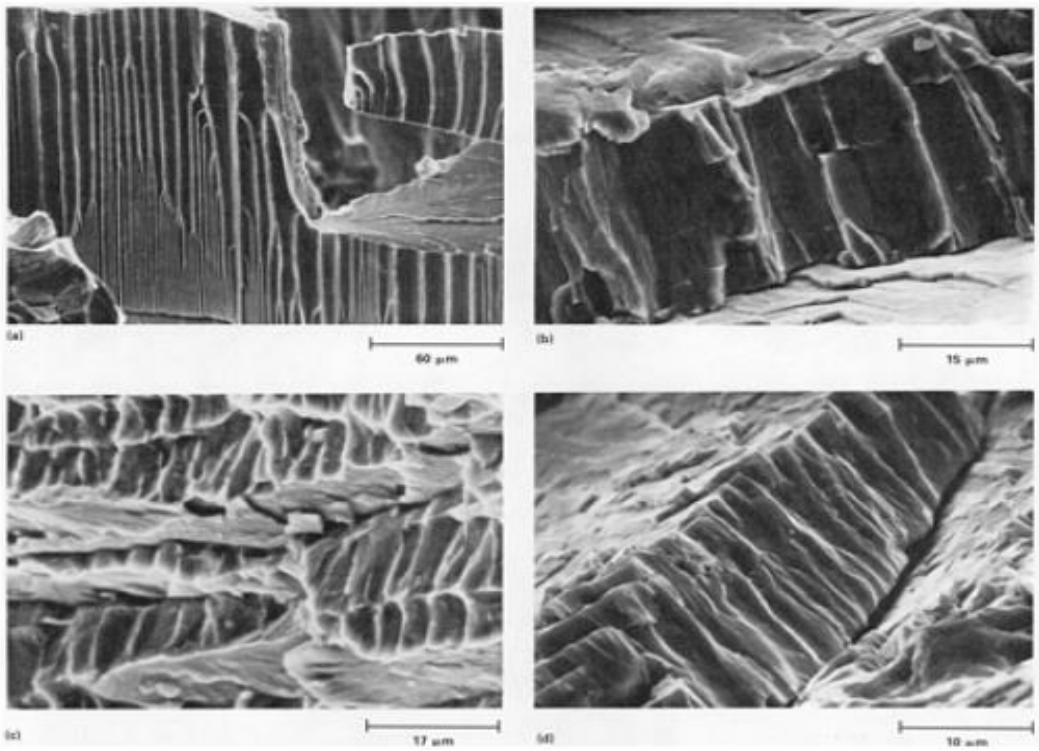

(a)

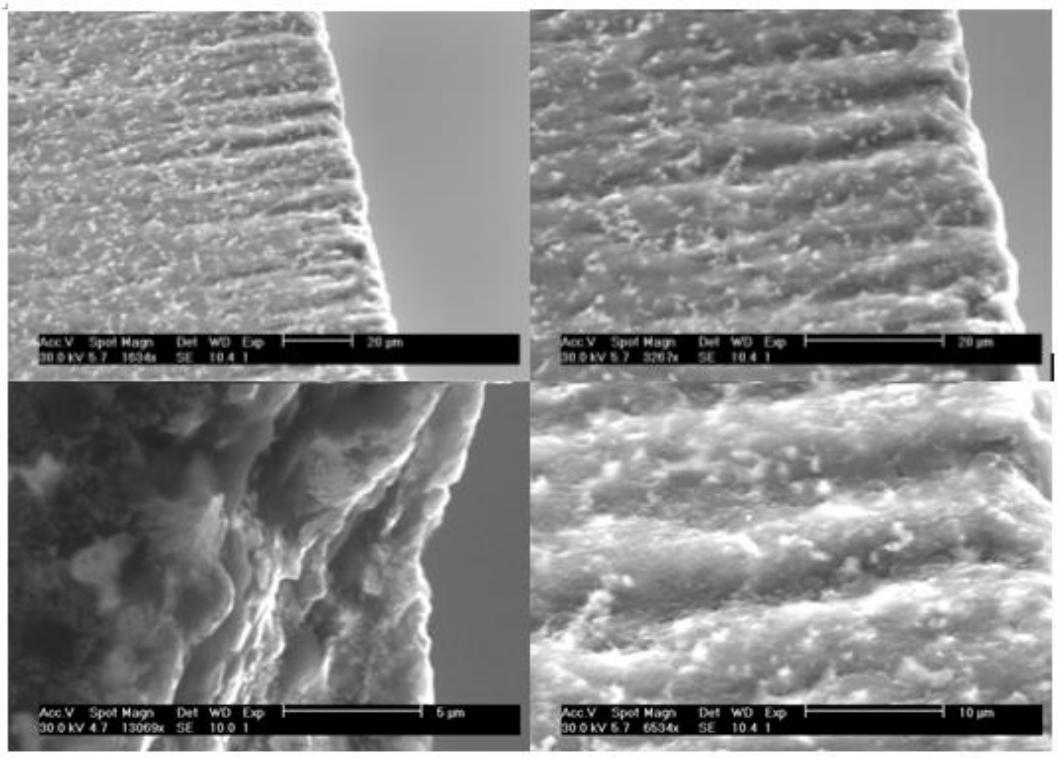

(b)

Figure 6.12 - (a) Flute Fractograph (ASM); (b) Flute Wear observed of test tool [113].

For the tool life analysis, two brand new tools of same geometry were used with same cutting parameters except the feed. In the first experiment the tool life was measured after every 302.4 mm cut with the feed of 300mm/min, axial depth of cut of 0.2mm and at a cutting speed of 180m/min. Figure 6.13 shows the images taken after every test cut. By analyzing the recorded wear data we notice that after the first test cut there is about 5-10 microns wear on the cutting edge with some built up edge. After the second test cut the tool wear remains within the range of 5-10 microns whereas the built up edge increased during this run. After the third test cut it is observed that there is dramatic increase in the tool wear amounting between 40-50 microns. It showed more flank wear compared to crater wear. After the fifth test cut the tool showed the retention of the previous wear pattern which was about 50 microns, but in the fifth run the wear remained around 50 microns but it is observed that it had increased built up edge. Figure 6.13 shows the wear pattern of the tool after each test cut.

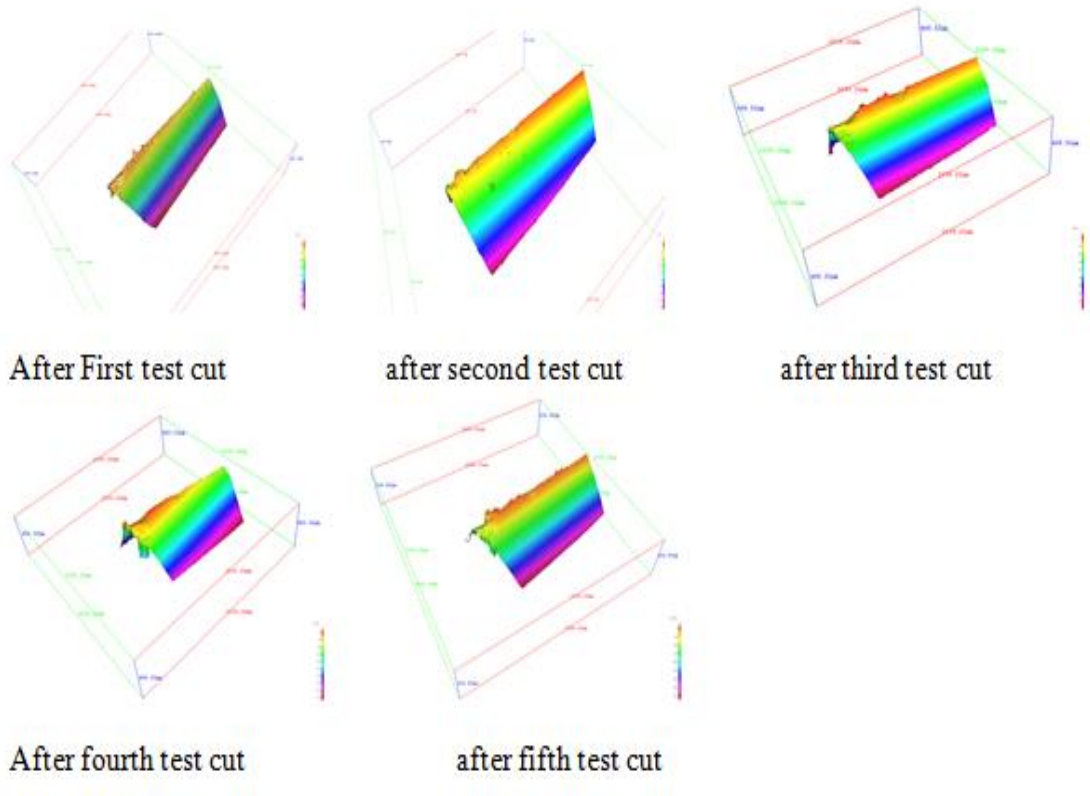

Figure 6.13 - The tool wear pattern measured after every test cut of 302.4mm with feed of 300mm/min cutting speed of 180m/min and axial depth of cut of 0.2mm.

In the second experiment the feed was increased to 400mm/min keeping all the other parameters same as the first experiment. The wear pattern on the cutting tool was measured on the Alicona microscope and analyzed. After the first test cut the tool has 1-2 microns of flank wear but there was a signs of crater wear in this tool with some built up edge. After the second test cut it was observed that the crater wear increased but there was not much flank wear crater wear was around 5-10 microns. At the end of the third run the tool showed increased crater wear along with 30-40microns of flank wear. After the fourth run the tool has worn on both flank and crater up to 50 microns showing signs of built up edge with increased wear. After fifth run it was observed that there is not much wear from test cut four, it held up its wear as it was in the fourth test cut. Figure 6.14 shows the wear pattern of the test tool after each test cut.

Figure 6.15 shows the results of tool wear evolution test. It can be found that the tool wear increase sharply when the cutting length reached 600 mm. Until the cutting length got to 1200 mm, the tool wear increase speed has slowed down. By substituting the experimental results into Equation (6-1), the Taylor's Equation can be summarized as Equation (6-7).

$$fT_t^{0.9599} = 658.9773 \tag{6-7}$$

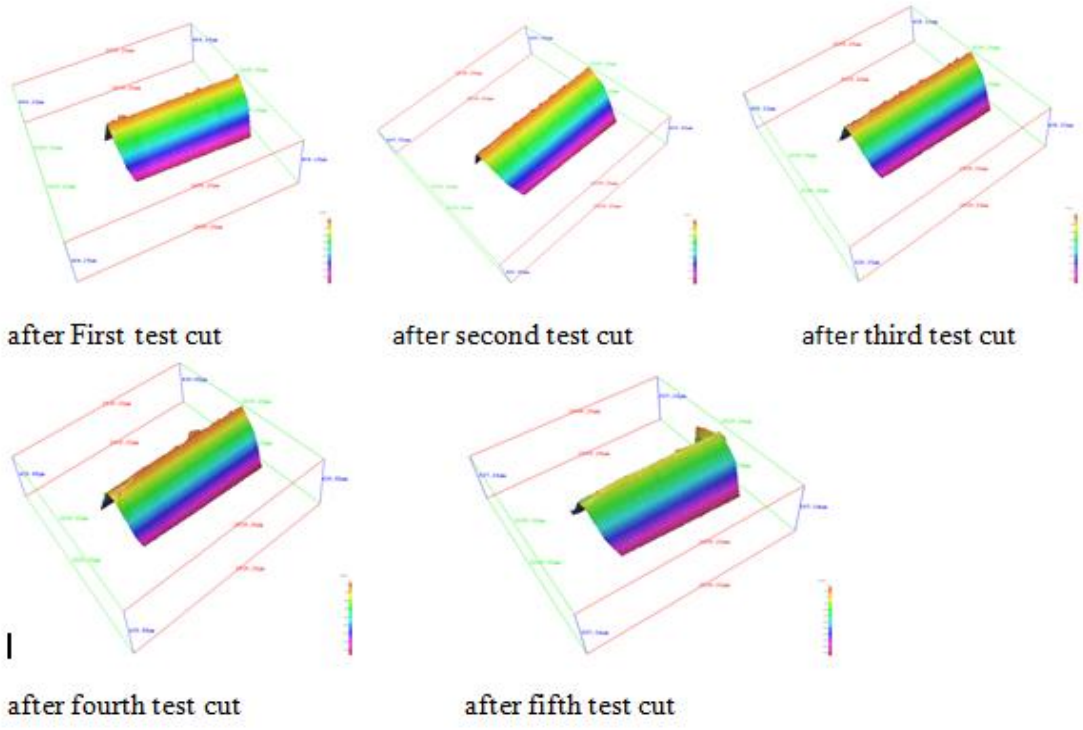

Figure 6.14 - The tool wear pattern measured after every test cut of 302.4mm with feed of 400mm/min cutting speed of 180m/min and axial depth of cut of 0.2mm.

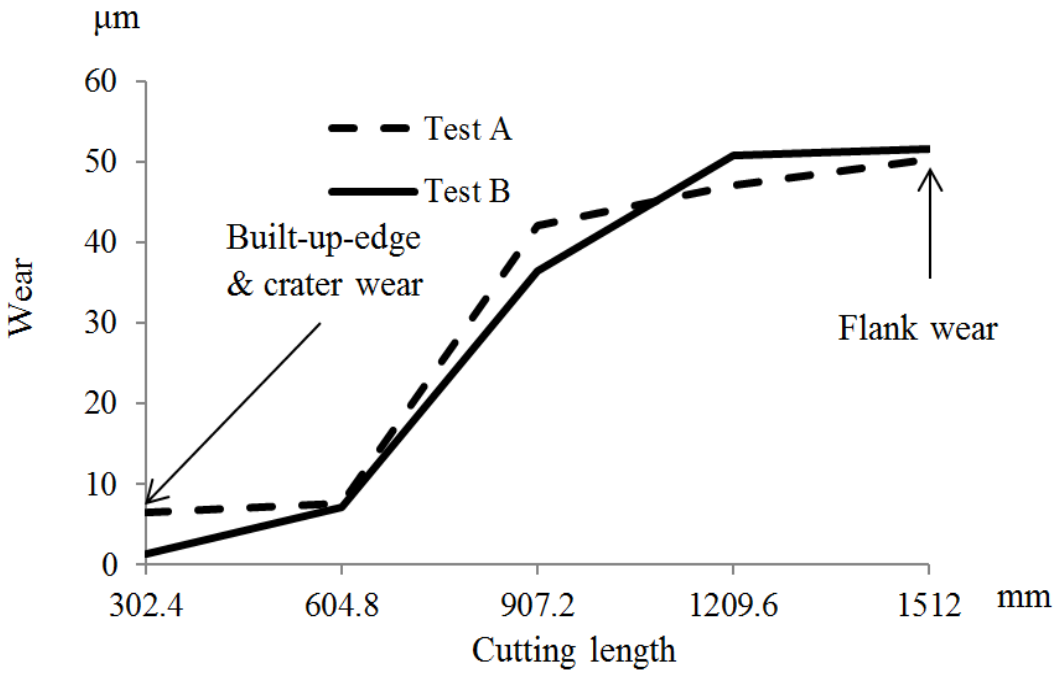

Figure 6.15 - Tool wear evolution.

6.4 Summary

No damage was caused on the PCD cutting tool inserts after 4265 loading cycle with the normal pressure of up to 4.9 GPa. A small damage of 0.05 mm was found after 24000 cycles with the same normal pressure.

Directional damages by the shearing and friction were found in the experiments. The cleavage-like fractograph was mainly caused by the rubbing action in the process and it appeared rarely in the experiment. The inhomogeneous material structure of PCD was the major factor which caused the delamination.

By analyzing the two types of fractograph it was found that there was huge impact of heat generated during the cutting on the tool wear. High cutting temperatures resulting due to low plastic deformation of Titanium alloy caused it close to the cutting edge and resulted in oxidation wear and flute type fractograph.

7 Surface quality and chip morphology

This chapter examines the influence of machining parameters on surface quality and investigates the chip morphology. It is known that an increase in machining parameters such as cutting speed, feed and axial cutting depth can shorten the tool life or increase the tool wear which will finally lead to poor quality of surface finish. This study optimizes the machining parameters by investigating the influence of machining parameters on the quality of surface finish. The new findings reveal that the serration frequency of the discontinuous chip has changed during machining process. The fluctuation in the instantaneous cutting force indicates the instability of the serration frequency.

7.1 Introduction

7.1.1 The surface roughness in fundamental machining theory

According to Groover [87], the surface roughness which represents the average of the vertical deviations from nominal surface over a certain measuring length on the surface of workpiece, is generally used to evaluate the finished surface quality. The expression of average roughness can be defined as Equation (7-1).

$$R_a = \int_0^{L_m} \frac{|y|}{L_m} dx \tag{7-1}$$

Where x is the differential length of the arbitrary measuring length (L_m) on workpiece surface. And the $|y|$ indicates the absolute distance from the peak nominal surface. Figure 7.1 illustrates the parameter x, L_m and $|y|$ in the measuring part. Another expression of average roughness is

$$R_a = \sum_{i=1}^{n} \frac{|y_i|}{n} \tag{7-2}$$

Where n is the number of measuring peak and y_i is the absolute height of every measuring peak on finished workpiece surface.

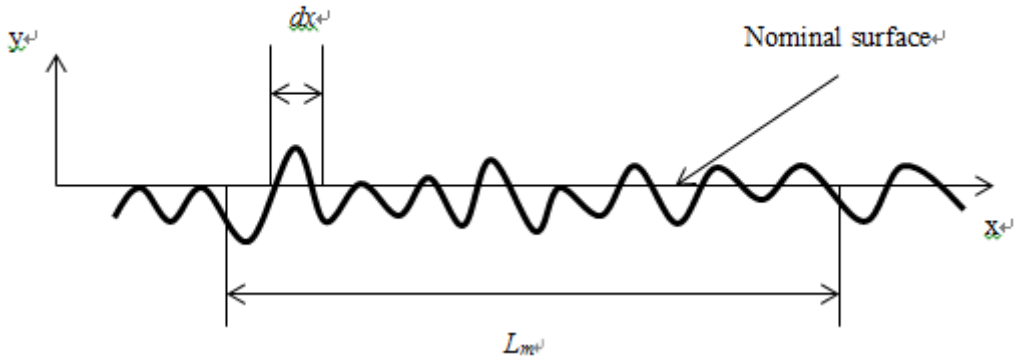

Figure 7.1 - The illustration of calculating parameters of average roughness [87].

7.1.2 Factors affecting surface roughness

Generally, the geometric factors which include the tool geometry, machining parameters and tool path of process can affect the surface roughness in the process. The influences of tool nose geometry and feed on surface roughness are shown in Figure 7.2 [87]. And the End Cutting Edge Angle (ECEA) can also affect the finished surface. According to Martellotti [114], the ideal surface roughness value in the process of slab milling can be presented as Equation (7-3).

$$R = \frac{0.125 f^2}{(D/2) \pm (f n_t / \pi)} \tag{7-3}$$

Where f is the value of feed, D is the tool diameter and n_t represents the tooth number of cutter. This expression clearly describes the relationship between feed, tool geometry and surface roughness.

Furthermore, the material properties of tool and workpiece can also affect the surface roughness. During the process, machining the material when significant work hardening is occuring will often lead to a built-up-edge on the tool nose. The built-up-edge can finally damage the finished surface. The friction effect is also a normal aspect which affects the surface finish. Due to the low thermal conductivity of

workpiece materials, the cutting heat generated in the process cannot be dissipated immediately after one milling cycle before the next. Heat accumulation will therefore result and the local cutting temperature will rise significantly. This situation may finally cause deformation of the finished workpiece. The characteristics of tool wear, vibration and runout in the process are also the important factors which contribute to a poor surface finish quality.

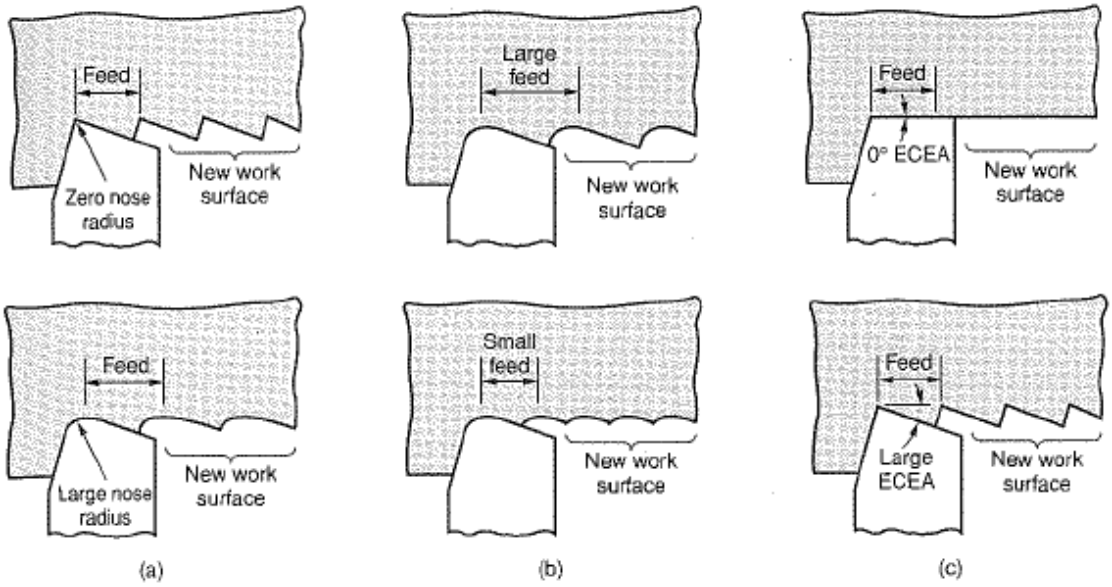

Figure 7.2 - The effects of geometric factors on surface roughness [87].

7.1.3 The factors affecting the chip morphology

Chip morphology analysis has been performed as standard practice over many decades. The chip serration is known as the result of the adiabatic shearing effect. Generally, this effect shows intense localization. In many studies, the heat conduction is ignored because of it is relatively slow compared to the rapid deformation process [115]. The characteristics of adiabatic shearing effect include the shearing frequency and the geometrical parameters of adiabatic shearing bands. From the view point of material engineering, there are some critical factors which affect the adiabatic shearing effect. These are: the thermal conductivity, thermal expansion and strain and strain rates.

In the milling process, it is known that the thermal properties of tools and workpiece influence the adiabatic shearing effect. The cutting speed is considered to be the critical factor determining the strain rate which also directly affects the adiabatic shearing effect.

The cutting speed reflects the speed of deformation and shearing. According to Wang's analysis, the shearing strain rate in the chip thickness direction within the shear band can be expressed as Equation (7-4).

$$\dot{\gamma}_1 = \frac{v(H - h_1)\sin\gamma_0}{\delta H \cos(\phi - \gamma_0)} \tag{7-4}$$

Where *v, H, h1, ϕ, δ, γ_0*are cutting speed, maximum thickness of sawtooth chip, chip thickness at local shear deformation, shearing angle, sawtooth chip shear band width and rake angle, respectively.

The expression of shear strain rate in the direction of chip width is

$$\dot{\gamma}_2 = \frac{v(b_D - b_{ch})\sin\phi\cos\gamma_0}{\delta h_D \cos(\phi - \gamma_0)} \tag{7-5}$$

Where b_D, b_{ch}, h_D are cut width, chip width and cut thickness respectively.

From equations (7-4) and (7-5), a linear relationship can be found between the cutting speed and the strain rate, the strain rate increasing with the cutting speed. As mentioned in the description of adiabatic shearing theory by Wright, the strain rate can affect the adiabatic shearing process. The changes of cutting speed will have influence on the adiabatic shearing effect as a matter of course.

The function of chip serration frequency was proposed in the following form by Sun:

$$f_{seg} = \frac{v}{L} \tag{7-6}$$

This expression describes the linear relationship between cutting speed, contact length of tool-chip interface and chip serration frequency. This equation also indicates the influence of cutting speed on the adiabatic shearing effect.

7.1.4 The structure and objectives

In this section, the study is focuses on two main aspects: the analysis of the machining parameters' influence on the surface quality and the analysis of chip morphology.

The average surface roughness is used for evaluating the finished surface quality in the process of milling Ti6Al4V with PCD cutting tools. Up to 22 groups of machining parameters were run in the experiment to investigate the influence of cutting speed, feed and axial cutting depth. The relation formula of average surface roughness and feed is obtained by substituting the experimental results and corresponding machining parameters into equation (7-3).

As discussed in Section 7.1.3, the chip serration frequency is affected by the machining parameters and thermal properties of work materials. The objective is aimed at investigating the Ti6Al4V chip serration frequency's relationship to the cutting speed and the instantaneous cutting force.

The procedure of analyzing surface quality and chip morphology is illustrated in Figure 7.3.

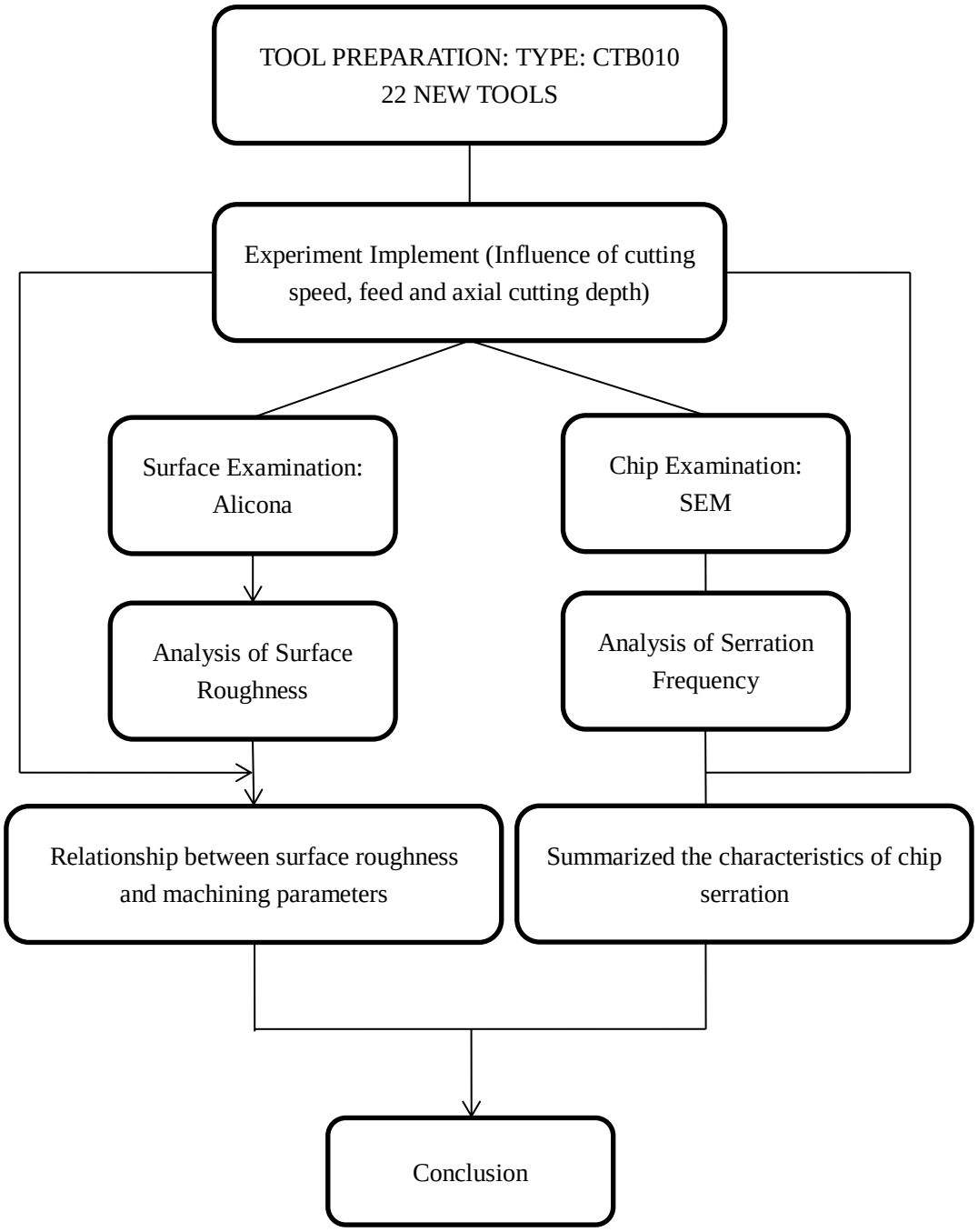

Figure 7.3 - Structure of studying surface quality and chip morphology.

7.2 Experimental setup

7.2.1 Experimental devices

Machining tests were carried out on a HAAS VF 1 CNC vertical milling machine which is programmed using EdgeCAM with cutting parameters shown in Figure 7.4. The Kistler Piezoelectrical Dynamometer was mounted directly on to the bed, where the workpiece is clamped, to record the instantaneous cutting forces during machining. During the test run the dynamometer measures voltage fluctuation which is recorded and converted in to Cutting force. The machining was performed with Diameter 6mm Brazed PCD tip (CTH-25) straight flute cutter at two different feeds of 300m/min and 400m/min, cutting speed of 180m/min with the axial depth of cut 0.2mm. The cutting forces were measured during machining in both the cases and analyzed. After each test the tool wear and surface finish was measured under an Alicona microscope to analyze the tool life and SEM was used for wear characterization and analysis. For the tool life test, two new cutters were used with the machining length of 302.8mm between each measurement with 5 test cuts for both the tools.

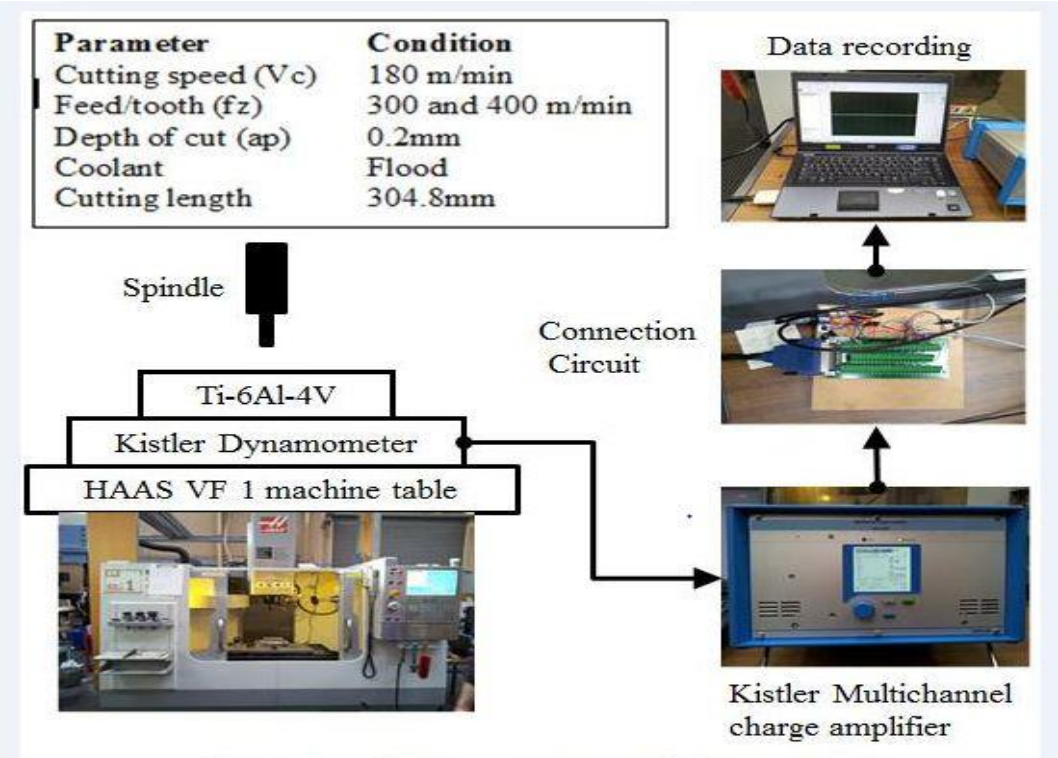

Figure 7.4 - Experiment Setup.

7.2.2 Material Information

The properties of Titanium alloy Ti6Al4V (ASTM B265, Grade 5) have been shown in the Table 7.1. This material has been chosen because it is the most widely used accounting for more than 50% of all titanium tonnage in the world. It has very high corrosion resistance and resistance chemicals.Ti6Al4V has Salt Creep Cracking below 0.1% at temperatures below 425 Degree Centigrade. The PCD tool (CTH-25) was clamped directly in the collet chuck. The properties of the tool material are shown in Figure 7.5.

Table 7.1 Mechanical properties of titanium alloys.

Tensile strength (Mpa)	0.2% proof stress (Mpa)	Elongation (%)	Density (g cm^{-3})	Melting point (℃)	Measured hardness (C.I.-99%)[a] HV_{100}	Thermal conductivity at 20 ℃(W/mk)
900-1160	830	8	4.5	1650	Min.Z341, Max. Z363	6.6

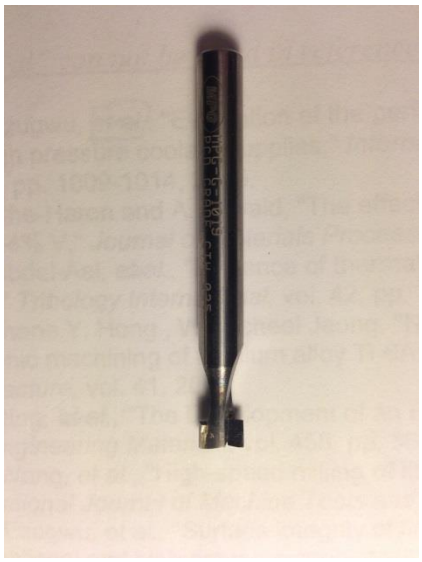

Description	Value
Knoop Hardness	60-120GPa
Thermal conductivity	400W/mK
Transverse rupture strength	1200MPa
Fracture toughness	9.1 ±0.59MPa/m

Figure 7.5 - PCD tool and Parameters.

In the milling process, the cutting force keeps varying as it is an intermittent cutting process. It has a high penetration force at the beginning of the cut when cutting tool enters the work material. It will then reduce and stabilize as it continues to cut through the material. Cutting force is one of the major physical variables, the study of which can help optimize the machinability, tool life, tool wear patterns, chatter of the machine and machining accuracy. By measuring the cutting force we can analyze the force required to shear the material in machining from which we can determine the force acting on the cutting tool edge. The cutting force in this experiment was measured by the Kistler Multichannel charge amplifier coupled with the Kistler Piezoelectrical Dynamometer. The machined surface can be described by various measurements referring to its roughness, waviness and its profile. The surface finish is specified by its roughness value (R_a), the lower the Ra value required on the surface the higher the cost and time required to produce it. Therefore it is necessary to analyze the optimum cutting parameters that can produce the lowest R*a* value. The surface

finish is measured after each test cut and recorded in this experiment for analysis.

7.3 Surface quality analysis

Table 7.2 shows the analysis of cutting force under different machining conditions. *MaxErr* is the error between the average cutting force and the maximum force; MaxForce is the maximum value of cutting force and MinForce is the value of minimum cutting force.

According to *MaxErr,* it can be seen that cutting speed V_c has small effect on the stability of cutting force. *MaxErr* increase significantly with the increase of f_t and a_p. The cutting force becomes more unstable when a larger feed and axial cutting depth are used. However, *MaxErr* remains at a low level when feeds are between 0.01 mm/rev to 0.06 mm/rev.

Figure 7.6 shows the profiles of finished surfaces that were machined with different cutting parameters. The length measured in each profile is 1.8 mm. The average distance (AD) between the peak and central axis (refer to Figure 7.6) was used to analyse the surface quality. Figures 7.6(a) and (b) are to compare the results of different cutting speeds; Figures 7.6(c) and (d) are to compare the results of different feeds.

Table 7.2 Analysis of cutting force.

Cutting Parameters			Cutting Force			
Vc (m/min)	fz (mm/rev)	ap (mm)	MaxForce (N)	MinForce (N)	MaxErr	AverageForce (N)
65.9734	0.025	0.2	85.3987	60.0005	20.9219	64.4768
87.9646			84.563	65.0014	15.6939	68.8691
109.9557			83.5276	67.0017	12.5923	70.9353
131.9469			87.1009	70.0244	13.7172	73.3837
153.938			92.8007	73.0044	16.2739	76.5268
175.9292			80.6315	68.0004	9.8043	70.8272
197.9203			90.2398	70.0024	14.9923	75.2475
219.9115			90.6723	70.0027	15.1674	75.5049
131.9469	0.01		95.1483	65.0029	23.9056	71.2427
	0.02		98.3134	70.0007	23.2455	75.0679
	0.03		92.4493	70.0002	17.4115	75.0378
	0.04		111.3221	65.0002	36.1843	75.1378
	0.05		109.9102	76.0005	25.7409	84.1693
	0.06		129.954	90.003	29.3976	100.5564
	0.07		160.1044	98.4249	46.8082	113.2962
	0.08		193.3536	120.0175	55.2258	138.1278
	0.03	0.1	78.2258	52.0025	19.2357	58.9901
		0.2	122.6459	75.0009	35.6921	86.9538
		0.3	162.0886	117.0238	32.182	129.9066
		0.4	171.5562	124.0013	35.0979	136.4583
		0.5	228.1216	128.0029	73.365	154.7566
		0.6	208.3219	121.0103	55.3518	152.9701

Based on the profiles shown in Figure 7.6 (a), the AD is found to be to be 1.85 μm when cutting speed is 65.97 m/min (Figure 7.6 (a)); 1.3 μm when cutting speed is 175.93 m/min (Figure 7.6 (b)). It is clear that the surface finish of the workpiece machined with a cutting speed of 175.9292 m/min is slightly better than that of 65.97 m/min. In Figure 7.6 (c) and Figure 7.6 (d), a sharp contrast exists between the workpiece machined with feeds of 0.01 mm/rev and 0.08 mm/rev. The AD of 0.01 mm/rev is 1.5 micro meters but the AD of 0.08 mm/rev is up to 5 micro meters. Overall, it can be concluded that the surface quality became poor when large feed was applied, higher cutting speed and lower feed can result in better surface quality. However, according to the results of Table 7.2, to use the feed in the range of 0.01 mm/rev to 0.06 mm/rev, the cutting force will vary slightly, which indicates that the

surface quality will not be affected significantly.

For studying the influence of feed on machined surface, the machining parameters are set to constant cutting speed (168m/min), constant axial depth of cut (0.2mm) and changing the feed (0.02mm/tooth to 0.045mm/tooth). To measure the surface roughness, the cutting length is 15mm in each test cut sample by using a 2 flute diameter 7mm Brazed tip PCD cutting tool. The measurement spots on the workpieces and the average roughness scanning results are shown in Figure 7.7 and Figure 7.8. And the surface roughness measured during the analysis of the test surface is summarized in the Table 7.3. Close analysis of the results show that at a feed of 0.035mm/tooth yields a low roughness value at a cutting speed of 168m/min. on further observation it is found that at feed of 0.020mm/tooth the surface roughness is less in some regions has a higger value at other places due to chatter. It is also observed that if the feed is too low then it result in chatter formation on the machined surface leading to an uneven surface roughness value. In Figure 7.7 the highlighted area indicates the waviness in the surface with feed of 0.02mm/tooth. Whereas 0.04mm/tooth feed shows deep grooves in the surface intermittently. According to Equation (7-3), the average roughness of the finished surface is supposed to have an exponential relationship with the feed. However, in this experiment, the relationship between feed and average roughness does not satisfy Equation (7-3). The value of average roughness has a significant drop before the dramatic increase when the feed increased above 0.35 mm/tooth.

Table 7.3 The roughness of finished surface.

Feed/Tooth	0.02mm	0.025mm	0.03mm	0.035mm	0.04mm	0.045mm
Roughness Value(Micron)	0.75	0.7	0.6	0.5	0.8	1

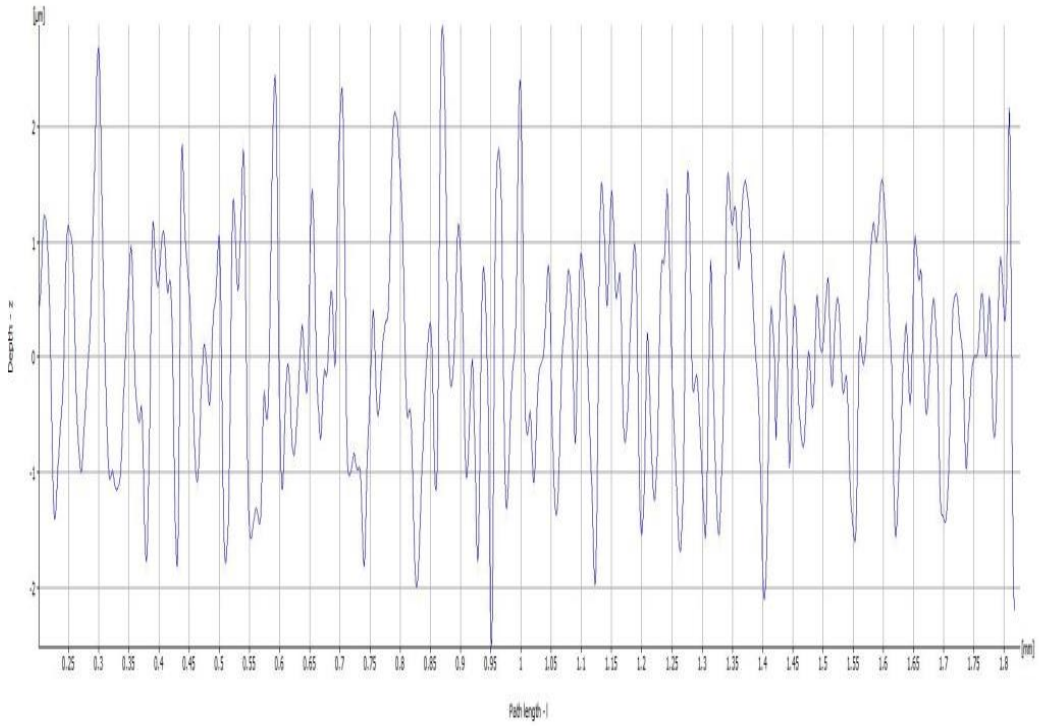

(a)

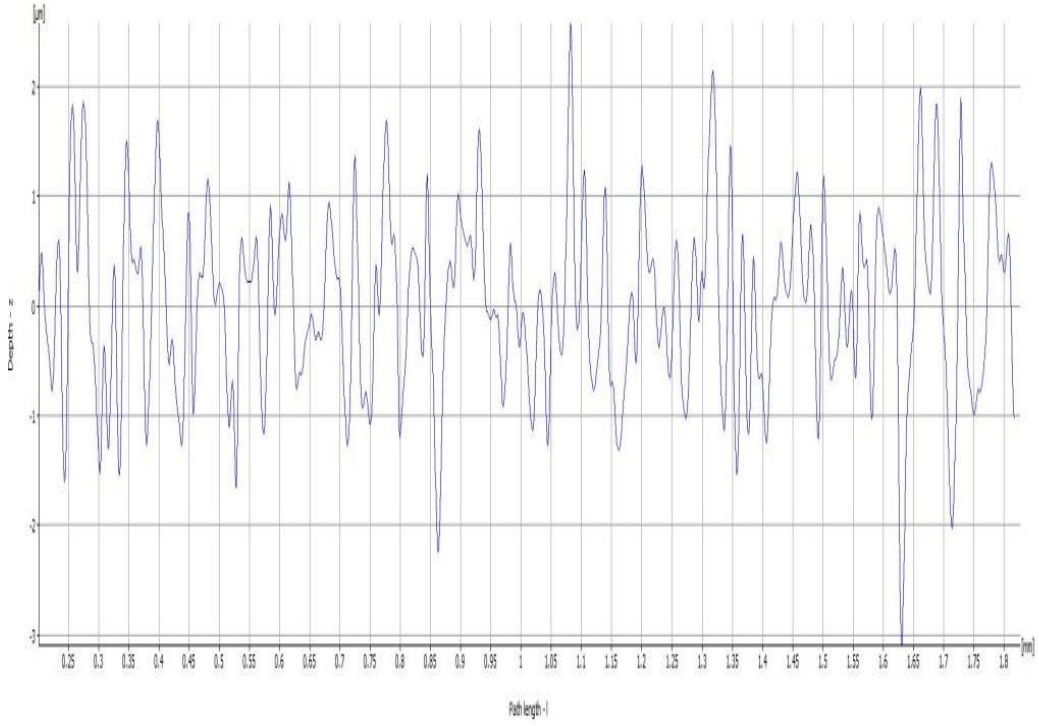

(b)

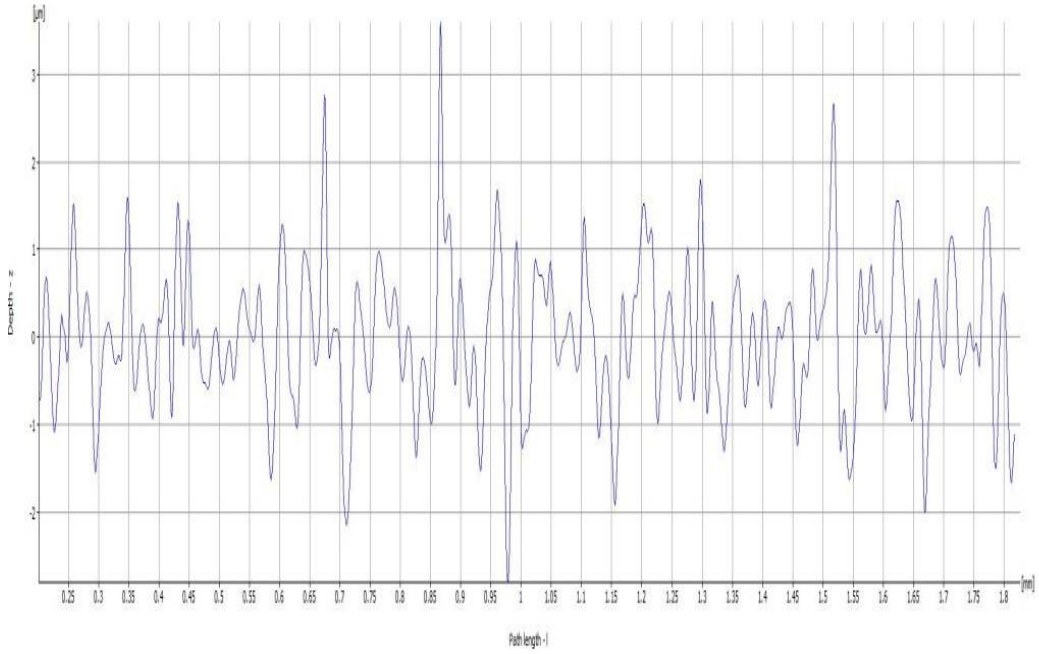

(c)

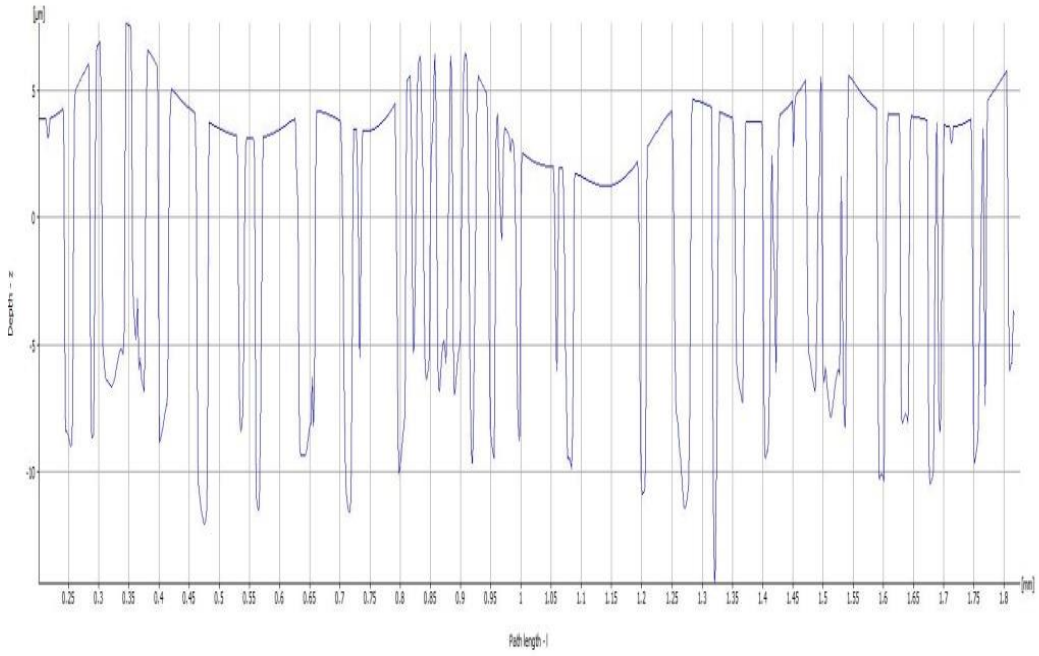

(d)

Figure 7.6 - Profiles of Titanium workpiece obtained with different machining parameters: (a) Cutting speed of 65.97 m/min, (b) Cutting speed of 175.92 m/min; (c) Feed of 0.01 mm/rev (d) Feed of 0.08 mm/rev.

Figure 7.7 - Surface images of the test cut at different feeds.

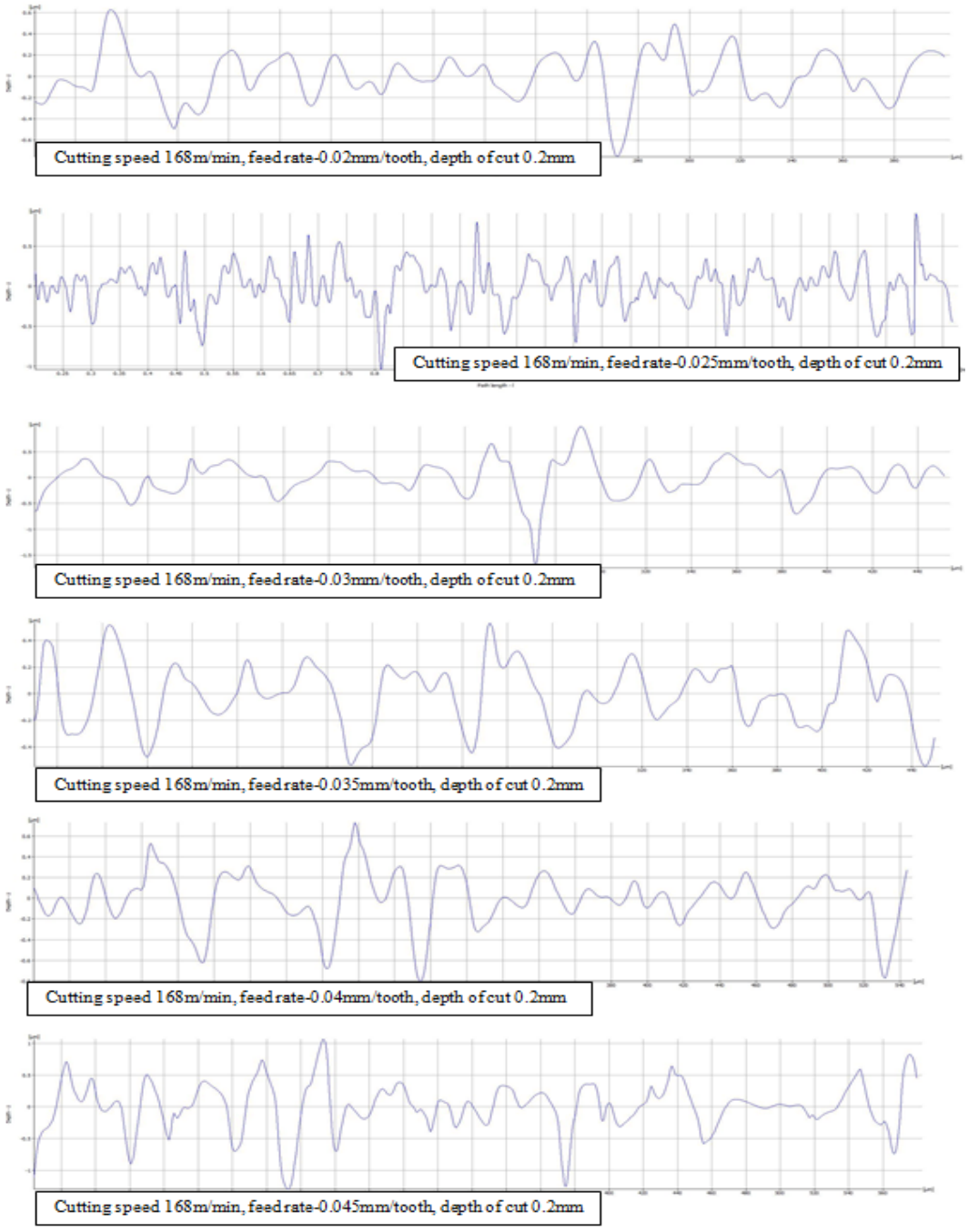

Figure 7.8 - Graph showing surface roughness on test surface at different feeds.

7.4 Chip morphology analysis

Many researches have been conducted to analyze the chip segmentation frequency in machining Ti6Al4V. For example, Molinari established the relationship between chip serration frequency and cutting speed [68]. Similar result has also been found by Miguélez et al. [69]. However, the change of serration frequency on one single chip has not been studied by any researchers.

Figure 7.9 shows one of the chips collected in our experiments. It can be seen that two different sections existed on this chip. The two sections with different serration frequencies were separated by a clear boundary, which indicated that the chip formation suffered a great change during the material removing process. The different adiabatic shearing frequencies of the two sections were 0.440×10^3 KHz and 2.199×10^3 KHz, the latter is nearly 5 times higher than the former. Most chips produced in this experiment have the similar serration frequency.

Similar to most other chips collected in the experiments, the change in serration frequency on this sample occurred at the position of 25% of total length (l_{Total}). Figure. 7.10 (a) shows the clear boundary existing between the two sections. By examining the instantaneous cutting force in Figure 7.10 (b), it can be found that the cutting force rose dramatically at the beginning of the milling cycle, but decreased slightly in Region A as shown in Figure. 7.10 (b). In the milling process, the strain rate varies all the time because of the change in the thickness of uncut chips. Since the strain rate can significantly affect the chip formation, the unstable strain rate was probably one of the reasons causing the sudden change in frequencies. Meanwhile, the accumulation of heat was getting more and it could not be dissipated due to the extremely low thermal conductivity of Ti6Al4V. Therefore, it is reasonable to conclude that the generated heat would provide the energy for changing chip serration frequency.

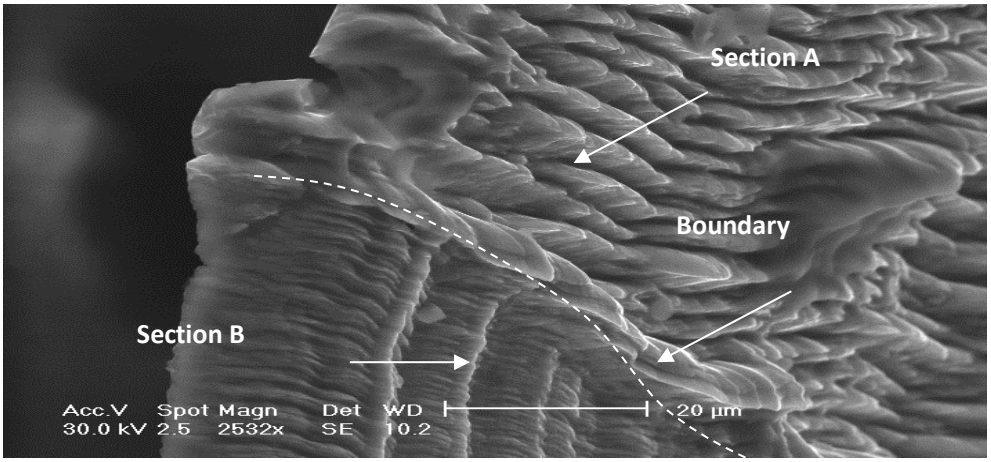

(a)

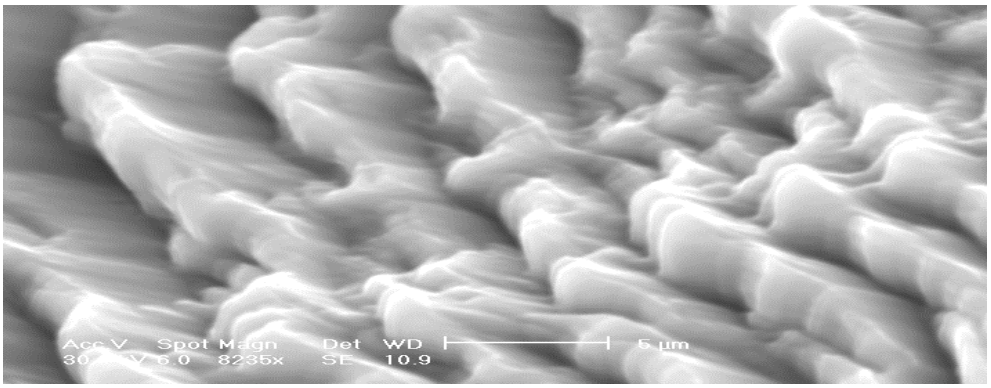

(b)

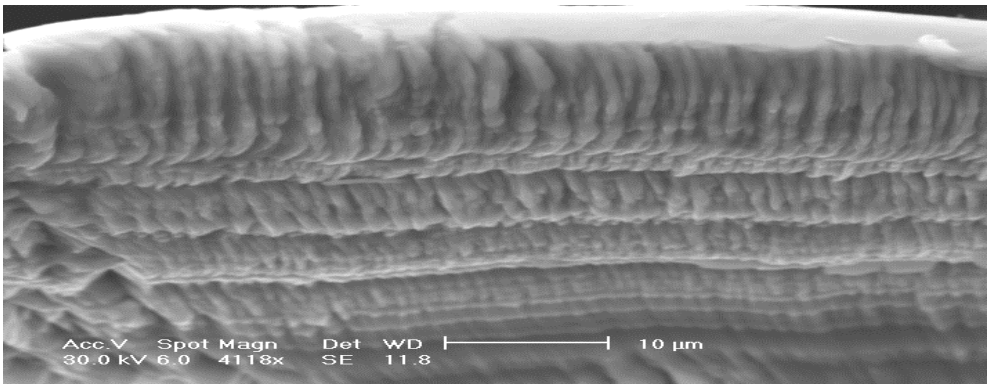

(c)

Figure 7.9 - The two sections with different adiabatic shearing frequencies (a) the magnified image of boundary between two sections (b) section A with 0.440×10^3 KHz (c) section B with 2.199×10^3 KHz.

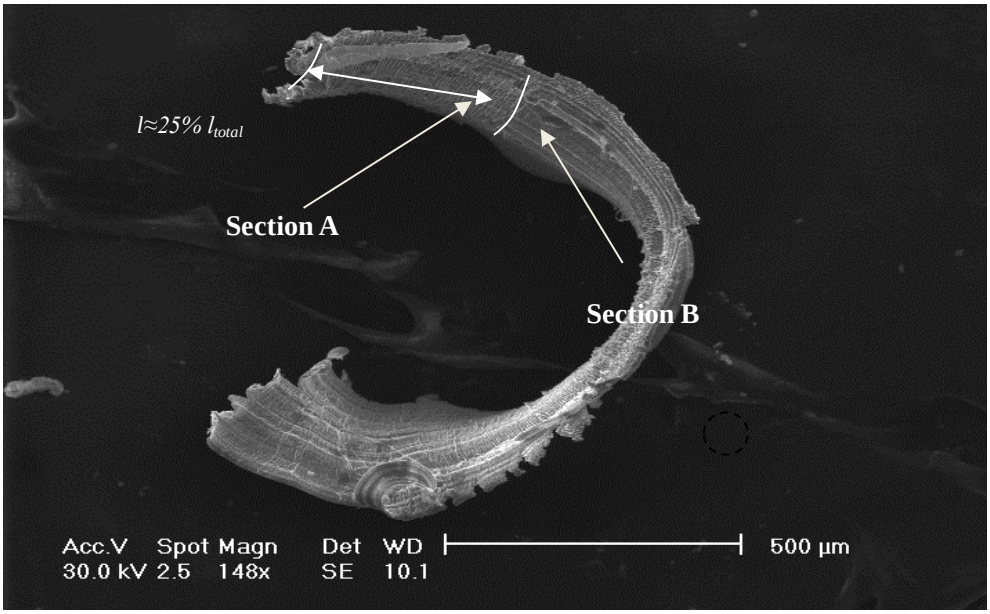

(a)

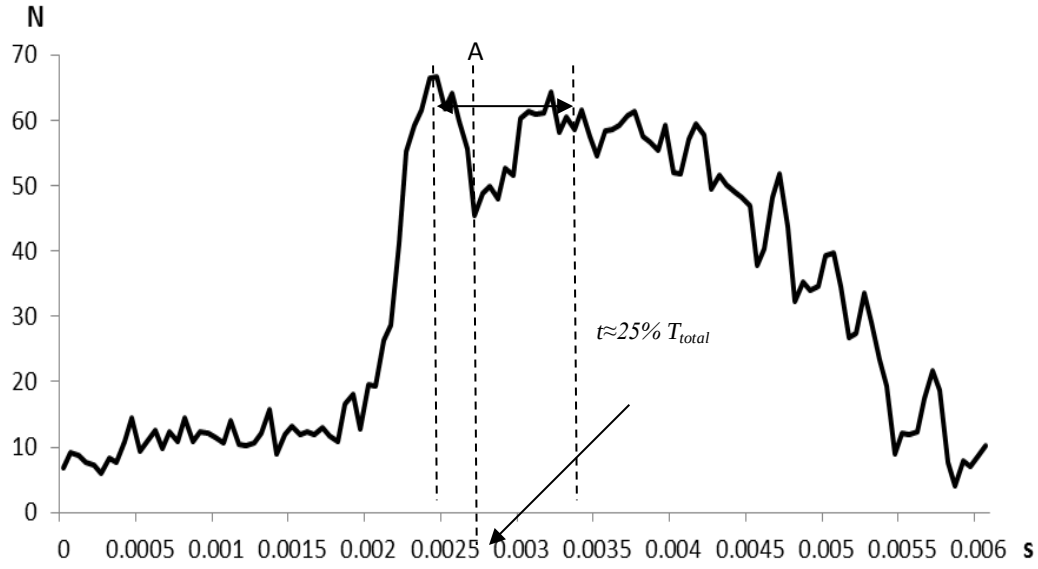

(b)

Figure 7.10 - Two sections of the different frequencies (a) sections with different frequencies of Sample 2 (b) instantaneous cutting force curve of Sample 2.

According to Equation (7-5), the frequency of chip serration has a linear relationship with the tool-chip contact length when the cutting speed is kept constant. Therefore, in this experiment, it is clear that the tool-chip contact length also changed in one milling cycle.

7.5 Summary

In the analysis of surface roughness it was observed that the feed of 0.035mm/tooth yielded the best surface finish in terms of Ra value. Even though the R_a value for lower feeds was less in some regions, it had zones where there were signs of vibrational waviness on the surface. On the other hand higher feed created some high grooves in the surfaces.

Various chip serration frequencies were observed on individual chips. The maximum difference between two sections was 5 times of the frequency. The dramatically changing frequency was the result of heat accumulation and the change of chip thickness. Frequency changes were found to take place at the position of 25% of the total length.

8 Conclusion

The innovation and main contributions made in this research are summarized in this chapter. The limitations of the methods developed in this research are addressed and suggestions for future research work are recommended.

8.1 Contributions

PCD tools are widely used in aerospace industry for machining composite material and Titanium alloys. Owing to the super-high hardness of diamond, traditional grinding processes cannot economically be applied to PCD tool production. The complicated geometric shapes of PCD inserts are machined either by EDG or Laser machining processes. However, the low conductivity of PCD, caused by its unique physical structure, makes it difficult to machine with conventional EDG parameters; special power generators are required in the machining process. Based on experimental studies, the relationship between gap voltages, peak current and electrical resistance of various PCD materials were investigated, the influence of peak current on the discharge waveforms was analyzed. It was found that discharge waveform in machining PCD was similar to that of machining ordinary materials such as Tungsten carbide. The maintaining voltage in machining PCD was higher than that of conventional EDM machining of conventional materials. The difference in the maintaining voltage was significant with the variation of PCD materials. The maintaining voltage increased linearly with the increase in current. Short-circuit arcing might not exist in the machining of PCD materials. However, it is difficult to predict if the non-short-circuit would occur when the electrode contacts the workpiece surface.

Experimental analysis shows that the three controllable machining parameters (feed, cutting depth and cutting speed) have a significant influence on the instantaneous cutting force. The feed affects the cutting force in two ways: the change in instantaneous undeformed chip thickness, and the change in cutting force coefficient. According to the experimental results, an increase of feed will lead to the increase in

cutting force. Cutting force also increases exponentially with the cutting speed and axial cutting depth. However, these two parameters affect the cutting force indirectly through the change in cutting force coefficients. Based on these analyses, a new cutting force model was developed and validated for the prediction of cutting forces in end milling Ti6Al4V with PCD tools. To predict the instantaneous cutting force more accurately, a time-dependent cutting force model has also been developed. Validation was conducted through cutting tests with a customized single flute PCD end mill. The maximum predictive error of the peaks of cutting forces was found to be less than 7 *N*.

The low thermal conductivity and high chemical affinity of Ti6Al4V make it extremely difficult to machine. Cutting temperature is an important factor that affects cutting forces. To investigate the thermal characteristics in end milling Ti6Al4V with PCD tools, an innovative cutting temperature predictive model was developed and validated through cutting experiments. The model described mathematical relationship between average cutting temperature and machining parameters. Experimental results show that the temperature increase with v_c, f_t and a_p. Results from the model match the data measured in the cutting experiments.

To analyze tool wear and cutting temperatures, residual chemical components on the PCD cutting tool were examined with X-ray diffraction method, while surface integrity of cutting tools was inspected based on the images taken by the scanning electrical microscope. Experiment results show that no massive chemical reaction had happened in the milling process with the selected cutting parameters, and the cutting temperature was below 500 ^{o}C. However, evidences of material diffusion and chemical reaction on PCD tools also showed that some region of the cutter suffered from higher than detected temperature.

Finite element analysis models were developed to simulate the initiation of cracks under different loading cycles. Through cutting experiments, it was found that brittle chipping and fatigue were the two major modes of failure, and feed was the dominant

factor that causes large cutting forces. The causes of the failures are shearing effect on the boundary of tool-chip interface, stress concentration at notch locations on the cutting edge and the uneven distribution of cutting stress on the area of contact between tool and chip. Directional damages by the shearing and friction were found in the experiments. The cleavage-like fractograph was mainly caused by the rubbing effect in the process and it appeared rarely in the experiment. The inhomogeneous material structure of PCD was the major factor which caused the delamination.

Based on SEM images of serrated chips, serration frequency was investigated. Results illustrated that serration frequency changed on each single chip. Two different serration frequencies could be found on a single chip. The boundary between the two regions with different serration frequencies was found to be at a position of 25 % of the chip length.

8.2 Future work

This research focused on the application of PCD tools in end milling of Titanium ally Ti6Al4V. Although two new models have been developed for the prediction of cutting force and cutting temperature, there is still much work to be done in this research. Some of these are theoretical while other issues are related to practical questions of implementation.

The cutting method applied in the experiments belongs to the category of conventional machining in terms of cutting speed and cooling method. Although the cutting speed for Aluminium alloys can be as high as 2,500 m/min, currently it is not uncommon to mill Titanium alloys (Ti6Al4V) at a speed less than 90 m/min. Therefore, to improve machining efficiency, future work can be done by integrating higher cutting speed in the predictive models based on what were achieved in this research.

Also, the two new methods for predicting instantaneous cutting force and average

cutting temperature are mainly based on the influence of machining parameters such as cutting speed, feed and axial cutting depth. The effects of cooling method and tool wear have not been considered. Therefore, to increase the accuracy and further minimize the predicting error, these two factors should be reflected in the model.

References

1. Rosemar B. da Silva, álisson R. Machado, Emmanuel O. Ezugwu, John Bonney and Wisley F. Sales (2013) “Tool life and wear mechanisms in high speed machining of Ti6Al4V alloy with PCD tools under various coolant pressures.” Journal of Materials Processing Technology 213:1459- 1464.

2. Mohd Hadzley AB, Izamshah R, Sarah AS, Nurul Fatin M (2013) “Finite Element Model of Machining with High Pressure Coolant for Ti6Al4V alloy.” Procedia Engineering 53: 624 - 631.

3. Lin S, Peng FY, Wen J, Liu YZ, Yan R (2013) “An investigation of workpiece temperature variation in end milling considering flank rubbing effect.” International Journal of Machine Tools & Manufacture 73: 71-86.

4. Koenig, W., Neises, N. (1993) “Turning TiAl6V4 with PCD.” Industrial Diamond Review 53(555): 85 - 88.

5. Nurul Amin, AKM, Ahmad FI, Nor Khairusshim MK (2007) “Effectiveness of uncoated WC-Co and PCD inserts in end milling of titanium alloy—Ti6Al4V.” Journal of Materials Processing Technology 192-193: 147-158.

6. Manouchehr V, Fredrik S, Mathias A, Jan-Eric S (2013) “A method for identification of geometrical tool changes during machining of titanium alloy Ti6Al4V.” International Journal of Advanced Manufacturing Technology 67: 339-348.

7. J. Sun, Y.B. Guo (2009) “A comprehensive experimental study on surface integrity by end milling Ti6Al4V.” Journal of Material Processing Technology 209: 4036-4042.

8. S. K. Bhaumik, C. Divakar and A. K. Singh (1995) “Machining Ti6Al4V alloy with

a wBN-cBN composite tool." Materials & Design 16: 4.

9. E.O. Ezugwu, R.B. Da Silva, J. Bonney, A ´.R. Machado. (2005) "Evaluation of the performance of CBN tools when turning Ti6Al4V alloy with high pressure coolant supplies." International Journal of Machine Tools & Manufacture 45, 1009-1014.

10. Z.G. Wang, Y.S. Wong, M. Rahman. (2005) "High-speed milling of titanium alloys using binderless CBN tools." International Journal of Machine Tools & Manufacture 45, 105-114.

11. Songlin Ding, R. Izamshah R.A, John Mo, and Yongwei Zhu. (2011) "The Development of an Economic Model for the Milling of Titanium Alloys." Key Eng Mater 458: 362-367.

12. Gert Adriaan Oosthuizen, Guven Akdogan, Nico Treurnicht (2011) "The performance of PCD tools in high-speed milling of Ti6Al4V." International Journal of Advanced Manufacturing Technology 52:929-935.

13. Emmanuel O. Ezugwu, John Bonney, Rosemar B. Da Silva, O. C- akir (2007) "Surface quality of finished turned Ti6Al4V alloy with PCD tools using conventional and high pressure coolant supplies." International Journal of Machine Tools & Manufacture 47, 884-891.

14. Schrock, D.J., Kwon, P. (2012) "Evidence of phase dependent tool wear in Ti6Al4V turning experiments using PCD and carbide inserts." Manufacturing Science and Engineering Conference 371 - 376.

15. E. Kuljanic, M. Fioretti, L. Beltrame, Pietro Rosa and F. Miani (1998) "Milling Titanium Compressor Blades with PCD Cutter." Annals of the ClRP 47/1.

16. Li. A., Zhao. J., Wang. D., Zhao. J., Dong. Y. (2012) "Failure mechanism of a PCD tool in high-speed face milling of Ti6Al4V alloy." International Journal of

Advanced Manufacturing Technology 1 - 8.

17. Ota. M., Okjda. J., Harada. T., Toda. N., Sumiya. H. (2009) “High speed cutting of titanium alloy with PCD tools.” Key Engineering Materials. 389 - 390: 157 - 162.

18. Anhai L, Jun Z, Dong W, Jiabang Z, Youngwang D (2013) “Failure mechanisms of a PCD tool in high-speed face milling of Ti6Al4V alloy.” International Journal of Advanced Manufacturing Technology 67: 1959-1966.

19. Yan-Cherng Lin, Yuan-Feng Chen, Der-An Wang, Ho-Shiun Lee (2009) “Optimization of machining parameters in magnetic force assisted EDM based on Taguchi method.” Journal of materials processing technology 209:3374-3383.

20. Mu-Tian Yan, Hsing-Tsung Chien (2007) “Monitoring and control of the micro wire-EDM process.” International Journal of Machine Tools & Manufacture 47:148-157.

21. S H Yeo, W Kurnia, P C Tan (2007) “Electro-thermal modelling of anode and cathode in micro-EDM.” Journal of Physics D: Applied Physics 40:3513.

22. R. Garn, A. Schubert, H.Zeidler (2011) “Analysis of the effect of vibrations on the micro-EDM process at the workpiece surface.” Precision Engineering 35: 364-368.

23. D. Gurgu ¡ E. V ázqueza, I. Ferrer (2013) “Influence of the Process Parameters to Manufacture Micro-cavities by Electro Discharge Machining (EDM).” Procedia Engineering 63: 499-505.

24. F. C. Hsu, T. Y. Tai, V. N. Vo, S. Y. Chen, Y. H. Chen (2013) “The machining characteristics of polycrystalline diamond (PCD) by micro-WEDM.” Procedia CIRP 6:261-266.

25. Pei-Lum Tso, Yan-Gang Liu (2002) “Study on PCD machining.” International Journal of Machine Tools & Manufacture 42: 331-334.

26. M. Iwai, S. Ninomiya, K. Suzuki (2013) “EDM properties of newly developed PCD made up of electrically conductive diamond particles.” Procedia CIRP 6:140-145.

27. C. Gao, Z. Zhan, S. Wang, N. He, L. Li (2013) “Research on WEDM process optimization for PCD micro milling tool.” Procedia CIRP 6:209-214.

28. Balkrishna R, Chinmaya RD, Yung CS (2011) “An experimental and numerical study on the face milling of Ti6Al4V alloy: Tool performance and surface integrity.” Journal of Materials Processing Technology 211: 294-304.

29. Johnson, G.R.; Cook, W.H. (1983), “A constitutive model and data for metals subjected to large strains, high strain rates and high.” Proceedings of the 7th International Symposium on Ballistics: 541-547.

30. Yun W.S, Cho D.W (2000) “An Improved Method for the Determination of 3D Cutting Force Coefficients and Runout Parameters in End Milling.” International Journal of Advanced Manufacturing Technology 16:851-858.

31. Lee T.S, Lin Y.J (2000) “A 3D Predictive Cutting-Force Model for End Milling of Parts Having Sculptured Surfaces.” International Journal of Advanced Manufacturing Technology 16:773-783.

32. W. A. Kline, R.E. DeVor. (1983) “The effect of runout on cutting geometry and forces in end milling.” International Journal of Machine Tool Design Research 23: 123-140.

33. M. Wan, W.H. Zhang, G.H. Qin, G. Tan (2007) “Efficient calibration of instantaneous cutting force coefficients and runout parameters for general end mills.” International Journal of Machine Tools & Manufacture 47: 1767-1776.

34. B.H. Wu, X. Yan, M. Luo, G. Gao (2013) “Cutting force prediction for circular end

milling process." Chinese Journal of Aeronautics 26(4): 1057-1063.

35. J. Barry, G. Byrne, D. Lennon. (2001) "Observations on chip formation and acoustic emission in machining Ti6Al4V alloy." International Journal of Machine Tools & Manufacture 41: 1055-1070.

36. Ezugwu E，Wang Z M．(1997) "Titanium alloys and their machinability—a review." Journal of Materials Processing Technology 68: 263 - 274.

37. Moaz H. Ali, Basim A. Khidhir, M.N.M. Ansari, Bashir Mohamed (2013) "FEM to predict the effect of feed on surface roughness with cutting force during face milling of titanium alloy." Housing and Building National Research Center.

38. S. M. Wang, C. H. Chiou, Y. M. Cheng (2004) "An improved instantaneous cutting force model for end-milling process." Journal of Materials Processing Technology 148: 317-327.

39. Y. Yang, W. H. Zhang, M. Wan. (2011) "Effect of cutter runout on process geometry and forces in peripheral milling of curved surfaces with variable curvature." International Journal of Machine Tools & Manufacture 51: 420-427.

40. A. Lamikiz , L.N. Lopez de Lacalle, J.A. Sanchez, M.A. Salgado (2004) "Cutting force estimation in sculptured surface milling." International Journal of Machine Tools & Manufacture 44:1511-1526.

41. Le Coz G, Marinescu M, Devillez A, Dudzinski D, Velnom L (2012) "Measuring temperature of rotating cutting tools: Application to MQL drilling and dry milling of aerospace alloys." Applied Thermal Engineering 36:434-441.

42. Masahiko S, Takashi U, Hisataka T (2007) "An experimental technique for the measurement of temperature on CBN tool face in end milling." International Journal of Machine Tools & Manufacture 47: 2071-2076

43. Pittal à GM, Monno, M (2011) "A new approach to the prediction of temperature of the workpiece of face milling operations of Ti6Al4V." Applied Thermal Engineering 31:173-180.

44. G. List, G. Sutter, A. Bouthiche (2012) "Cutting temperature prediction in high speed machining by numerical modelling of chip formation and its dependence with crater wear." International Journal of Machine Tools & Manufacture 54-55: 1-9.

45. Chen Ming, Sun Fanghong, Wang Haili, Yuan Renwei, Qu Zhenghong, Zhang Shuqiao (2003) "Experiment research on the dynamic characteristics of the cutting temperature in the process of high-speed milling." Journal of Materials Processing Technology 138:468-471.

46. Cui XB, Zhao J, Pei ZQ (2012) "Analysis of transient average tool temperatures in face milling." International Communications in Heat and Mass Transfer 39: 786-791.

47. Ugarte A, M'Saoubi R, Garay A, Arrazola PJ (2012) "Machining behaviour of Ti6Al4V and Ti-5553 alloys in interrupted cutting with PVD coated cemented carbide." Procedia CIRP 1:202 - 207.

48. ABHANG LB, HAMEEDULLAH M (2010) "Chip-Tool Interface Temperature Prediction Model for Turning Process." International Journal of Engineering Science and Technology 2(4):382-393.

49. Xuance Z, Qingshun B, Kai Y, Zhi L (2010) "Relationship between Cutting Temperature and Cutting Parameters of Micro-milling." World Academy of Science, Engineering and Technology 46.

50. Machado AR, Wallbank J (1990) "Machining of titanium and its alloys - a review." Proceedings of the Institution of Mechanical Engineers, Part B: Journal of

Engineering Manufacture 53: 204.

51. Deng JX, Li YS, Song WL (2008) “Diffusion wear in dry cutting of Ti6Al4V withWC/Co carbide tools.” Wear 265:1776-1783.

52. A. Jawaid, S. Sharif, S. Koksal (2000) “Evaluation of wear mechanisms of coated carbide tools when face milling titanium alloy.” Journal of Materials Processing Technology 99: 266-274.

53. M.J. Bermingham, J.Kirsch, S.Sun, S.Palanisamy, M.S.Dargusch (2011) “New observations on tool life, cutting forces and chip morphology in cryogenic machining Ti6Al4V.” International Journal of Machine Tools & Manufacture 51: 500-511.

54. A.K.M.N. Amin, N.V.Talantov (1986) “Influence of the instability of chip formation and preheating of work on tool life in machining high temperature resistant steel and titanium alloys.” Mechanical Engineering Research Bull. 9: 52-62.

55. R. Komanduri (1981) “New observations on the mechanism of chip formation when machining titanium alloys.” Wear 69: 179-188.

56. Kirk DC, (1971) “Cutting aerospace materials (Nickel, cobalt and titanium based alloys)” Rolls Royce Ltd London.

57. Ezugwu EO, Bonney J, Yamane Y (2003) “An overview of the machinability of aeroengine alloys.” Journal of Materials Processing Technology 134:233-253

58. S.Zang, J.F.Li, J.Sun, F.Jiang (2010) “Tool wear and cutting forces variation in high speed endmilling Ti6Al4V Alloy.” International Journal of Advanced Manufacturing Technology 46:69-78.

59. Emmanuel O. Ezugwu, John Bonney, Rosemar B. Da Silva, O. C- akir (2007)

"Surface integrity of finished turned Ti6Al4V alloy with PCD tools using conventional and high pressure coolant supplies." International Journal of Machine Tool & Manufacture 47, 884-891.

60. ISO Standard 3685.

61. Xiao Jiang Cai, Zhi Qiang Liu, Ming Chen and Qing Long (2012) "An experimental investigation on effects of minimum quantity lubrication oil supply rate in high-speed end milling of Ti -6Al-4V." Proceedings of the Institution of Mechanical Engineers, Part B: Journal of Engineering Manufacture 226: 1784.

62. Q.A. Shenderova, D.W.Brenner, A.Omeltchenko, X.Su, Lin H.Yang and A.Nazarov (1999) "Properties of Polycristalline Diamond: multiscale Modelling approach." Molecular Simulation 24: 2000.

63. A. Li, J. Zhao, Y. Dong, D. Wang, X. Chen (2013) "Surface quality of high-speed face milled Ti6Al4V alloy with PCD tools." Machining Science and Technology 17: 464 - 482.

64. SU Honghua, LIU Peng, FU Yucan, XU Jiuhua (2012) "Tool Life and Surface Integrity in High-speed Milling of Titanium Alloy TA15 with PCD/PCBN Tools." Chinese Journal of Aeronautics 25: 784-790.

65. Puerta JD, Vel ́asquez Bolle B, Chevrier P, Geandier G, Tidu A (2007) "Metallurgical study on chips obtained by high speed machining of a Ti-6 wt.%Al-4 wt.%V alloy." Materials Science and Engineering A 452-453: 469-474.

66. Sima M, Ozel T (2010) "Modified material constitutive models for serrated chip formation simulations and experimental validation in machining of titanium alloy Ti6Al4V." International Journal of Machine Tools & Manufacture 50: 943-960.

67. A.L. Mantle, D.K. Aspinwall, (1998) "Tool life and workpiece surface roughness

when high speed machining a gamma titanium aluminide, progress of cutting and grinding." in: Proceedings of the Fourth International Conference on Progress of Cutting and Grinding, International Academic Publishers, Urumqi and Turpan, China, pp. 89-94.

68. Molinari A, Soldani X, Migu´ez MH (2013) "Adiabatic shear banding and scaling laws in chip formation with application to cutting of Ti6Al4V." Journal of the Mechanics and Physics of Solids 61: 2331-2359.

69. Migu´ez MH, Soldani X, Molinari A (2013) "Analysis of adiabatic shear banding in orthogonal cutting of Ti alloy." International Journal of Mechanical Sciences 75: 212-222.

70. Baker M (2003) "The influence of plastic properties on chip formation." Computational Materials Science 28: 556-562.

71. K.H.Ho, S.T. Newman (2003) "State of the art electrical discharge machining (EDM)", International Journal of Machine Tools & Manufacture 23:1287-1300.

72. N.M. Abas, D.G. Solomon, M.F.Bahari (2007) "A review on current research tgrends in electrical discharge machining (EDM)." International Journal of Machine Tools & Manufacture 47:1214-1228.

73. M.P. Jahan, Y.S. Wong, M. Rahman (2009) "A study on the fine-finish die-sinking micro-EDM of tungsten carbide using different electrode materials", Journal of materials processing technology 209: 3956-3967.

74. Hassan EI-Hofy (2005) "Advanced Machining Processes." McGraw-Hill.

75. Altpeter, F., Perez, R. (2004) "Relevant Topics in Wire Electrical Discharge Machining Control." Journal of Materials Processing Technology 149 /1-3: 147-151.

76. Chingyei Chung, Shou-Yen Chao, M. F. Lu (2009) “Modeling and Control of Die-sinking EDM.” WSEAS TRANSACTIONS on SYSTEMS 8: 1109-2777.

77. Elman C. Jameson (2001) “Electrical Discharge Machining.” The society of manufacturing engineers.

78. Peter J. Heath (2001) “Development in application of PCD tooling.” Journal of Materials Processing Technology 116: 31-38.

79. E.O. Ezugwu (2005) “Key improvements in the machining of difficult-to-cut aerospace superalloys.” International Journal of Machine Tools & Manufacture 45: 1353-1367.

80. Shane A. Catledge, Yogesh K. Vohra, Ram Ladi, Ghanshyam Rai (1996) “Micro-Raman stress investigations and X-ray diffraction analysis of polycrystalline diamond (PCD) tools.” Diamond and Related Materials 5: 1159-1165.

81. B. Lauwers, J.P. Kruth, W. Liu, W. Eeraerts, B. Schacht, P. Bleys (2004) “Investigation of material removal mechanisms in EDM of composite ceramic materials.” Journal of Materials Processing Technology 149: 347-352.

82. C.J. Luis, I. Puertas, G. Villa (2005) “Material removal rate and electrode wear study on the EDM of silicon carbide.” Journal of Materials Processing Technology 164-165: 889-896.

83. T. Masaki, T.Kuriyagawa , J. Yan, N. Yoshihara (2007) “Study on shaping spherical Poly Crystalline Diamond tool by Micro-electro-Discharge Machining and micro-grinding with the tool.” International Journal of Surface Science and Engineering 1(4): 344-359.

84. T.B. Thoe, D. K. Aspinwall, M.L.H. Wise and I.A.Oxley (1996) “Polycrystalline

Diamond Edge Quality and Surface Integrity Following Electrical Discharge Grinding." Journal of Materials Processing Technology 56: 773-785.

85. R.H.Olsen, D.K.Aspinwall, R.C.Dewes (2004) "Electrical Discharge Machining of Conductive CVD Diamond Tool Blanks." Journal of Materials Processing Technology 155-156: 1227-1234.

86. D.T. Pham, S.S. Dimov, S. Bigot, A. Ivanov, K. Popov (2004) "Micro-EDM — recent developments and research issues." Journal of Materials Processing Technology149 (1-3): 50 - 57.

87. Mikell P.Groover (2007) "FUNDAMENTALS OF MODERN MANUFACTURING. (Third Edition)" John Wiley & Sons.

88. P.-J. Arrazola, A. Garay, L.-M. Iriarte, M. Armendia, S. Marya, F. Le Maitre (2009) "Machinability of titanium alloys (Ti6Al4V and Ti555.3)." Journal of Materials Processing Technology 209: 2223-2230.

89. Woei-Shyan Lee, Tao-Hsing Chen, His-Hwa Hwang (2008) "Impact Response and Microstructural Evolution of Biomedical Titanium Alloy under Various Temperatures." Metallurgical and Materials Transactions A 39:1435-1448.

90. P.L.B. Oxley (1989) "Mechanics of Machining: An Analytical Approach to Assessing Machinability." Ellis Horwood, Chichester.

91. P. Lee, Y. Altintas (1996) "Prediction of ball-end milling forces from orthogonal cutting data." International Journal of Machine Tool Manufacture 36 (9): 1059-1072.

92. K. Levenberg (1944) "A method for the solution of certain problems in least squares, Quart." Appl. Math 2: 164–168.

93. D. Marquardt (1963) "An algorithm for least-squares estimation of nonlinear

parameters" SIAM J. Appl. Math (11) 431–441.

94. Sadao Sano, Kiyoshi Suzuki, W. L. Pan, M. Iwai, Y. Murakami, T. Uematsu (2007) "Forming Fine V-Grooves on a Tungsten Carbide Workpiece with a PCD electrode by EDM." Key Engineering Materials 329: 631-636.

95. Moussaoui K, Mousseigne M, Senatore J, Chieragatti R, Monies F (2013) "Influence of milling on surface integrity of Ti6Al4V—study of the metallurgical characteristics: microstructure and microhardness." International Journal of Advanced Manufacturing Technology 67:1477-1489.

96. Li A, Zhao J, Wang D, Zhao J.B, Dong Y.W (2013) "Failure mechanisms of a PCD tool in high-speed face milling of Ti6Al4V alloy." International Journal of Advanced Manufacturing Technology 67:1959-1966.

97. Wang JJ, Zheng CM (2002) "An analytical force model with shearing and ploughing mechanisms for end milling." International Journal of Machine Tool & Manufacture 42: 761-771.

98. Wan M, Zhang WH, Dang JW, Yang Y (2010) "A novel cutting force modelling method for cylindrical end mill." Applied Mathematical Modelling 34: 823-836.

99. N. H. COOK (1973) "Tool Wear and Tool Life." Journal of Engineering for Industry. 931-938.

100. Loewen, E.G., Shaw, M.C. (1954) "On the Analysis of Cutting Tool Temperatures." Transactions of the ASME, 76:217-231.

101. Abukhshim NA, Mativenga PT, Sheikh MA (2006) "Heat generation and temperature prediction in metal cutting: A review and implications for high speed machining." International Journal of Machine Tools & Manufacture 46: 782-800.

102. Anayet UPMd, Nurul Amin AKM, Faris WF (2009) "PREDICTION OF

TANGENTIAL CUTTING FORCE IN END MILLING OF MEDIUM CARBON STEEL BY COUPLING DESIGN OF EXPERIMENT AND RESPONSE SURFACE METHODOLOGY." Journal of Mechanical Engineering 40:2.

103. Umbrello D (2008) "Finite element simulation of conventional and high speed machining of Ti6Al4V alloy." Journal of materials processing technology 196: 79-87

104. ISO Standard 8688 -1 and ISO Standard 8688 -2.

105. Polycrystalline diamond composites US 3913280 A.

106. ASM Metals HandBook Volume 19 FATIGUE AND FRACTURE.

107. D. Iliescu, D. Gehin, M. E. Gutierrez, F. Girot (2010) "Modeling and tool wear in drilling of CFRP." International Journal of Machine Tools & Manufacture 50: 204-213.

108. Z. P. Hao, D. Gao, Y. H. Fan, R. D. Han (2011) "New observations on tool wear mechanism in dry machining Inconel718." International Journal of Machine Tools & Manufacture 51: 973-979.

109. Tze-Pin Lin and George A. Cooper. Michael Hood (1993) "Fatigue test on polycrystalline diamond compacts." Material Science and Engineering A163: 23-31.

110. Feng CHEN, XU Gen, XU Guo-ping, MA Chun-de (2010) "Influences of shock damage on edgewise compressive strength of PDC." Journal of Central South University (Science and Technology). In Chinese 41: 5.

111. S.G. Moseley, K.-P. Bohn, M. Goedickemeier (2009) "Core drilling in reinforced concrete using polycrystalline diamond (PCD) cutters: Wear and fracture mechanisms." International Journal of Refractory Metals & Hard Materials 27:

394-402.

112. M. Werner, S. Klose, F. Sztics, Ch. Moelle, H.J. Fecht, C. Johnston, P.R. Chalker, I.M. Buckley-Golder (1997) High temperature Young's modulus of polycrystalline diamond.” Diamond and Related Material 6: 344- 347.

113. ASM Handbook committee, ASM Hand book volume 12, 1987.

114. Martellotti, M. E. (1941) “An Analysis of the Milling Process.” ASME Transactions 63: 677-700.

115. Thomas W. Wright (2012) “Adiabatic Shear Localization (Second Edition).” Elsevier. ISBN: 978-0-08-097781-2. 215-246.